Optomechanical Integrated Circuits for Efficient Microwave-to-Optical Transduction

I-Tung Chen

A dissertation

submitted in partial fulfillment of the

requirements for the degree of

Doctor of Philosophy

University of Washington
2025

Reading Committee:

Mo Li, Chair

Kai-Mei Fu

Arthur Barnard

Program Authorized to Offer Degree:

Electrical and Computer Engineering

© Copyright 2025

I-Tung Chen

University of Washington

Abstract

Optomechanical Integrated Circuits for Efficient Microwave-to-Optical Transduction

I-Tung Chen

Chair of the Supervisory Committee:
Mo Li
Department of Electrical & Computer Engineering, Department of Physics

Microwave-to-optical transduction is crucial for long-distance data transmission in both classical and quantum networks. In classical applications, microwave-to-optical transduction can be achieved through electro-optics effect. In quantum applications, cavity-optomechanical systems with microwave phononic mode are uniquely suitable for this task. However, a scalable platform to achieve efficient microwave-to-optical transduction is still elusive. This work presents three novel approaches to address these limitations.

First, a wafer-scale boron-doped gallium phosphide (BGaP) material platform is utilized to demonstrate scalable optomechanical devices. The BGaP optical resonators exhibit intrinsic quality factors exceeding 25,000 at visible and 200,000 at telecom wavelengths. It further demonstrates a low acoustic propagation loss and an integrated acousto-optic frequency shifter (AOFS) using a zinc oxide (ZnO) hybrid integration. These results show BGaP material as a promising platform for scalable optomechanical technologies.

Second, we develop a BGaP-based optomechanical integrated circuit (OMIC) featuring the first ring-type optomechanical cavity—an optomechanical ring resonator (OMR)—in which phononic and photonic modes co-circulate and interact. The hybrid platform, which combines suspended BGaP for waveguiding and ZnO for phonon generation, achieved an intermodal conversion efficiency of $\eta_i = 2.1\%$ at a low acoustic pump power of 1.6 mW. This enables an efficient microwave-to-optical transduction for quantum information and microwave photonics applications.

Finally, we introduce a non-suspended OMIC using silicon-on-sapphire (SOS), compatible with state-of-the-art superconducting qubits. By leveraging the triple co-resonance modes, we report a phonon pump-enhanced coupling rate $G_b = 3.6$ GHz/mW$^{-1/2}$ at a low microwave drive power $P_{\text{MW}} = 3.6$ mW. This is the first OMIC demonstration on a non-suspended material platform with a GHz pump-enhanced coupling rate, and we project a two-order magnitude improvement of coupling rate by optimizing the design, which paves the way for an ultra-efficient microwave-to-optical conversion for quantum interconnect. We conclude by discussing the outlooks and the challenges of OMIC and propose possible ways to improve the OMIC performance for quantum transduction.

Contents

List of Figures

List of Tables

ACKNOWLEDGEMENTS

My PhD journey started at an *interesting* time during March 2020. Since then, this journey has been brining me incredible experiences and helping me grow personally and professionally. I am truly grateful for the support from people around me, so, I would like to acknowledge them here.

First off, I would like to thank my advisor, **Prof. Mo Li**, whose guidance has been crucial throughout my PhD journey. I am always amazed by your ability to distill complex concepts into clear, accessible explanations. It not only helped me understand the knowledge but also taught me the importance of effective communication. Your innovative approach to tackle research challenges consistently offers perspectives I would never have considered on my own. I am also grateful for the intellectual freedom that you granted me during my study, which has been instrumental in my development as an independent researcher. The last few years have been truly exceptional, and I have thoroughly enjoyed the time working with you. I hope that after I finish my PhD study, we would still maintain connection, and run into each other from time to time.

Prof. Kai-Mei Fu, thank you for being a member of my committee and providing valuable feedbacks and ideas. I also want to thank you for fostering the quantum community here at UW, especially for AQET. Being a student leader of AQET is a truly unbelievable experience. The rare opportunity of hosting Dr. Darío Gil and Prof. Peter Shor would not have happened without your support. I hope the great tradition of providing quantum public lectures at UW would continue for many years.

Prof. Arthur Barnard and **Prof. Dan Fu**, thank you for being on the committee. Your feedbacks and ideas are really appreciated. Arthur, I think the first time I formally learn about optomechanics, it was from your lecture. I really enjoyed it, and it built a solid foundation for my research, so, thank you for offering the class. Also, thank you for spending time discussing research collaborations and letting me play with your dilfridge. Dan, although we didn't have much overlap in research or in class, thank you for being on my committee for both my general exam and dissertation defense.

Nick, it is really fun collaborating with you. You helped me so much on the OMR project, and I'm really grateful for your insight and analysis on it. I truly admire your analysis skills and the OMR project could not have succeeded without your contributions, thank you! Not only that, I have also learned so much from you as a researcher and a classmate. I wish the best for your career, and I hope we have opportunities to collaborate in the future, too.

Adina, my bestie in Mo's group! We joined the group in the same year, trained in WNF together, and even live together in the same house. When the PhD life gets challenging, we could always brainstorm ideas for each other, for which I am really grateful. I cherish our time hanging out at the bar, bouldering at SBP, top-roping at stone garden, hiking mountains, attending Vancouver quantum workshop, going to CLEO, and many more things we did together. Good luck with finishing your thesis, because you're next!

Seokhyeong, my senpai in Mo's group, we have many good conversations not only about life but also about random interesting things. You kept me sane during the chaotic schedule of fabricating and measuring devices. You also taught me how to play tennis. I am glad that I have you as a senpai. Thank you!

Hannah, Sanskriti, Rithi, and Chaman. My fellow AQET student leaders! Without your helps and supports, we could never host so many unforgettable events. Thank you guys so much, I will remember the fun we had working together.

Former and current students in Mo's group whom I worked with: **Bingzhao, Qixuan, Haoqin, Shucheng, Yue, Ameya, and Mark**, thank you all for helping me out, giving advises, and most of all, supporting each other in the group.

Finally, I'd like to thank my parents and my loving husband, **Wei-Ting**. Your unwavering support and tender care carried me through what has been one of the most demanding and challenging years of my life. Your presence and understanding made this journey possible.

March, 12, 2025, Seattle

DEDICATION

To my parents, who gave me the gift of dreams and the ability to realize them.

To my husband, my best friend, my greatest supporter.

Chapter 1

Introduction

Quantum computing requires millions of physical qubits to implement a fault-tolerant error corrected algorithm for practical application [8]. Current superconducting-based systems fall short of this goal, primarily due to limitations in cryogenic cooling capacity and the space required for microwave cables. While researchers have shown inter-dilution refrigerator connection via cables [9] and/or optical fibers [10], the challenge remains. Nevertheless, recent work has demonstrated promising applications even on today's noisy, pre-fault-tolerant processors [11].

A quantum transducer, in which quantum states can be converted efficiently between different physical systems, is a promising technology for interconnecting multiple quantum processors to form a large-scale quantum network. However, the realization of such a device is challenging because of the 10^5 times difference in frequency between a microwave photon, which most of the physical qubit systems are based on, and an optical photon, where long range optical fiber communication is available. To address this frequency disparity, several approaches such as electro-optics [12], piezo-optomechanics [13], Rydberg-atom assisted [14], and magnon-mediated [15] microwave-to-optical (M2O) conversion have been proposed and demonstrated. Among them all, electro-optical and optomechanical M2O transduction have been the most compact and integrable on-chip solutions. In the scope of this work, optomechanical approaches leverage the fundamental interaction between light and mechanical waves in solids, a phenomenon that has been studied for over a century. This year, 2025, marks the 103rd anniversary after Leon Brillouin first investigated the interaction between light and thermally excited sound waves in solids [16]. The effect of *Brillouin scattering*, which is named after Leon Brillouin, describes the optical wave being modulated when passing through a medium (either resulting in a change of light propagating direction, and/or in a change of the wavelength of the light wave). This effect lies at the heart of this dissertation.

There are two main types of Brillouin scattering: spontaneous Brillouin scattering [17] and stimulated Brillouin scattering [18]. Spontaneous Brillouin scattering occurs when the interaction between optical and acoustic waves happens naturally. This type of scattering is typically weak at low laser power and requires sensitive detection methods to observe. At high laser power, the stimulated Brillouin scattering (SBS) [19] occurs when an external seed laser is used to amplify the interaction between acoustic waves and the scattered light. The simplest mathematical description of Brillouin scattering is the momentum and energy conservation of optical and acoustic wave inelastic scattering. Consider an incoming light wave with angular frequency ω and momentum β, which is scattered by an acoustic wave with angular frequency Ω and momentum q. The scattered light wave will have an angular frequency ω' and momentum β'. The conservation of energy and momentum can be written as:

$$\omega' = \omega \pm \Omega, \tag{1.1a}$$

$$\beta' = \beta \pm q. \tag{1.1b}$$

Here, the plus sign corresponds to anti-Stokes scattering (phonon absorption), and the minus sign corresponds to Stokes scattering (phonon emission). These equations describe the energy and momentum transfer between the optical and acoustic waves, this is also known as the phase-matching condition (PMC).

While Brillouin scattering applies on free-propagating acoustic and optical waves, cavity optomechanics describes the mechanical motion and optical force interplay in a cavity. In other words, the radiation pressure from light in the cavity causes the material to deform, which shifts the cavity's resonant frequency. This can be written as

$$\omega_{\mathrm{cav}}(x) \approx \omega_{\mathrm{cav}} + x\frac{\partial \omega_{\mathrm{cav}}}{\partial x} \tag{1.2}$$

where the optical resonant frequency $\omega_{\mathrm{cav}}(x)$ is shifted by the material deformation x of the optomechanical cavity. The cavity optomechanical description is our bridge to understanding the quantum dynamics of our system, and we will discuss this in depth in the following chapters.

In this work, we harness both Brillouin scattering and the cavity optomechanical interaction in nanostructured devices that enable enhanced microwave-to-optical conversion. The wavelength-scale optical waveguides and cavities, can be engineered to have specific properties that enhance the Brillouin scattering process, leading to an efficient modulation of light. One of the key advantages of using integrated devices is the ability to confine both optical and acoustic waves to very small volumes. This confinement increases the interaction strength between the waves, allowing for an efficient energy transfer.

This dissertation is structured as follows: Chapter 2 provides an introduction to the fundamental theoretical backgrounds and a brief review of the current state of microwave-to-optical transducers. We build on the knowledge of the previous works and apply this to the optomechanical integrated circuit (OMIC) design for efficient microwave-to-optical transduction. Chapter 3 starts by investigating a novel boron-doped gallium phosphide (BGaP) platform for integrated acousto-optics devices. Chapter 4 demonstrates an OMIC with an optomechanical ring resonator (OMR) using BGaP to achieve efficient microwave-to-optical frequency conversion. In Chapter 5, we re-design the OMIC on a silicon-on-sapphire (SOS) platform that is compatible with superconducting qubits and demonstrate an efficient microwave-to-optical transduction. Finally, in Chapter 6, we discuss the challenges of OMIC and propose future directions to improve the efficiency of OMR and propose a way to integrated OMIC with superconducting qubits in a dilfridge.

Chapter 2

Theory and backgrounds of piezo-optomechanics

In this chapter, we first introduce the effect of piezoelectricity, which can be used to convert microwave signals to mechanical waves in materials. Then, we detail the acousto-optic effect and the Brillouin scattering by investigating the phase-matching condition between mechanical and optical waves in materials. Following that, we discuss the theoretical foundation of cavity-optomechanics to perform microwave-to-optical conversions.

2.1 Electromechanical transducers and piezoelectric materials

When mechanical strain (material deformation) generates electric fields in a non-centrosymmetric crystal, this is often described as the direct piezoelectric effect, and the vice versa is usually referred as the converse piezoelectric effect. In this chapter, for simplicity, we will refer the converse piezoelectric effect as piezoelectric effect. This is because we generally apply electric fields to the materials to generate mechanical waves. We can describe the piezoelectric effect as

$$T = c_E \cdot S - e^T \cdot E, \tag{2.1}$$

where T is stress, S is strain and E is the external electric field. c_E and e^T are the elasticity matrix(6x6 matrix) and the transposed piezoelectric coupling matrix(3x6 matrix) respectively. In Voigt notation, the elasticity matrix c_E and the piezoelectric coupling matrix e^T of a zinc-blend crystal structure takes the form of

$$c_E = \begin{bmatrix} c_{11} & c_{12} & c_{12} & 0 & 0 & 0 \\ c_{12} & c_{11} & c_{12} & 0 & 0 & 0 \\ c_{12} & c_{12} & c_{11} & 0 & 0 & 0 \\ 0 & 0 & 0 & c_{44} & 0 & 0 \\ 0 & 0 & 0 & 0 & c_{44} & 0 \\ 0 & 0 & 0 & 0 & 0 & c_{44} \end{bmatrix}, e^T = \begin{bmatrix} 0 & 0 & 0 & e_{14} & 0 & 0 \\ 0 & 0 & 0 & 0 & e_{14} & 0 \\ 0 & 0 & 0 & 0 & 0 & e_{14} \end{bmatrix}. \tag{2.2}$$

A table of c_E and e^T from selective piezoelectric materials is shown in Table 2.1. Zinc oxide (ZnO) is of particular interest since it can be easily sputtered on various substrates while retaining a high piezoelectricity. We also include gallium phosphide (GaP) because the recent demonstration of a high quality GaP photonic ring and microwave-to-optical transducer [20]. However, the piezoelectric coupling coefficient is relatively low for GaP. This indicates that it would be difficult to generate acoustic waves across GaP thin films via piezoelectric coupling on its own, so a hybrid integration is needed to launch the acoustic waves that can propagate through or into GaP.

Crystals	c_E [GaP]	e^T [C/m^2]
GaP	c_{11}=141.2, c_{12}=62.53, c_{44}=70.47	e_{14}=-0.1
ZnO	c_{11}=209.7, c_{12}=121.1, c_{44}=42.3	e_{33}=1.32
$LiNbO_3$	c_{33}=242(highest)	e_{15}=3.38

Table 2.1: Elasticity and piezoelectricity coefficient for common materials

The second component of generating acoustic waves in material is the interdigital transducer (IDT). IDTs are metal electrodes deposited on material that create alternative electric fields to excite the piezoelectric materials [21]. IDTs on piezoelectric materials have been widely used in radio-frequency (RF) filtering in wireless communication. IDT transduces incoming RF signal into oscillating mechanical vibrations via piezoelectric effect, and the period (Λ)—the distance between two electrodes of the same polarity— determines the wavelength of the generated acoustic waves,

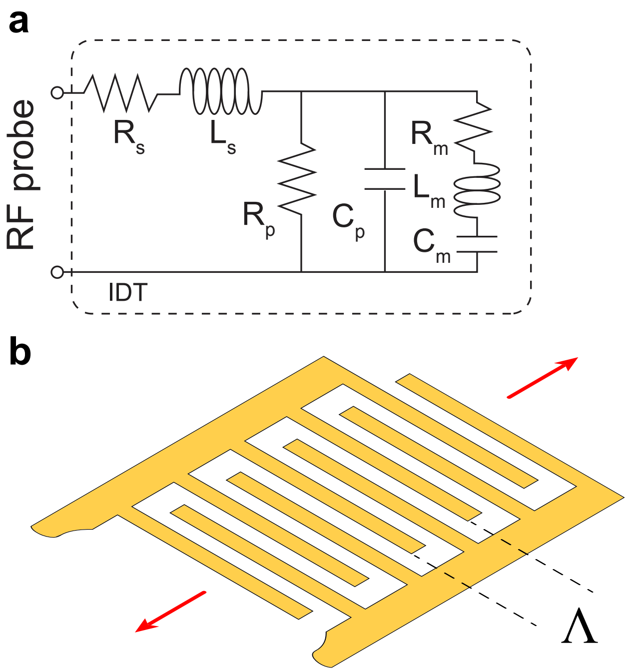

Figure 2.1: Lumped-element model and an illustration of IDT (a) A lumped-element model for the IDT (b) An illustration of the IDT

as shown in Fig. 2.1b. The characteristics of the IDT with the piezoelectric material is often modeled by the modified Butterworth Van-Dyke (mBVD) circuit (Appendix II for full derivation) to analyze the system, as shown in the inset of Fig. 2.1a. The total load impedance of the IDT can be expressed as the following

$$\begin{aligned} Z_{\text{total}} &= Z_s + Z_{\text{load}}, \\ Z_s &= R_s + j\omega L_s, \\ Z_{\text{load}} &= \left(\frac{1}{Z_p} + \sum_N Y_m^{(N)}(\omega)\right)^{-1}, \\ Z_p &= \frac{1}{j\omega C_p + 1/R_p} \end{aligned}$$

and

$$Y_m(\omega) = \frac{1}{Z_m} = \frac{1}{R_m + j\omega L_m + 1/j\omega C_m}. \tag{2.3}$$

The total load impedance Z_{total} of a fabricated device can be calculated from the measured S_{11} using the following expression

$$Z_{\text{total}} = R_{char} \times \frac{1 + \mathbb{C}(S11(\omega))}{1 - \mathbb{C}(S11(\omega))}, R_{char} = 50\Omega.$$

Note that S_{11} is a complex number. The IDT electromechanical (electric-to-mechanical) conversion efficiency is defined as the power ratio of the power on mechanical lumped elements P_m and the input power P_{in}. The input power that is transferred to Y_m can be expressed as

$$P_m = Re[V_{Y_m}^2 \cdot Y_m]$$

where V_{Y_m} is the voltage across the mechanical lumped elements, which can be calculated by analyzing the mBVD circuit in Fig. 2.1(a).

2.2 Acousto-optics, Bragg diffraction, and Brillouin scattering

When the IDT excited acoustic wave encounters an optical wave which is propagating through the material, the light is diffracted to multiple directions [22]. The diffraction angles of the optical waves, or the Bragg angle, can be described heuristically as

$$2\Lambda \sin\theta_B = N\lambda, \tag{2.4}$$

where λ is the optical wavelength, Λ is the acoustic wavelength, and the integer N is the order to which the optics being diffracted. The refractive index grating formed from the traveling acoustic wave is analogous to the crystal plane in the material which causes the X-ray to constructively interfere at the Bragg angles in crystallography. However, the acoustic wave is a sine wave (could be longitudinal and/or transverse) unlike the sharp crystal plane. This effect can also be interpreted as the momentum conservation of a photon and a phonon collision

$$\kappa_2 = \kappa_1 \pm q, \tag{2.5}$$

where the outgoing light's wavevector κ_2 is a vector sum of the incident photon and phonon momentum κ_1 and q respectively. The Bragg angle can be easily derived from this relation as shown in Fig. 2.2(a). This momentum and energy conversion relation between acoustic and optical waves scattering is generally referred as acousto-optic interactions.

Brillouin scattering is similar to acousto-optics interactions. This is also a nonlinear effect that the photon absorbs or emits phonon energy which results in an optical frequency up-shift (anti-Stokes) or down-shift (Stokes). In spontaneous Brillouin scattering, the incident light emits phonon spontaneously and generates acoustic waves; in stimulated Brillouin scattering (SBS), phonon emission is enhanced by a seed laser with equivalent down-shifted energy, leading to the amplification of the scattered light and the generation of coherent phonons. The Brillouin interactions are usually optically driven processes through electrostriction. In a context more relevant to this work, the Brillouin process used here is driven through electromechanically generated acoustic waves using the IDTs [23, 24].

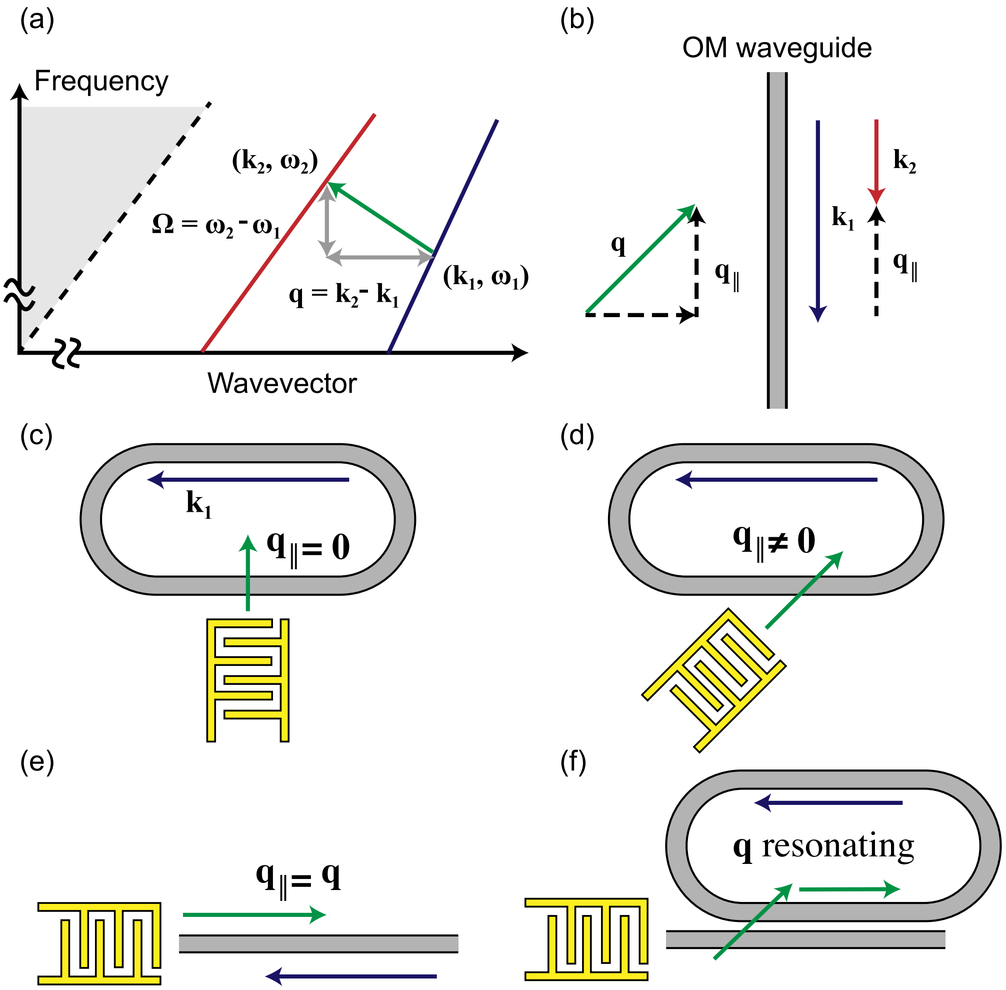

Figure 2.2: The principle intermodal scattering of guided optical modes and various types of integrated acousto-optomechanical device architecture. (a) Principle of intermodal anti-stokes scattering in a waveguide. (b) The phase-matching diagram of an optomechanical waveguide. (c)-(d) Categorization of different acousto-optomechanical interaction by the value of parallel acoustic wavevector $q_{||}$.

In an integrated photonic platform, the electromechanically excited acoustic waves have been used to scatter guided optical waves. In Fig. 2.2a, the red and blue solid lines represent the dispersion curve of two different optical modes propagating in a same waveguide. An *intra*-modal Brillouin scattering effect describes the guided optical mode being scattered within the same mode on the same dispersion curve. This is in contrast to *inter*-modal scattering, where the optical mode is scattered into a different mode (the mode jump from one to the other curve). The intra-modal scattering is particularly useful for applications requiring high spectral purity and low noise, as it preserves the mode structure of the optical signal.

A general goal of modern technology is to miniaturize existing tools' footprint, so one can engineer a more compact tool that has more functions, runs faster, and is more power efficient. Here is no different; we focus on packing integrated photonics and acousto-optic devices into smaller footprints. This involves the scattering of guided modes in waveguides or resonators, where the interaction of the light and sounds is confined to a wavelength-scale area. The guided modes' scattering can be broadly categorized by the acoustic and optical waves traveling direction with respect to the waveguides. In some of the earlier works of Brillouin scattering in integrated devices, the acoustic waves travels perpendicularly to the waveguides (Fig. 2.2c), where the acouto-optics interaction depends on the mode overlaps instead of momentum matching. A few representative works using such configuration are Tadesse et al. [25], Shao et al. [26], and Sohn et al. [23] The disadvantages of such perpendicular wave interaction are that the acousto-optic interactions are limited to one pass of the acoustic waves and a high-power microwave drive is required for efficient Brillouin scattering. The second category is a tilted IDT configuration, such as the work from Kittlaus et al. [27] and Zhou et al. [28], as shown in Fig. 2.2d. This configuration, while having a parallel component of the acoustic wavevector to the traveling optical waves, most of the acoustic energy still am not contributed to the acousto-optic interaction. A fully forward/backward Brillouin scattering process has been demonstrated in a waveguide as well, where the acoustic wave travels parallelly with the optical waves. Several attempts such as Liu et al. [24] and Zhang et al. [29]. Zhang et al. achieved an impressive near unity optical mode conversion in their work, but the footprint of the devices are not ideal, a long waveguide is needed (> 5mm) to achieve this unity mode conversion. Ideally, we would like an integrated circuit where both acoustic and optical modes co-propagate and resonant—an optomechanical integrated circuit—to achieve maximum scattering efficiency (Fig. 2.2f). This is the core idea of this thesis, and we will explore it more deeply in later chapters.

2.3 Cavity optomechanics

In contrast to Brillouin scattering in a free propagating medium, cavity-optomechanics describes the optical-mechanical interactions in a cavity [30]. We use cavity-optomechanics as an example to understand how resonant optical and mechanical modes interact. Here, we construct the model with a simple moving-mirror cavity and learn how to describe this system using Hamiltonian formalism. Then, we use these relations to introduce the concept of beam-splitter Hamiltonian and two-mode squeezing Hamiltonian, which are useful in performing microwave-to-optical transduction.

2.3.1 A moving-mirror cavity

We show a diagram of the moving mirror model (Fig. 2.3a). In this model, the optical cavity forms between the left-side optical mirror and a mechanical cavity structure which reflects the optical mode. The optical mode forms a standing wave between the left and right side reflectors. On the other hand, the mechanical cavity also supports a resonant acoustic mode. This system Hamiltonian can be written as

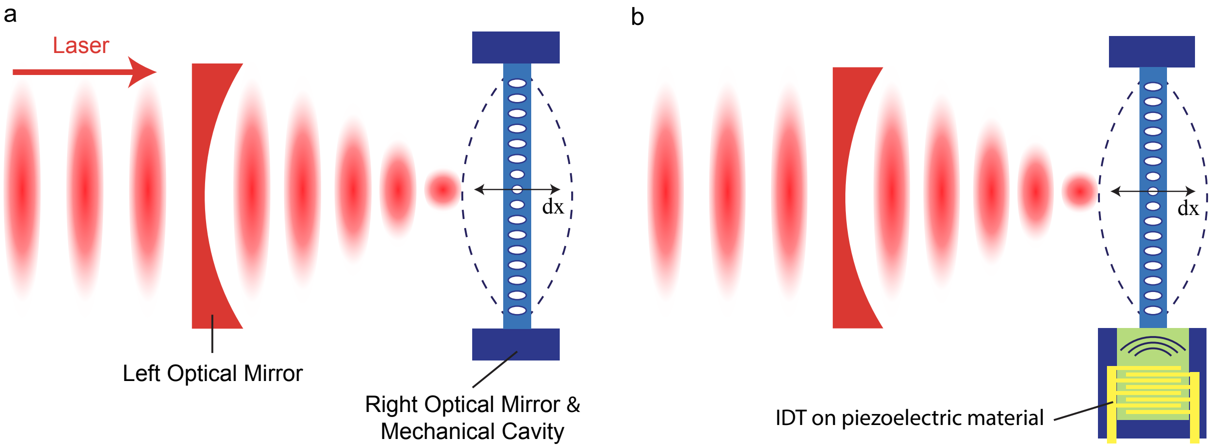

Figure 2.3: A moving mirror model. The moving mirror cavity consists of two optical mirrors while one of the mirrors is also a mechanical cavity which has acoustic resonant modes

$$\frac{H}{\hbar} = \Omega \hat{b}^\dagger \hat{b} + \omega_{\text{cav}} \hat{a}^\dagger \hat{a}, \tag{2.6}$$

where the $\hat{a}$ ($\hat{a}^\dagger$) are the optical mode annihilation (creation) operators and the $\hat{b}$ ($\hat{b}^\dagger$) are the mechanical mode annihilation (creation) operators. The ω (Ω) is the resonance frequency of the optical (acoustic) modes.

The optomechanical interaction starts when the radiation pressure from the photons simultaneously causes the mechanical cavity to deform dx, such that the optical resonance frequency shifts because of the change in optical cavity length. The optical resonance shift can be written as a function of the cavity length, which reads

$$\omega_{\text{cav}}(x) = \omega_0 + x \cdot \frac{\partial \omega}{\partial x}, \tag{2.7}$$

where x is the mechanical cavity displacement due to the radiation pressure from the photons. We then plug Eq. 2.7 into Eq. A.16 and write

$$\frac{H}{\hbar} = \Omega \hat{b}^{\dagger} \hat{b} + (\omega_0 - G\hat{x}) \hat{a}^{\dagger} \hat{a}, \tag{2.8}$$

where the optomechanical coupling coefficient $G \equiv -\frac{\partial \omega}{\partial x}$, and the displacement operator $\hat{x} = x_{\text{ZPF}}(\hat{b} + \hat{b}^{\dagger})$ and x_{ZPF} is the zero-phonon fluctuation of the mechanical mode at 0K. Finally, we can write the interaction Hamiltonian as

$$\frac{H_I}{\hbar} = g_0 a^{\dagger} \hat{a} (\hat{b} + \hat{b}^{\dagger}) + h.c., \tag{2.9}$$

where the vacuum optomechanical coupling coefficient $g_0 = G x_{\text{ZPF}}$. This is the well-known optomechanical interaction Hamiltonian, which describes the coupling between the optical and mechanical modes. This coupling leads to energy exchange between the modes, which can be used for various applications such as cooling of mechanical motion, amplification, and transduction between different frequency domains.

2.3.2 Beam-splitter and two-mode squeezing Hamiltonian

The optomechanical interaction Hamiltonian in Eq. 2.9 can be used to perform a quantum state exchange (a beam-splitter Hamiltonian), or to generate entangled pairs between the optical and mechanical modes (a two-mode squeezing Hamiltonian).

We consider a small perturbation in the optical mode $\hat{a} \rightarrow \bar{a} + \delta\hat{a}$ and replace the optical operators in Eq. 2.9. This leads to the linearized interaction Hamiltonian:

$$\frac{H_{\text{linear}}}{\hbar} = g_0[(\bar{a} + \delta\hat{a})\hat{b} + (\bar{a} + \delta\hat{a})\hat{b}^\dagger] + h.c., \tag{2.10}$$

where $\bar{a}$ is the steady-state amplitude of an optical mode, in other words, a classical optical pump. We note that the optical and acoustic modes here can be expressed as $\hat{a} = \bar{a}\exp(-i\omega t)$ and $\hat{b} = \bar{u}\exp(-i\Omega t)$, where $\bar{a}$ and $\bar{u}$ are the respective mode amplitudes. We also define a detuned frequency $\Delta = \omega - \Omega$. One can easily observe that at $\Delta = -\Omega$ (a 'red detuned' pump) and using the rotating-wave approximation (RWA) at the lab-frame (discarding the non-zero frequency terms), we arrive at a beam-splitter Hamiltonian

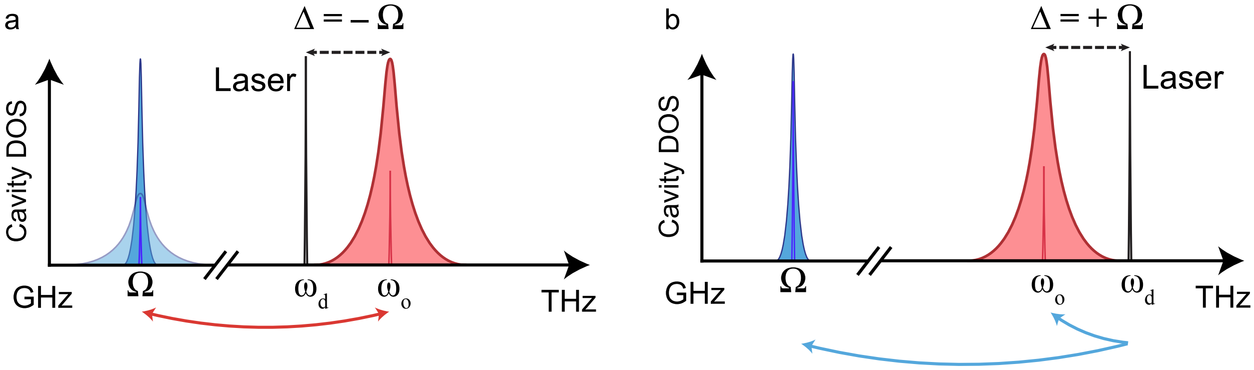

Figure 2.4: Spectral characteristics of Beam-splitter and two-mode squeezing pumping **a**. a red detuned pumping where the GHz mechanical phonons and THz photons exchanging energy. **b**. a blue detuned pumping that generates an entangled photon-phonon pair.

$$\frac{H_{\text{BS}}}{\hbar} = g(\delta\hat{a}\hat{b}^\dagger + \delta\hat{a}^\dagger\hat{b}), \tag{2.11}$$

where $g = g_0\bar{a}$ is the enhanced optomechanical coupling rate. A spectral characteristic of the red detuned pumping is shown in Fig. 2.4a. Conversely, choosing a $\Delta = +\Omega$ (a 'blue detuned' pump), the equation arrives at a two-mode squeezing Hamiltonian

$$\frac{H_{\text{TMS}}}{\hbar} = g(\delta\hat{a}\hat{b} + \delta\hat{a}^\dagger\hat{b}^\dagger). \tag{2.12}$$

A spectral characteristic of the blue detuned pumping is shown in Fig. 2.4b. These Hamiltonians are useful for describing quantum state transfer and entanglement generation between the optical and mechanical modes.

2.3.3 Optomechanical coupling rate

The coupling rate between the optical and mechanical modes is denoted by g_0, which represents the single-photon optomechanical coupling strength. This coupling rate depends on the overlap between the optical and mechanical modes and can be enhanced by increasing the intracavity photon number or by using resonant enhancement techniques.

$$\Delta \mathbf{P} = \Delta\varepsilon(x,y,z)\mathbf{E}_i(x,y)e^{i(\omega t - k_i z)}, \tag{2.13}$$

where k_i is the propagating wavevector of the i-th mode, $E_i(x,y)$ is the normal mode electric field of the i-th mode. The mechanical perturbation of the permittivity $\Delta\varepsilon$ consists of contributions from the moving boundary effect [31] and the photoelastic effect [32] and can be described as

$$\Delta\varepsilon = \delta\varepsilon \cdot \mathbf{u} = -\underbrace{\mathbf{u}(x,y)\cdot\mathbf{n}(x,y)(\Delta\varepsilon'|\mathbf{E}_{\parallel}(x,y)|^2 - \Delta\varepsilon'^{-1}|\mathbf{D}_{\perp}|^2)}_{\text{Moving boundary effect}} + \underbrace{\mathbf{u}\cdot\frac{\varepsilon\cdot p\mathbf{S}\cdot\varepsilon}{\varepsilon_0}}_{\text{Photoelastic effect}} \tag{2.14}$$

where $\mathbf{n}$ is the normal vector pointing from the dielectric 1 to dielectric 2; $\Delta\varepsilon' = \varepsilon_2 - \varepsilon_1$ and $\Delta\varepsilon'^{-1} = \varepsilon_2^{-1} - \varepsilon_1^{-1}$; $\mathbf{E}_{\parallel}$ and $\mathbf{D}_{\perp}$ are the tangential electric field and perpendicular displacement field at the dielectric boundary; p is the photoelastic tensor and $\mathbf{S}$ is the strain tensor. An acousto-optic figure-of-merit $\mathcal{M}_2 = n^6p^2/\rho v^3$ [33], which takes into account the photoelastic constant p, refractive index n, material density ρ, and acoustic velocity v, can be used to identify a range of material platform selections that is suitable for achieving strong OM coupling. Here we list the $\mathcal{M}_2$ of several materials in Table 2.2.

From Table 2.2, we can see that gallium arsenide (GaAs), gallium phosphide (GaP), and silicon (Si) have significant higher acousto-optic figure-of-merit $\mathcal{M}_2$ compared to other materials. This indicates that these materials are intrinsically suitable for strong optomechanical coupling, which is beneficial for applications such as microwave-to-optical conversion. In this thesis, we investigated GaP and Si as the optomechanical platform.

	k_{em}^2 (%)	n (1.55 μm)	p_{ij}	ρ (g/cm^3)	v_s (m/s)	$\mathcal{M}_2$(s^3kg^{-1})
AlN	7.2	2.19	$p_{11} = -0.1$	3.26	5760	1.7
GaAs	0.38	3.37	$p_{11} = -0.16$	5.32	4726	66.7
GaN	1.3	2.31	$p_{11} = -0.09$	6.15	3941	3.26
GaP	0.2	3.05	$p_{11} = 0.151$ [33]	4.13	4100	64.5
$LiNbO_3$	17.2	2.21	$p_{31} = 0.172$ [33]	4.64	3978	11.8
					(Y-cut)	
Si*	0	3.47	$p_{11} = -0.095$ (RT)	2.33	5845	36.1
			$- 0.160$ $(5K)$			60.6
ZnO	3.3	1.92	$p_{11} = -0.2$	5.61	3500	8.3

Table 2.2: Acousto-optic figure-of-merit $\mathcal{M}_2 \times 10^{-15}$ of selected materials that can be used in our system. The refractive index consider here is at 1550nm. * For silicon, the data for photoelastic constant at room temperature and cryogenic is calculated using the reference [5, 6, 7].

While $\mathcal{M}_2$ serves as an indicator for finding an ideal material platform, the modal overlap of the acoustic and optical fields also plays a significant role in enhancing the optomechanical coupling rate. The contribution from the moving boundary effect from Eq. 2.14 can be expanded as

$$G_{MB} = \frac{\int dA\mathbf{u}(x,y)\cdot\mathbf{n}(x,y)(\Delta\varepsilon'|\mathbf{E}_{\parallel}(x,y)|^2 - \Delta\varepsilon'^{-1}|\mathbf{D}_{\perp}|^2)}{\sqrt{\int dV\rho|\mathbf{u}|^2}\int dV\varepsilon|\mathbf{E}|^2}, \tag{2.15}$$

This is a mode overlap integration around the dielectric surface dA with thickness l and normalized by the acoustic and optical intensity in this dielectric volume V. Similarly, the photoelastic effect can be written as

$$G_{PE} = \int dV \frac{\varepsilon^2\mathbf{E}^*\cdot p\mathbf{S}\cdot\mathbf{E}}{\varepsilon_0\sqrt{\int dV\rho|\mathbf{u}|^2}\int dV\varepsilon|\mathbf{E}|^2} = \frac{\int dV\varepsilon_0 n^4\mathbf{E}\cdot p\mathbf{S}\cdot\mathbf{E}}{\sqrt{\int dV\rho|\mathbf{u}|^2}\int dV\varepsilon|\mathbf{E}|^2}, \tag{2.16}$$

where the normalized $G_{MB(PE)} = g_{MB(PE)}/-\frac{\omega}{2}\sqrt{\frac{\hbar}{2\Omega l}}$ and the refractive index $n = \sqrt{\varepsilon/\varepsilon_0}$. The photoelastic tensor p (6×6 matrix) of the material can be determined experimentally or found in literature, which has the following form

$$p = \begin{pmatrix} p_{11} & p_{12} & p_{12} & 0 & 0 & 0 \\ p_{12} & p_{11} & p_{12} & 0 & 0 & 0 \\ p_{12} & p_{12} & p_{11} & 0 & 0 & 0 \\ 0 & 0 & 0 & p_{44} & 0 & 0 \\ 0 & 0 & 0 & 0 & p_{44} & 0 \\ 0 & 0 & 0 & 0 & 0 & p_{44} \end{pmatrix}, \tag{2.17}$$

where p_{11}, p_{12}, and p_{44} are the photoelastic coefficients. We can rewrite the full photoelastic effect matrix multiplication as

$$G_{PE} = \frac{\varepsilon_0 n^4}{\sqrt{\int dV \rho |\mathbf{u}|^2 \int dV \varepsilon |\mathbf{E}|^2}} \int dV$$
$$\begin{pmatrix} E_{\mathrm{x}}^* & E_{\mathrm{y}}^* & E_{\mathrm{z}}^* \end{pmatrix} \begin{pmatrix} p_{11}S_{\mathrm{xx}} + p_{12}(S_{\mathrm{yy}} + S_{\mathrm{zz}}) & p_{44}S_{\mathrm{xy}} & p_{44}S_{\mathrm{xz}} \\ p_{44}S_{\mathrm{xy}} & p_{11}S_{\mathrm{yy}} + p_{12}(S_{\mathrm{xx}} + S_{\mathrm{zz}}) & p_{44}S_{\mathrm{yz}} \\ p_{44}S_{\mathrm{xz}} & p_{44}S_{\mathrm{yz}} & p_{11}S_{\mathrm{zz}} + p_{12}(S_{\mathrm{xx}} + S_{\mathrm{yy}}) \end{pmatrix} \begin{pmatrix} E_{\mathrm{x}} \\ E_{\mathrm{y}} \\ E_{\mathrm{z}} \end{pmatrix}. \tag{2.18}$$

Finally, the total optomechanical coupling coefficient can be written as

$$g_{om} = g_{MB} + g_{PE} = -\frac{\omega}{2}\sqrt{\frac{\hbar}{2\Omega l}}(G_{MB} + G_{PE}). \tag{2.19}$$

We can calculate this using a finite element analysis software such as COMSOL.

2.3.4 Heisenberg-Langevin equations and input-output formalism

The Heisenberg-Langevin equations and input-output formalism allows us to analyze the system dynamics in a steady state, whose input and output are measurable. We simplify the equation-of-motion (EOM) analysis by ignoring the second-order perturbation of the Hamiltonian (i.e., the

$\hat{a}_i\hat{a}_j$ terms). We can express the simplified EOM as

$$\dot{\hat{b}} = -(i\Omega + \frac{\kappa_b}{2})\hat{b} - iG\hat{a}_0 + \sqrt{\kappa_{e,b}}\hat{b}_{\mathrm{e}} + \sqrt{\kappa_{i,b}}\hat{b}_{\mathrm{i}} \tag{2.20a}$$

$$\dot{\hat{a}}_0 = -(i\omega_0 + \frac{\kappa_0}{2})\hat{a}_0 - iG\hat{b} + \sqrt{\kappa_{e,0}}\hat{a}_{\mathrm{e},0} + \sqrt{\kappa_{i,0}}\hat{a}_{\mathrm{i},0} \tag{2.20b}$$

where $\kappa_{(b,0)} = \kappa_{e,(b,0)} + \kappa_{i,(b,0)}$ is the total resonator linewidth of the OMR. The extrinsic decay represents the cavity coupling to an input channel, and the operator means the input optical drive, for instance, a waveguide coupling to the cavity with laser pump. The intrinsic decay represents the decay channel of the material defect or to surrounding environment, and the operator corresponds to the input from the thermal bath in the environment. We can further analyze the HOM with input-output formalism to understand the time evolution of the mechanical and optical operators. The EOM can be rewritten as a matrix form

$$\dot{\hat{\mathbf{s}}} = A\hat{\mathbf{s}} + B\hat{\mathbf{s}}_{\mathrm{in}} \tag{2.21a}$$

$$\hat{\mathbf{s}}_{\mathrm{out}} = C\hat{\mathbf{s}} + D\hat{\mathbf{s}}_{\mathrm{in}}, \tag{2.21b}$$

where $\hat{\mathbf{s}} = [\hat{b},\ \hat{a}_0]^T$, $\hat{\mathbf{s}}_{\mathrm{in}} = [\hat{b}_e,\ \hat{b}_i,\ \hat{a}_{e,0},\ \hat{a}_{i,0}]^T$, and $\hat{\mathbf{s}}_{\mathrm{out}} = [\hat{b}_{\mathrm{out}},\ \hat{a}_{\mathrm{out},0}]^T$. And the full-form of the transfer matrix can be written as

$$A = \begin{pmatrix} -(i\Omega + \frac{\kappa_b}{2}) & -iG \\ -iG & -(i\omega_0 + \frac{\kappa_0}{2}) \end{pmatrix},$$

$$B = \begin{pmatrix} \sqrt{\kappa_{e,b}} & \sqrt{\kappa_{i,b}} & 0 & 0 \\ 0 & 0 & \sqrt{\kappa_{e,0}} & \sqrt{\kappa_{i,0}} \end{pmatrix},$$

$$C = \begin{pmatrix} \sqrt{\kappa_{e,b}} & 0 \\ 0 & \sqrt{\kappa_{e,0}} \end{pmatrix},\ D = \begin{pmatrix} -1 & 0 & 0 & 0 \\ 0 & 0 & -1 & 0 \end{pmatrix}.$$

Using the input-output formalism, the transduction efficiency can be calculated by the scattering matrix

$$\hat{s}_{\mathrm{out}} = \mathbf{S}\hat{s}_{\mathrm{in}}, \tag{2.22}$$

and one can solve $\mathbf{S}$ by using the A, B, C, and D matrix. The solution of the scattering matrix would be

$$\mathbf{S} = C(-i\boldsymbol{\omega} - A)^{-1}B + D, \tag{2.23}$$

where

$$\boldsymbol{\omega} = \begin{pmatrix} \Omega & 0 \\ 0 & \omega_{0,\text{in}} \end{pmatrix}$$

is the driving frequency of the optical modes from the bus waveguide. By solving Eq. A.25, the input-output relation can be determined, and the scattering efficiency can be determined. The result for this example mode is written as

$$\begin{pmatrix} \hat{b}_{\text{out}} \\ \hat{a}_{0,\text{out}} \end{pmatrix} = \begin{pmatrix} \frac{\kappa_{eb}(i\delta_0+\kappa_0)}{G^2-\kappa_b(i\delta_0+\kappa_0)} - 1 & -\frac{G\sqrt{\kappa_{e0}}\sqrt{\kappa_{eb}}}{G^2-\kappa_b(i\delta_0+\kappa_0)} \\ -\frac{G\sqrt{\kappa_{e0}}\sqrt{\kappa_{eb}}}{G^2-\kappa_b(i\delta_0+\kappa_0)} & \frac{\kappa_b\kappa_{e0}}{G^2-\kappa_b(i\delta_0+\kappa_0)} - 1 \end{pmatrix} \begin{pmatrix} \hat{b}_{\text{e}} \\ \hat{a}_{e,0} \end{pmatrix}, \tag{2.24}$$

where the optical detuning $\delta_0 = (\omega_{0,\text{e}} - \omega_0)$, and the diagonal elements of the scattering matrix $\mathbf{S}$ are the microwave-optical conversion efficiency. At $\hat{\text{a}}_{0,\text{e}} = 0$ and zero optical detuning ($\delta_0 = 0$), the extrinsic microwave-to-optical conversion efficiency

$$\eta_{\text{ext}} = |\frac{\hat{a}_{0,\text{out}}}{\hat{b}_{\text{in}}}|^2 = |\frac{G\sqrt{\kappa_{e0}\kappa_{eb}}}{\kappa_0\kappa_b/4-G^2}|^2. \tag{2.25}$$

2.4 Previous works

In this section, we briefly review the current state-of-the-art quantum transducers. We limit the scope to electro-optics (EO) and piezo-optomechanics(OM) M2O transduction schemes, which shows great promise to be integrated with superconducting based qubit platforms. EO transducers require a strong χ^2 nonlinear coefficient for the material, but can direct convert a microwave photon to optical domain. In contrast, piezo-OM transducers operate through a two-step process: microwave photons are first converted to mechanical states, which are then converted to optical photons (Fig. 2.5). For a more general review on quantum transduction including magnon-mediated and atom-assisted conversion scheme, one can refer to [34].

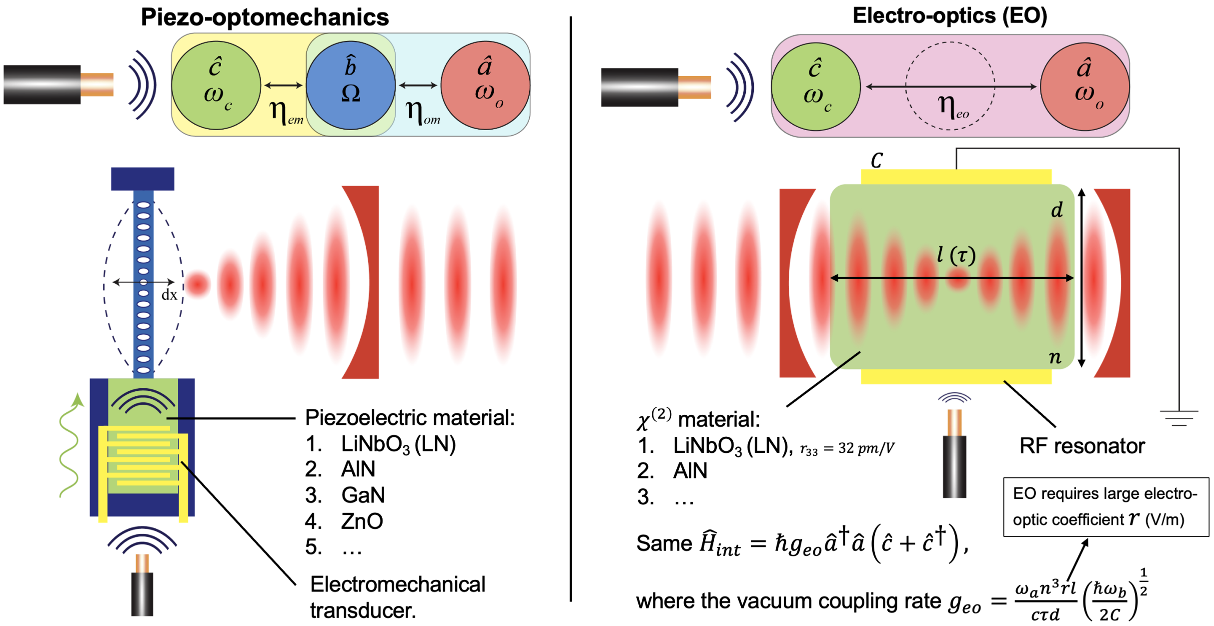

Figure 2.5: Different quantum transduction schemes. Operator $\hat{c}$ (ω_c), $\hat{b}$ (Ω), and $\hat{a}$ (ω_a) correspond to the annihilation operator (frequency) of the microwave photon, mechanical phonon, and optical photon mode, respectively. The efficiencies η_{em}, η_{om}, and η_{eo} correspond to the transduction efficiency of the electromechnical, optomechanical, and electro-optical process, respectively. **(Left)** Piezo-optomechanical transduction. **(Right)** Electro-optical transduction.

2.4.1 Cavity piezo-optomechanics

To perform a M2O transduction via cavity optomechanics, one needs to induce a mechanical motion using microwave photons. This can be achieved by piezoelectric effects in material. Advantages of using GHz piezoelectric effects is that thermal noise is significantly reduced at millikelvin temperatures (mK) and quantum ground state can be reached without any active cooling technique [35]. Furthermore, GHz mechanical devices can couple to superconducting qubits directly since the two have similar frequencies range [36, 37, 38]. Bi-directional M2O transduction has been showed in material platform such as AlN [39], GaAs [40], and $LiNbO_3$ (LN) [13]. More recently, LN-on-SOI platform demonstrated a bi-directional with a maximum total transduction efficiency $\eta = 0.9\%$ [41].

The main challenge in current optomechanical cavity design is the low heat dissipation from the suspended structure. The thermal noise comes from the strong red-side band pumping of the optical photons, which results in a heating from the residual phonon in the cavity [41].

2.4.2 Electro-optics

Electro-optic (EO) quantum transduction is a direct transduction scheme that uses Pockels effect $\chi^{(2)}$–a change in refractive index of materials Δn induced by the electric field–to directly interface microwave and optical photons. The design considerations to achieve a high transduction efficiency includes the selection of material with high $\chi^{(2)}$ coefficient, the cavity design with a large mode overlap between the RF and optical mode, while minimizing the mode volume. $LiNbO_3$ (LN), with its large EO coefficient $r_{33} = 31\ pm/V$, has been a popular choice for realizing EO transducers [42, 43]. There are also works on using low microwave loss material such as SiGe/Si platform with a high quality factor to design EO transducers [44].

Although EO transduction has shown promising results, strong optical pump [45] that is needed to achieve a high conversion efficiency, also leads to a large optical loss by the photorefractive effect [46]: impurities and defect centers in the crystal induce absorptions in the traveling optical mode. The charges generated by the optical pump then form a space-charge field in the waveguides that changes the refractive index. The photorefractive effect can be mitigated by metal doping [47]. Another way is to operate at a high temperature to increase the mobility of the impurities. However, this also increases the thermal noise in the cryogenic system which is not desirable. The centermeter-scale microwave cavities [48] that are often used to confine both the microwave and optical mode also limits the integratability of the EO transducer with on-chip qubits.

Chapter 3

Silicon-lattice-matched boron-doped gallium phosphide: a scalable acousto-optic platform

This study demonstrates that silicon-lattice-matched boron-doped GaP (BGaP), grown at the 12-inch wafer scale, provides similar functionalities as GaP. BGaP optical resonators exhibit intrinsic quality factors exceeding 25,000 and 200,000 at visible and telecom wavelengths, respectively. It further demonstrates the electromechanical generation of low-loss acoustic waves and an integrated acousto-optic (AO) modulator. High-resolution spatial and compositional mapping, combined with ab initio calculations, indicate two candidates for the excess optical loss in the visible band: the silicon-GaP interface and boron dimers. These results demonstrate the promise of the BGaP material platform for the development of scalable AO technologies at telecom and provide potential pathways toward higher performance at shorter wavelengths.

This chapter has been published as:

N. S. Yama*, **I. Chen***, S. Chakravarthi, B. Li, C. Pederson, B. E. Matthews, S. R. Spurgeon, D. E. Perea, M. G. Wirth, P. V. Sushko, M. Li, K.-M. C. Fu, Silicon-Lattice-Matched Boron-Doped Gallium Phosphide: A Scalable Acousto-Optic Platform. Adv. Mater. 2024, 36, 2305434.
* Equally contributing authors
https://doi.org/10.1002/adma.202305434

3.1 BGaP material characterizations

We choose the piezo-optomechanical transduction scheme because of its intergrability and scalability on chip. We also select a boron-doped gallium phosphide-on-silicon (GaP) platform to for its desirable acousto-optic (AO) properties. Optically, GaP has shown significant progress because of its large band gap (2.24 eV), high refractive index ($n = 3.34$ (3.05) at 600 (1550) nm [49]), and a large second-order nonlinearity ($\chi^{(2)} \sim 110$ pm/V [50]). Acoustically, GaP has a large AO figure-of-merit $\mathcal{M}_2 = 64.5(\times 10^{-15}\ \mathrm{s}^3\mathrm{kg}^{-1})$, which takes into account of the refractive index, the acoustic velocity, and the photoelastic constant of the material. The promising AO properties of GaP as a scalable acousto-optic platform has been experimental demonstrate in our recent work [1].

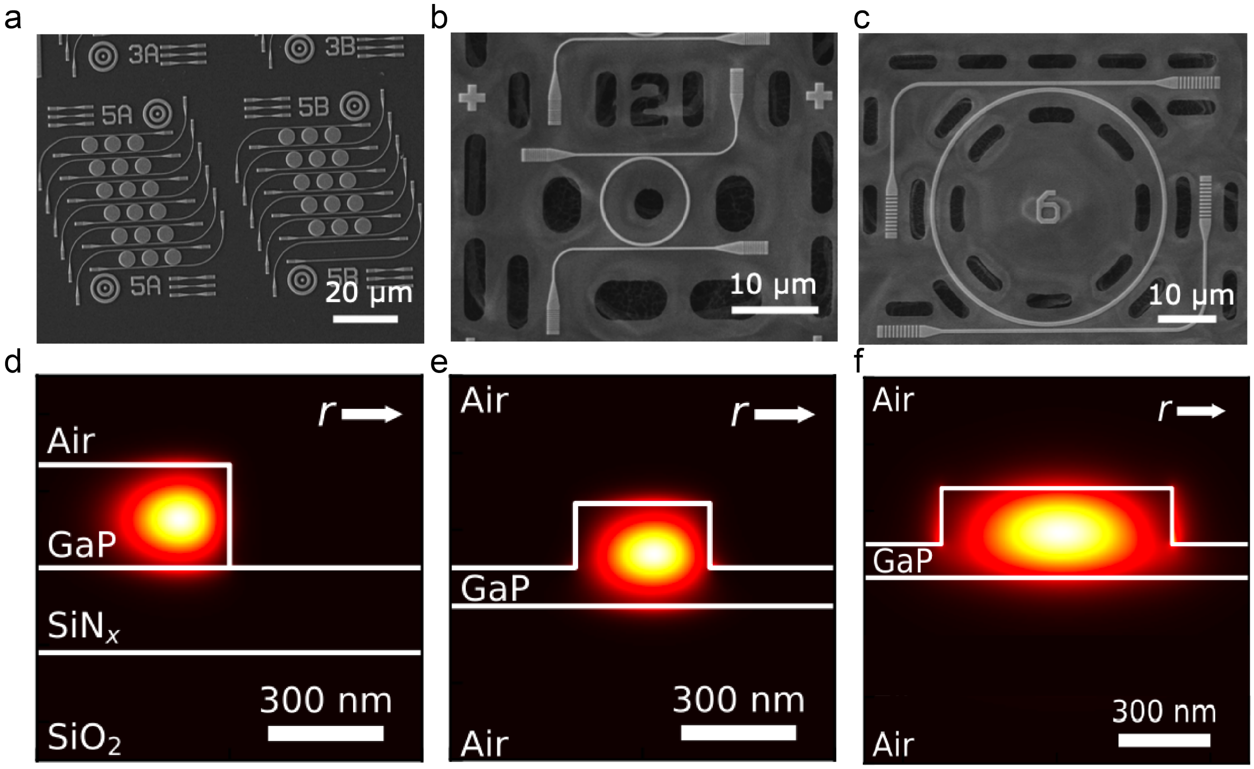

Figure 3.1: Visible and telecom-wavelengths GaP optical resonators [1]. **(a, b, c)** SEM image of the visible **(a)** GaP-on-SiN hybrid disk resonators, **(b)** suspended GaP devices, and telecom **(c)** suspended GaP ring resonators. **(d, e, f)** The simulated mode profiles for the visible **(a)** hybrid, **(c)** suspended devices, and telecom **(c)** suspended GaP ring resonators.

3.2 Optical characterization

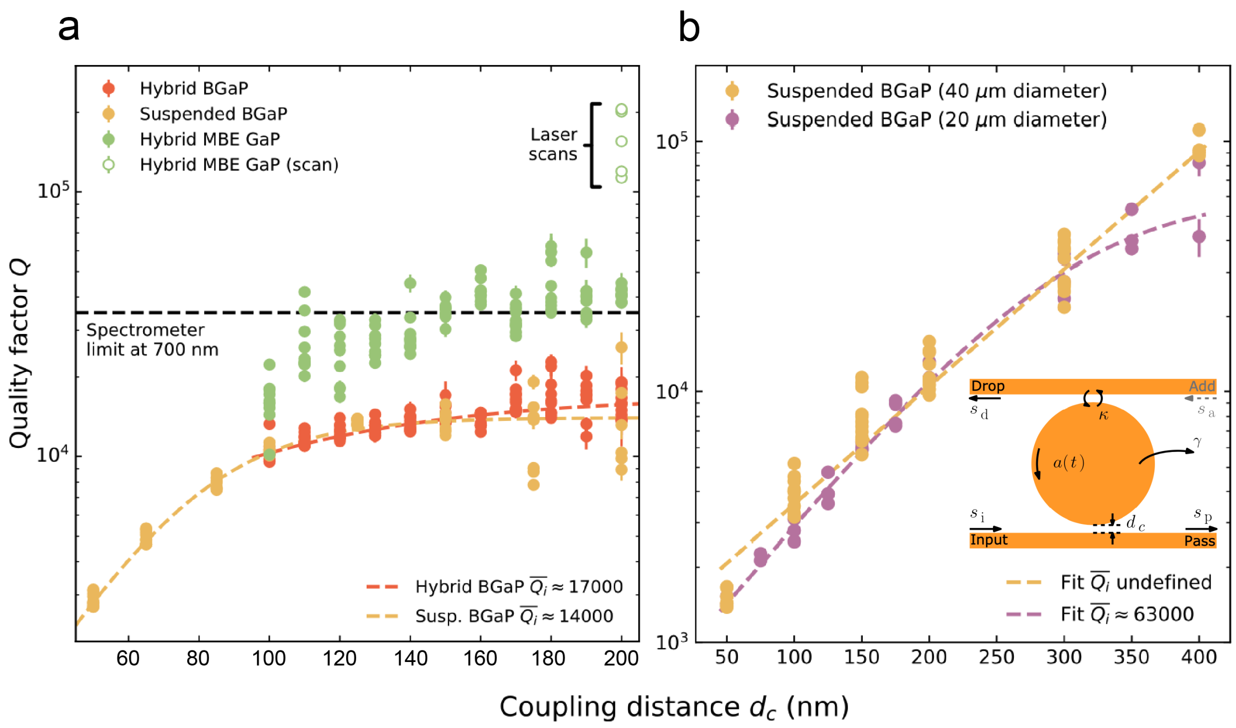

Figure 3.2: Extracted quality factor of the visible and telecom-wavelengths GaP optical resonators [1]. (a) The extracted loaded quality factor Q of the visible-wavelength GaP optical resonators as a function of the coupling distance d_c. **(b)** The extracted loaded quality factor Q of the telecom-wavelengths GaP optical resonators as a function of the coupling distance d_c.

We first investigate the optical properties of GaP at visible and telecom-wavelengths, and fabricate two types of devices: transferred GaP-on-SiN hybrid devices and suspended GaP devices, as shown in Fig. 3.1. For the visible range devices, the coupling distance d_c between the resonator and the waveguide are varied between 50–200 nm to control the coupling strength from under- to over-coupled regime. To characterize the intrinsic material quality of the GaP, we measure the optical transmission spectrum by exciting at the input port with a supercontinuum laser (600-800 nm) and collecting at either drop port or through port, as shown in the inset of Fig. 3.2b. The transmission signal is then received on a spectrometer with 0.02-nm-per-pixel resolution. The fitted quality factor for the visible range devices has the measured highest value of $Q \approx$ 16,000 on both the hybrid and suspended devices. We also compare our material with the GaP that is grown by molecular-beam epitaxial (MBE), as shown in Fig. 3.2a. Upon comparing the Q of the doped-GaP and the MBE growth GaP, the result suggests that our GaP's optical quality is limited by the intrinsic material loss at visible range.

On the telecom range devices, we use a laser-scanning transmission measurement to characterize the material at 1530–1565 nm. The coupling distance is varied between 50–400 nm. We can determine the intrinsic quality factor $Q_i \approx 200,000$ from the loaded quality factor shown in Fig. 3.2b. This suggests that the BGaP is a promising material for telecom-wavelengths AO devices. The reason of an increased optical loss at visible range is suspected to be the remaining silicon post-suspending at the GaP/Si interface and the excess boron which form interstitial defects in the material.

3.3 Acoustic Characterizations

The weak piezoelectric coefficient of BGaP call for a hybrid zinc-oxide (ZnO)-BGaP-Si combination to efficiently generate surface acoustic waves (SAW). The low speed of sound of BGaP ($v = 4100$ m/s) in contrast to that of silicon ($v \sim 8000$ m/s) ensures negligible loss into the substrate without thin-film suspension. We characterize the acoustic propagation loss on the BGaP-on-silicon by fabricating acoustic delay lines with different propagation length L, as illustrate in Fig. 3.3a. The interdigital transducers (IDTs) are used to excite SAW that propagates through BGaP slab, and the normalized RF transmission intensity $I/I_0 = e^{-\alpha L}$, where acoustic loss α can be determined with varying the propagation length L.

Similar to different optical modes in solids propagates with different group velocity and mode profile, different acoustic modes also carry different characteristics. In Fig. 3.3b, four resonances can be seen between 4–9 GHz in the RF reflection spectrum. The mode that propagates through the BGaP is the third-order Rayleigh mode (R_3) at 7.5 GHz, where most of the acoustic energy concentrates in BGaP (inset of Fig. 3.3b). After we identified the acoustic modes, we measure the radio-frequency (RF) transmission of the delay lines with different propagation distance L and extract the room-temperature and 4 K acoustic loss $\alpha_{RT} = 5.6$ dB/cm and $\alpha_{4K} = 0.9$ dB/cm.

The acoustic loss in solids can be attributed to both temperature-dependent thermal phonon scattering and temperature-independent material defect loss channel. We fit the attenuation $\alpha(T) =$

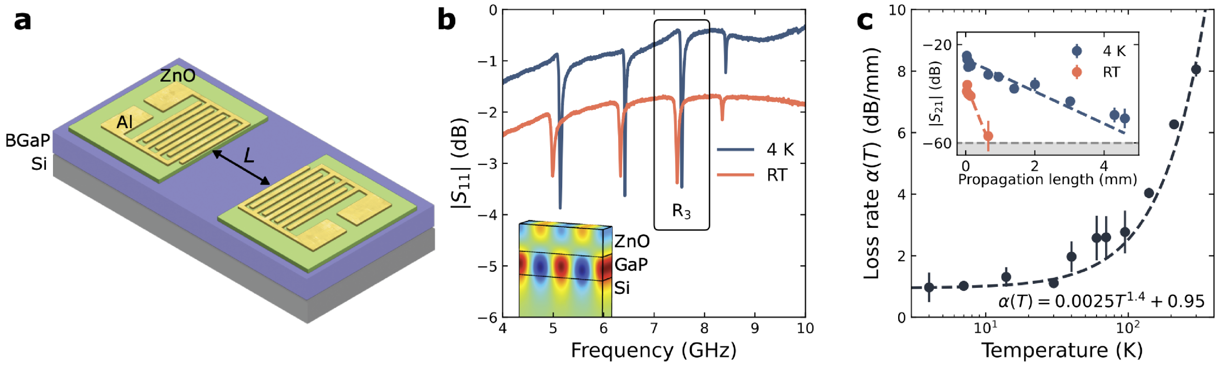

Figure 3.3: Acoustic delayline and radio-frequency (RF) acoustic spectrum [1]**. (a)** An illustration of the acoustic delay line device with a pair of interdigital transducers (IDTs) on the ZnO-BGaP-Si structure. The acoustic propagation length is L. **(b)** RF reflection spectrum (S_{11}) of the IDT. The inset shows the simulated third-order Rayleigh mode (R_3) profile. **(c)** The acoustic propagation loss as a function of temperature (4 K–300 K). The inset shows the RF transmission intensity of the acoustic wave as a function of propagation length L.

$bT^n + \alpha_0$ to determine dominate loss channel in BGaP. The resulted $n = 1.40$ and the temperature-independent loss $\alpha_0 = 0.95$ (Fig. 3.3c). n characterize the temperature-dependent loss, where 1.4 suggests thermal phonon scattering dominates the loss in BGaP [51], and α_0 is comparable to that of $LiNbO_3$-on-sapphire material platform ($\alpha_0 = 0.7$ dB/cm at 4 K) [52].

3.4 Acousto-optic frequency shifter (AOFS)

Now we turn our attention in realizing an acousto-optic frequency shifter (AOFS) on our suspended BGaP platform. An optical image of the fabricated AOFS is shown in Fig. 3.4a. We fabricated the AOFS on a suspended BGaP which consists of four optical grating couplers and one IDT in the middle on a ZnO layer. The IDT are made of aluminum fingers with a period $\Lambda = 650$ nm. The optical operation wavelength $\lambda = 1550$ nm, and the Bragg deflection angle θ_B satisfying

$$sin(\theta_B) = \frac{\lambda}{2\Lambda n_{\text{eff}}}, \tag{3.1}$$

where the effective index of the optical mode $n_{eff} = 2.5$, yielding $\theta_B = 27°$.

When the phase-matching condition between a photon with frequency ω and a phonon with frequency Ω is satisfied, the incident photon will either absorb $\omega + \Omega$ (anti-Stokes) or emit $\omega - \Omega$

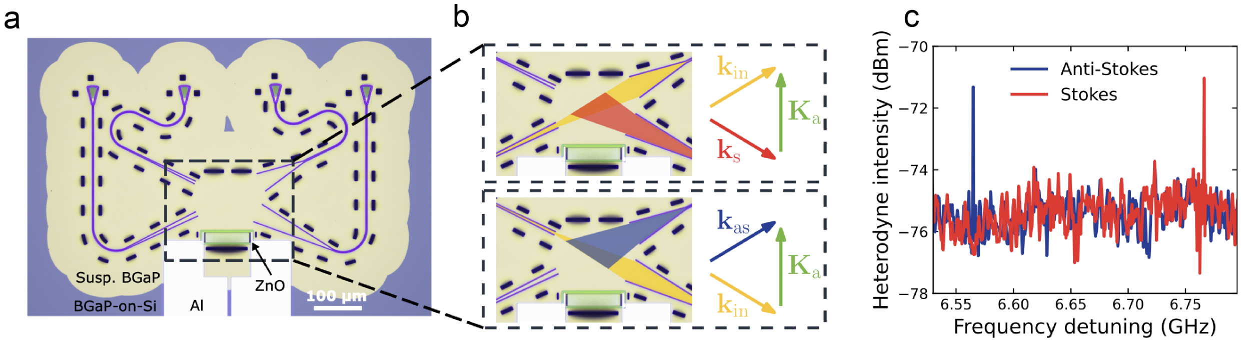

Figure 3.4: An acousto-optic frequency shifter (AOFS) [1]. **(a)** An optical image of the fabricated AOFS. The light-green area is the suspended BGaP film. The purple area is the as-grown BGaP on Si area. The ZnO is under the aluminum metal fingers at the bottom middle of the image. **(b)** Stokes and anti-Stokes phase-matching condition for the AOFS. The red and blue area are the collecting area of Stokes and anti-Stokes photons, respectively. The yellow area is the incident photon direction. The green arrow is the acoustic wave propagation direction. **(c)** The measured heterodyne beating signal of the generated Stokes and anti-Stokes photons.

(Stokes) a phonon. We can then detect the frequency shifting using a high-speed photodetector, as show in Fig. 3.4c. The detected signal is the beating signal with a reference laser signal that is shifted by a commercial AOFS with $\delta/2\pi = 102.9$ MHz. We can clearly observe the Stokes and anti-Stokes signal at $\Omega \pm \delta$. The results demonstrated the first AOFS using a hybrid ZnO-BGaP combination, the current efficiency is $< 0.1\%$, but further improvement can be done by using a guided acoustic wave instead of a slab mode that increases the overlap between the optical and acoustic mode.

The AOFS scattering efficiency is mainly limited by the short AO interaction length and the poor mode confinement of both acoustic wave and optical wave at the active region. Integrated photonic have shown significant progress [53], where high quality factor ring resonators fabricated on chip [54, 55] and low-loss waveguides that route the optical signal to different active region. Conversely, integrated phononics has gain traction in recent years, where wavelength-scale optomechanical waveguides [56, 57] confine both acoustic and optical mode in a small mode volume. Yet, an optomechanical ring resonator (OMR) that holds both co-resonating photons and phonons is still missing due to the lack of material platform [58]. Table 3.1 lists common AO material platforms with corresponding acoustic loss α. Our work using hybrid ZnO-BGaP-on-Si has a similar acoustic loss to LN at GHz level, which provides flexibilities and benefits over LN in optical domain.

Reference	Material Platform	$\Omega/2\pi$ (GHz)	η_{em} (%)	α (dB/mm)
[59] (2019)	GaN-on-sapphire	0.188-0.196	0.03 (-35dB)	0.05 (RT) 0.003 (50 mK)
[24] (2019)	Suspended AlN	16.2	17	N/A
[58] (2021)	LN†-on-Sapphire	3.4	~60	$4.9^* \pm 1.6$ (RT) $0.7^* \pm 0.2$ (4 K)
[57] (2021)	Suspended LN	0.440	~60	N/A
[60] (2022)	Bulk LN	2.5	x	1.7 (RT) 0.5 (77 K)
Our Work [1] (2023)	BGaP-on-Si	7.5	90 (4 K)	5.6 (RT) 0.9 (4 K)

† $LiNbO_3$ (LN) * α is converted from mechanical quality factor $Q_m = 5000$ (7×10^4) at RT (4 K).

Table 3.1: Integrated phononic circuit properties of different material platforms

3.5 Summary

We have demonstrated high-performance optical resonators and on-chip acousto-optic devices, fabricated with commercially available lattice-matched BGaP grown on silicon. Measured intrinsic optical quality factors in the telecom C band exceeding 200,000 and low acoustic losses comparable to leading materials are extremely promising for immediate integration in both nonlinear [55, 61] and optomechanical devices [62, 63, 64]. Likewise, strong visible-wavelength quality factors exceeding 25,000 suggest good prospects for the development of small-mode-volume, defect-integrated nanophotonic resonators [65] in the near term. Our investigation revealed two potential sources of loss in the visible band: imperfections in the GaP/Si interface and optically active boron defects; both of which can be addressed by modification to the growth process, such as by the inclusion of additional buffer layers (e.g. AlGaP [65]) and further optimization of the boron content [66]. Such improvements, combined with its strong AO properties and inherent scalability, would enable BGaP to be an ideal platform for the development of next-generation integrated photonic devices.

3.6 Device Fabrication

Membrane transfer for hybrid devices

The commercial BGaP-on-Si wafer was covered in a protective photoresist layer (AZ1512, MicroChemicals) and diced into 1 cm×1 cm chips. For the chips used in the hybrid devices, the silicon backside was mechanically thinned to 75 µm. The protective resist was stripped in solvent and a new layer of AZ1512 was spun on. Aligned-mask photolithography (ABM) was then performed in order to define individual membranes with vias for wet transfer. Individual membranes are 1.5 mm×1.5 mm and have rectangular vias defined at 250 µm intervals. After developing the resist, the exposed BGaP is etched in an Ar:Cl_2:N_2 inductively coupled plasma reactive ion etch (ICP-RIE) to transfer the membrane pattern into the BGaP layer. The chip is then cleaved between the membranes for individual use. A single-membrane chip is then flipped onto a sapphire substrate (silicon side facing up) and the sample is exposed to a XeF_2 vapor etch (SPTS) to remove the remaining silicon. The BGaP membrane adheres to the sapphire substrate which is then submerged in water, releasing the membrane onto the surface (the resist is hydrophobic and orients upward). The membrane can then be picked up on the target substrate (SiN_x in this work) and allowed to dry. After drying the adhesion to the substrate increases and the remaining photoresist can be stripped in solvent.

Photonic device fabrication

Starting with either a BGaP-on-Si or transferred BGaP-on-substrate chip, the sample is cleaned in a solvent rinse and allowed to dehydrate on a hotplate at 150°C. Electron-beam lithography (EBL) resist, hydrogen silsesquioxane (HSQ), is spun on to around 100 nm thick and soft baked at 80°C. The photonic structures are then patterned in EBL and the HSQ is developed in a 25% tetramethylammonium hydroxide (TMAH) bath. The device pattern is transferred to the BGaP layer by ICP-RIE either completely etching through the membrane (as in the hybrid devices) or partially etching the membrane. If the devices need to be suspended then AZ1512 photoresist is spun on and etch vias are patterned using an aligned direct write (Heidelberg DWL66 plus). The resist is developed and the etched vias are defined in ICP-RIE. At this stage XeF_2 vapor etch is used to undercut the silicon substrate for the suspended devices.

Photonic device design

Hybrid resonators. Three disk resonators, with center-to-center separation of 7 µm, are placed along the coupling waveguides. The disk resonator diameters are varied by 10 nm such that, from left to right, the diameters are 4.99, 5.00, and 5.01 nm respectively to separate the modes for increased device yield. The coupling waveguide is designed to have a width of 150 nm which allows for a single, low-loss TM mode to propagate. The BGaP membrane is 250 nm, whereas the MBE GaP membrane (undoped) is around 290 nm. Lossy TE modes also exist but are not considered in this work. Coupling distance d_c in the main text is measured from the edge of the waveguide closest to the disks and the edge of the 5.00-µm disk.

Suspended resonators. Visible wavelength ring resonators are designed to have a diameter of 10 µm and width of 350 nm as measured from the center of the ring. Telecom wavelength ring resonators have diameters of 20 or 40 µm and widths of 750 nm. The visible- and telecom-wavelength waveguides are 250 and 600 nm respectively with coupling distances similarly measured from the edge of the waveguide closest to the ring and the outer edge of the ring. For a BGaP membrane of about 250 nm in height, the targeted partial etch depth was 170 nm to enable sufficient confinement of the modes while also providing mechanical support. The final partial etch depth, as determined by profilometer measurements (Fig. 3.5b) is 168 nm.

Suspended AO device fabrication

The BGaP photonic waveguides and grating couplers are patterned with EBL using PMMA resist. The pattern is transferred into BGaP by partial etching via ICP-RIE using chlorine-based chemistry. The 290 nm thick ZnO film is deposited using an RF magnetron sputtering system and lifted-off in a sonicated acetone bath. The IDT pattern is written using the EBL and lifted-off after depositing 220 nm aluminum film using an electron-beam evaporator. The releasing vias are patterned with photolithography and etched in ICP. Finally, XeF_2 etching of silicon is used for suspending the BGaP layer.

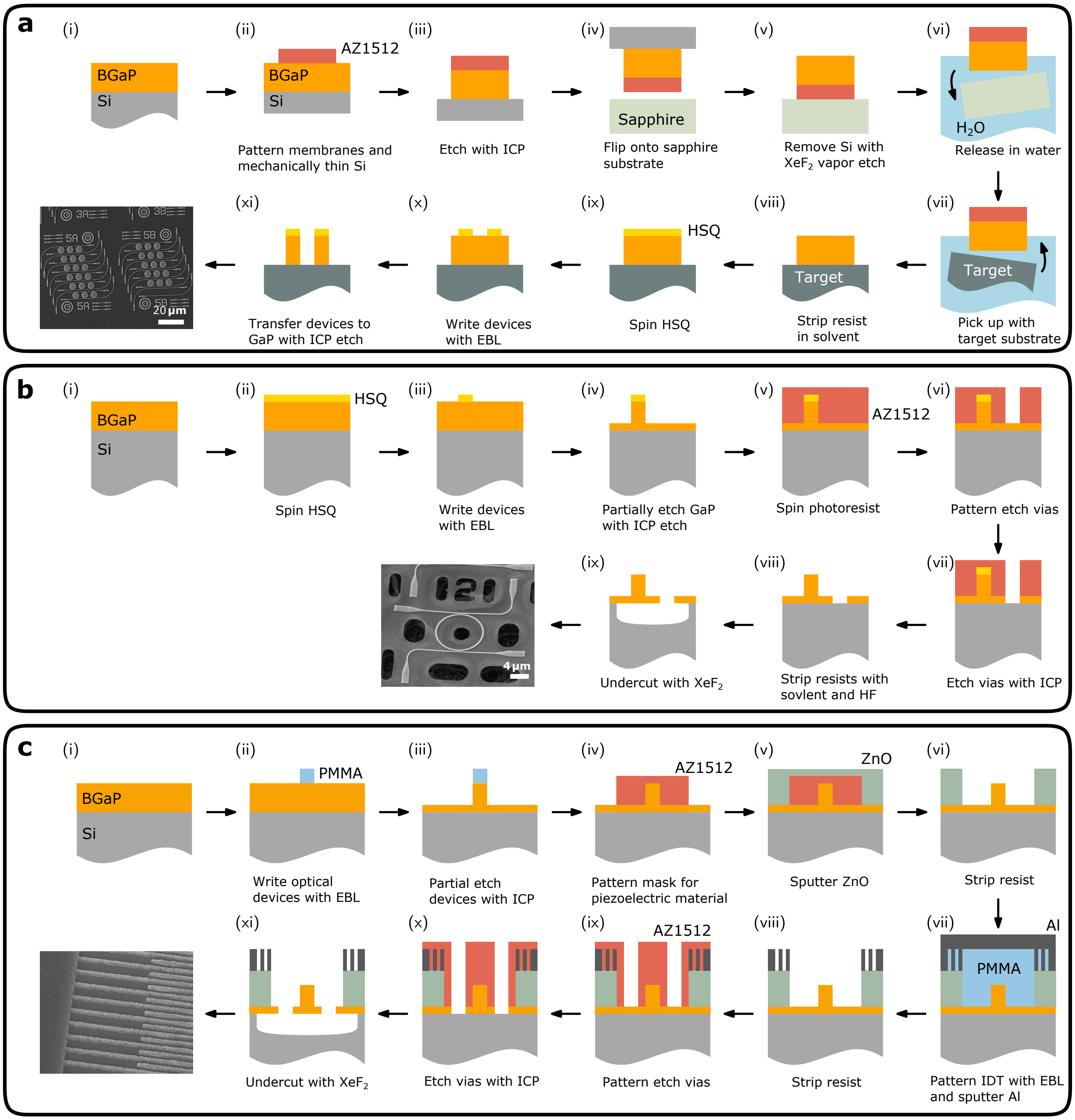

Figure 3.5: Fabrication process [1].Schematic representations and end results of the fabrication processes for **(a)** hybrid devices, **(b)** suspended photonics, and **(c)** suspended AO devices.

Chapter 4

Optomechanical ring resonator for efficient microwave-optical frequency conversion

Here, we demonstrate an OMIC including an optomechanical ring resonator (OMR), where co-resonant infrared photons and GHz phonons induce significantly enhanced interconversion. The platform is hybrid, using wide bandgap semiconductor gallium phosphide (GaP) for waveguiding and piezoelectric zinc oxide (ZnO) for phonon generation. The OMR features photonic and phononic quality factors of $> 1\times10^5$ and 3.2×10^3, respectively. The optomechanical interconversion between photonic modes achieved an internal conversion efficiency and a total device efficiency at a low acoustic pump power of 1.6 mW. The efficient conversion in OMICs enables microwave-optical transduction for quantum information and microwave photonics applications.

This chapter has been published as:

Chen, IT., Li, B., Lee, S. et al. Optomechanical ring resonator for efficient microwave-optical frequency conversion. Nat Commun 14, 7594 (2023).
https://doi.org/10.1038/s41467-023-43393-x

4.1 Optomechanical ring resonator (OMR)

Although photonic integrated circuits have become a mature technology, the development of phononic integrated circuits is still at an early stage [67, 68, 69, 70, 71]. The photonic ring resonator is a crucial component in photonic integrated circuits, as it allows for efficient electro-optic modulation, frequency comb generation, wavelength filtering, routing, and switching. Similarly, phononic ring resonators are expected to play an important role in phononic circuits and have been recently demonstrated in various materials, such as lithium niobate and gallium nitride (GaN) on sapphire substrates and GaN on silicon carbide. A ring resonator for both photons and phonons—an optomechanical ring resonator (OMR)—would resonantly enhance the interaction between co-circulating photons and phonons to achieve ultrahigh optomechanical coupling efficiency, thus highly desirable for the abovementioned applications. Wavelength scale optomechanical waveguide that confines both photons and phonons for optomechanical conversion has recently been demonstrated. However, realizing OMRs with high quality factors requires low-loss waveguides for both photons and phonons, as well as a phonon source that can generate phonons in resonance with the ring. As macro scale acoustic and optical co-resonator has been demonstrated using high-overtone bulk acoustic resonators (HBAR), integrated OMR with photonic and phononic mode in co-resonance has yet to been demonstrated. Therefore, its realization faces challenges in material selection, structure design, and device fabrication and thus remains elusive to date. Such OMRs interconnected in optomechanical integrated circuits (OMIC) would offer a wide range of applications in both classical and quantum domains. These applications include quantum transduction, single-photon gate operations, nuclear spin control, mechanical control of defect centers, frequency comb generation and modulation, frequency conversion, and non-reciprocal optical devices.

Here, we demonstrate an OMR built on a hybrid material platform, on which non-piezoelectric material gallium phosphide (GaP) is used as the optomechanical photon-phonon guiding layer and combined with piezoelectric material zinc oxide (ZnO), which is used to electromechanically generate phonons. The hybrid approach allows us to exploit the best properties of both materials: GaP provides a high optical refractive index (n = 3.1 at 1.55 μm wavelength), a large band gap (2.26 eV), a high $\chi^{(2)}$ nonlinearity, and a high optomechanical figure of merit, while ZnO possesses strong piezoelectricity and can be easily sputtered as a thin film. Moreover, boron-doped GaP can be grown epitaxially on silicon wafers by commercial vendors (see Methods and Supplementary Note 6), enabling a scalable platform to build large-scale optomechanical integrated circuits (OMICs). To enable waveguiding of both photons and phonons, the GaP layer must be suspended from the silicon substrate. This configuration allows us to achieve high quality factors and high optomechanical coupling efficiency, making the ZnO/GaP hybrid a promising platform. In this section, we demonstrate the first OMR that uses a hybrid platform of suspended ZnO-BGaP where electromechanically generated phonon and optical photon are coupled and form a strong optomechanical scattering that leads to an efficient microwave-optical frequency conversion.

The OMR supports two photonic modes and one photonic mode with angular frequency and wavevector of (ω_0, β_0), (ω_2, β_2), and (Ω, κ) respectively. The frequency difference of the two photonic modes are designed to match the acoustic mode ($|\omega_2 - \omega_0| = \Omega$) while satisfying the phase-matching condition ($|\beta_2 - \beta_0| = \kappa$). A counter-propagating anti-Stokes case that satisfies both conditions is illustrated in Fig. 4.1a. The coupling coefficient g of the three modes be expressed as

$$g = \frac{G}{\sqrt{\phi}} = -\frac{\omega_0}{2} \frac{\int dA \mathbf{E}_0^* \cdot \delta\epsilon \cdot \mathbf{u}(x,y) \cdot \mathbf{E}_2}{P_2\sqrt{\Phi}}, \tag{4.1}$$

where the electric field $\mathbf{E}_0$ (TE_0) and $\mathbf{E}_2$ (TE_2) are the waveguide cross-sectional mode profile and $\mathbf{u}$ is the cross-sectional acoustic displacement field (Fig. 4.1b). The three modes are chosen such that the integral in Eq. 4.1 is non-vanishing.

4.2 Device characterization

We first characterize the optical properties of the OMR. The optical part of the OMR consist of 4 ports, where 2 of the ports are for TE_0 mode coupling and 2 for TE_2 mode (Fig. 4.2b). The coupling region is essentially a mode convertor, one side (optical input port in Fig. 4.2c) allows the TE_0 to be coupled to the OMR and the other side (optical drop in Fig. 4.2c) coupled out the TE_2 mode that is circulating in the OMR by spatially filter out the TE_0 mode. The measured highest loaded optical quality factor $Q_{ol} = 7.5 \times 10^4$, which corresponds to an intrinsic optical quality factor

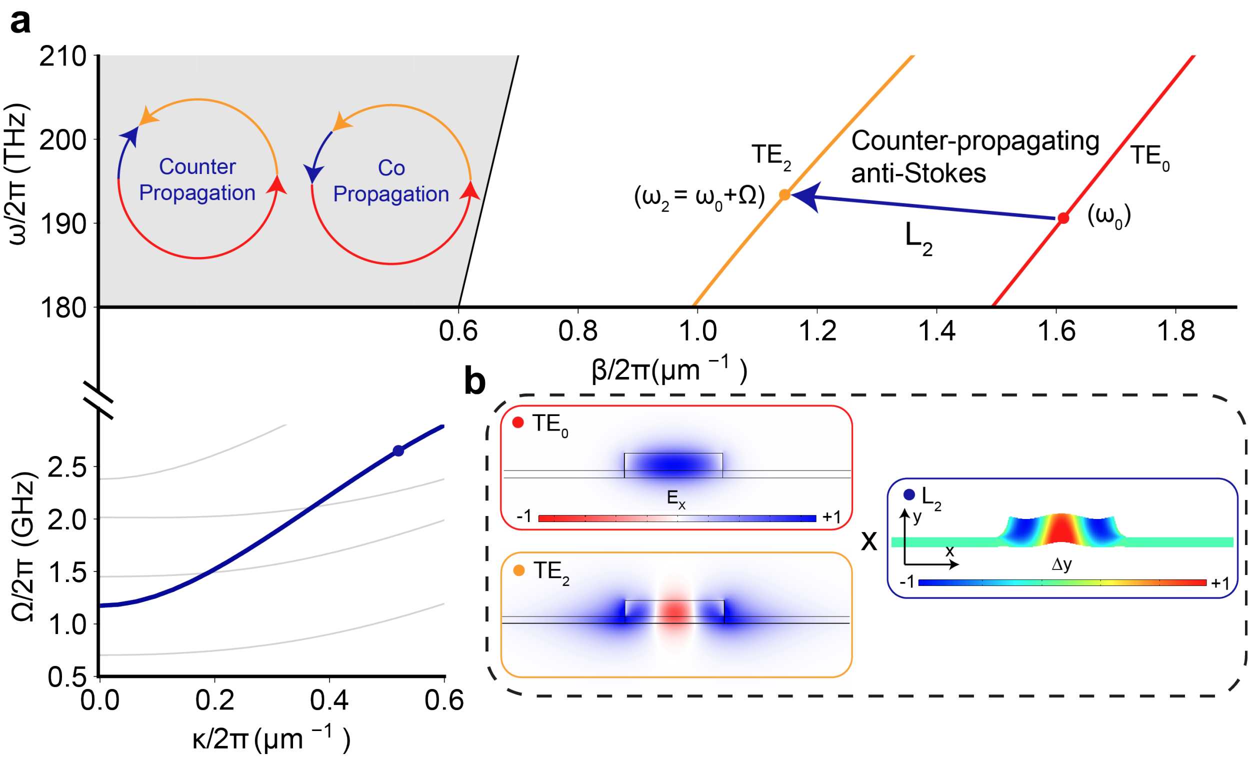

Figure 4.1: Co-resonating photon-phonon mode in an optomechanical ring resonator [2]. (a) (top penal) The photonic mode TE$_0$ and TE$_2$ dispersion curve. **(a)** (bottom penal) The phononic mode second-order Lamb mode (L$_2$) dispersion curve. **(b)** The mode profile of TE$_0$, TE$_2$, and L$_2$ mode, respectively.

$Q_{oi} = 1.5 \times 10^5$ (Fig. 4.2e).

After the optical characterization, radio-frequency (RF) reflection (S_{11}) and transmission (S_{21}) spectrums are measured using a vector network analyzer (VNA) at cryogenic temperature. In the S_{11} spectrum, a sharp resonance is observed at 2.5 GHz (Fig. 4.2c), which corresponds to the designed L$_2$ mode, as confirmed by COMSOL simulations. We also observe a resonance frequency shift between RT and 4 K, this is due to the temperature-dependent impedance of the aluminum metal fingers that are used to generate the acoustic waves. The S_{21} of the OMR is similar to an optical ring transmission spectrum, which shows an overall broad peak with small dips within (Fig. 4.2f). The small dips correspond to the acoustic mode resonance in the OMR, and the broad peak corresponds to the bandwidth of the IDT. From the resonance dips in the S_{21} spectrum, we can extract the acoustic quality factor $Q_m = 3200$ at 4 K, which correspond to an acoustic propagation loss $\alpha = 6.2$ dB/mm. The measured Q_m is limited by the temperature-independent intrinsic material loss, which is due to the interstitial boron defects [1].

4.3 Time-reversal symmetry breaking in OMR

Now we have characterized the OMR, we can then investigate the optomechanical coupling between the optical and acoustic mode. We first input the photonic mode without the phononic mode, and the observed TE_2 mode intensities are recorded as the reference signal (Fig. 4.3c, d). We then input the photon and phonon modes simultaneously and observe the optical output. The phase-matching condition (PMC) is satisfied when the energy and momentum are both converted. The PMC manifests as the counter-propagating anti-Stokes scattering, which the output TE_2 mode photon are created by the same amount as the input TE_0 mode photon annihilated. We tune the laser to be optically on resonance with the OMR and RF driving to be acoustically resonance, but with different propagating direction. The output TE_2 is detected using an optical spectrum analyzer (OSA). We observe a TE_2 intensity increases as the photon and phonon are traveling in the counter-propagating direction (Fig. 4.3a, f). And when the photonic and phononic modes are traveling on the opposite direction, the TE_2 intensity decreases (Fig. 4.3b, e). This is a clear demonstration of time-reversal symmetry breaking in the OMR. However, this measurement cannot resolve the frequency shifting of the output TE_2 mode due to the unresolved sideband regime that we are operating in.

4.4 Efficient microwave-to-optical frequency conversion

After the initial observation of the increased TE_2 output from the OSA, we now investigate the frequency shifting of the output TE_2 mode. We use heterodyne detection scheme to measure the frequency shift of the output TE_2 mode. The input microwave signal is generated by a microwave source and amplified by a microwave amplifier. The microwave signal is then sent to the IDT to generate the acoustic wave. The optical input is a continuous-wave (CW) laser that is tuned to be on resonance with the OMR, as shown in Fig. 4.4a. The optical signal is also sent to a beam-splitter, where a reference signal generated by the table-top AOFS that shifts the pump laser by $\delta/2\pi = 102.9$ GHz. This is then mixed with the output optical signal. The mixed signal is then detected by a high-speed photodetector (PD) and sent to a real-time spectrum analyzer (RSA). In the output spectrum (Fig. 4.4b), three distinct frequency appears from the output mixed signal between 2.4–2.7 GHz. We attribute the peaks $P_{02}(\Omega - \delta)$ and $P_{02}(\Omega + \delta)$ to the anti-Stokes and the Stokes scattering of the output. The signal $P_{02}(\Omega)$ is the beating signal between the scattered signal and the Rayleigh scattered TE_2 mode (frequency unshifted).

We detune the RF driving frequency and measure the output spectrum again, we find the two consecutive maximum output signal are separated by a frequency of 5.1 MHz, which corresponds to the FSR of the acoustic signal (Fig. 4.4). Finally, we trace the output optical power of the $P_{02}(\Omega - \delta)$ and the $P_{02}(\delta)$ as a function of RF driving power as in Fig. 4.4e and d, respectively. The output power shows oscillations between the reference signal and the generated TE_2 signal, which is an indication of high optomechanical coupling coefficient.

	[39]	[13]	[40]	[72]	[38]	This work [2]
$g_{om,0}$ [Hz]	115×10^3	80×10^3	1.3×10^6	19×10^3	$\sim 0.5 \times 10^6$	–
G_0 $[\frac{1}{\mathrm{mm}\sqrt{\mathrm{W}}}]$	–	–	–	–	–	230
C_{om}	3×10^{-3}	5×10^{-3}	1.7	0.4	0.04	3.35
C_{em}	–	–	–	7	~ 150	626
η	$\times 10^{-8}$	$\times 10^{-5}$	$< 3.5 \times 10^{-10}$	7.4×10^{-4}	8.8×10^{-6}	1.37×10^{-5}
η_{in}	NR	0.026	NR	0.058	10^{-3}	0.021
$\frac{\mathrm{B}}{2\pi}$ [MHz]	~ 1	~ 1	NR	1	1	10
n_{add}	NR	NR	NR	NR	0.57	0.07
T_{env} [K]	~ 300	~ 300	0.02	0.9	0.015	4

Table 4.1: GHz Piezo-optomechanical microwave-to-optical quantum convertors

We extend the table from the review paper [34] as Table 4.1 with our work on the OMR included. We also introduced a unit length coupling strength G_0 which arise from the traveling wave coupling in the OMR system.

4.5 Summary

In conclusion, we have demonstrated the first OMR in which photonic and phononic modes are co-resonantly coupled to achieve efficient optomechanical mode conversion. The integration of the OMR in an OMIC allows exploration and validation of the time-reversal symmetry and optical reciprocity of the system. The OMR is a new type of traveling wave cavity optomechanics, which has unique advantages over the standing-wave type, including multimode coupling, readiness for interconnecting multiple devices, and flexibility in device design. The critical next step is to improve the photonic and phononic resonance quality factors, which can be achieved with fabrication process optimization and new material platforms. It is also necessary to develop an unsuspended design where waveguiding material and the substrate have both high refractive index contrast and large acoustic velocity differences. The hybrid design of the OMIC is applicable to the integration of many piezoelectric and non-piezoelectric materials, such as aluminum nitride and silicon, which are CMOS-compatible. The OMR is compelling for classical applications such as high-efficiency acousto-optic frequency shifters, frequency beam splitters, and on-chip optical isolators. For quantum applications, achieving phase-matching and co-resonating in the OMR will lead to ultra-efficient microwave-to-optical signal transduction for superconducting qubits. Furthermore, the hybrid OMIC can be also integrated with many other types of solid-state qubits [**?**] to use phonons as quantum information carriers.

4.6 Device fabrication

The as-grown boron-doped GaP (266 nm)-on-Si substrate is purchased from NAsPIII/V GmbH. The GaP photonic and phononic waveguides are patterned with electron beam lithography (EBL) (JEOL-JBX6300FS) using PMMA 950K A6 resist. The pattern is transferred into GaP by partial etching in an inductively coupled plasma etcher using chlorine-based chemistry. The 290 nm thick ZnO film is deposited using an RF magnetron sputtering system and lift-off in a sonicated acetone bath. The IDT pattern is written using the EBL and lift-off after depositing 220 nm aluminum film using an E-beam evaporator. The releasing vias are patterned by the photolithography and etched in ICP. Finally, XeF2 etching of silicon is used for suspending the GaP layer. See Supplementary Note 6 and Fig. S7 for fabrication process flow.

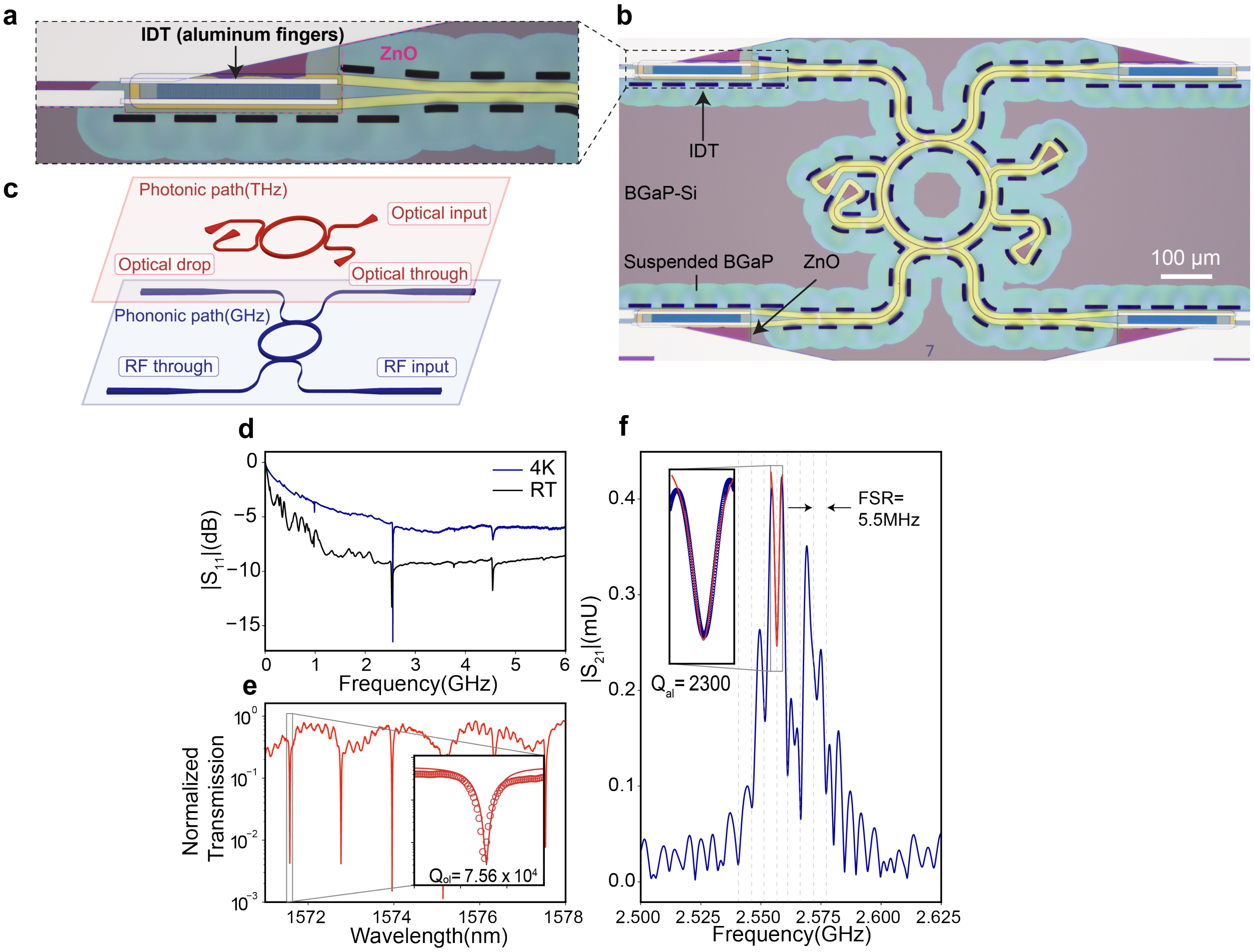

Figure 4.2: Optomechanical ring resonator (OMR) photonic and phononic properties characterization [2]. **(a)** A photon of the aluminum interdigital transducer (IDT) is fabricated on top of a ZnO layer (inside pink dashed line). **(b)** A photo of the OMR device. The purple area is the BGaP-on-Si. The ZnO is under the aluminum metal fingers at the 4 corners of the image. The cyan area is the suspended BGaP film. The light green area is the partially etched BGaP film around the rib waveguide. The ring in the middle is the OMR. **(c)** Pictorial description of the photonic path (upper layer) and the phononic path (lower layer) in the OMR. **(d)** The radio-frequency (RF) reflection spectrum (S_{11}) of the OMR at room-temperature (RT) and 4 K. **(e)** The optical transmission spectrum of the OMR photonic path. The optical loaded quality factor $Q_{ol} = 7.56 \times 10^4$. **(f)** The RF transmission spectrum (S_{21}) of the OMR at RT and 4 K. The acoustic loaded quality factor $Q_{al} = 2300$.

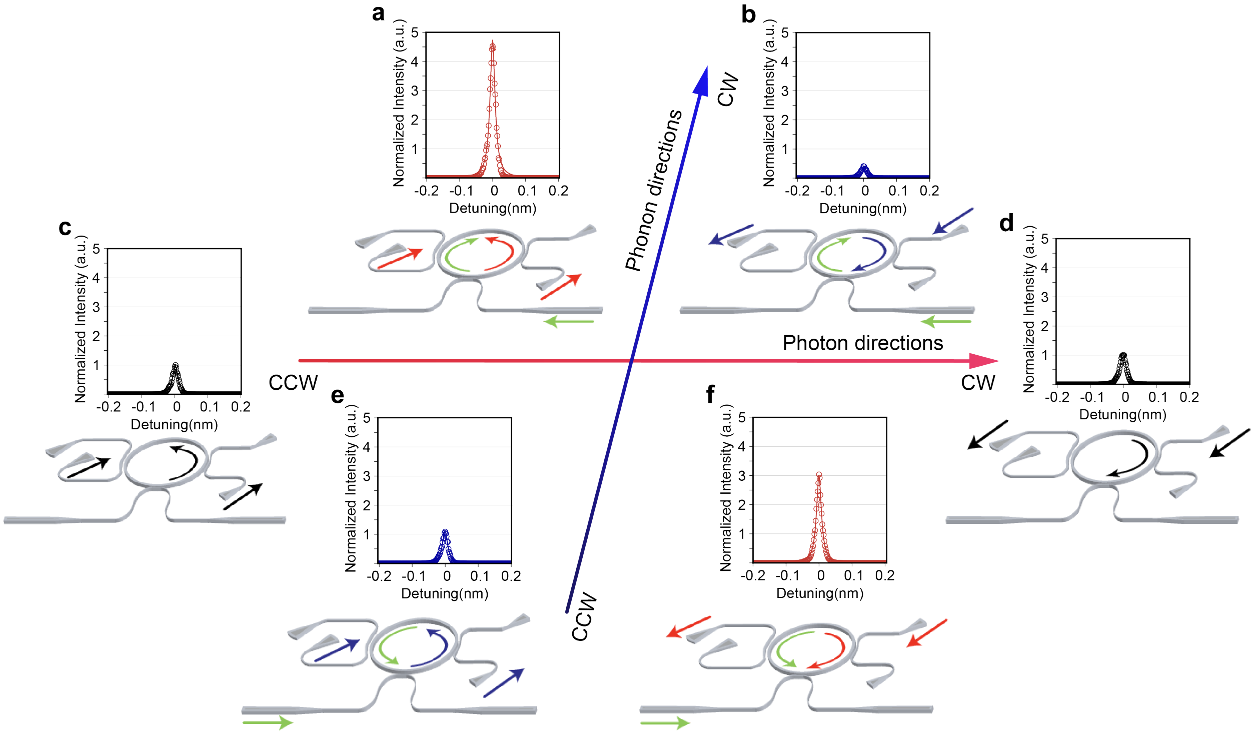

Figure 4.3: Time-reversal symmetry breaking of the photonic modes in the OMR [2]. (a, f) The TE_2 output spectrum that satisfies the phase-matching condition (PMC) when the photon and phonon are counter-propagating. **(b, e)** The TE_2 output spectrum that does not satisfy the PMC when the photon and phonon are co-propagating. **(c, d)** The TE_2 output spectrum when the phononic inputs are off.

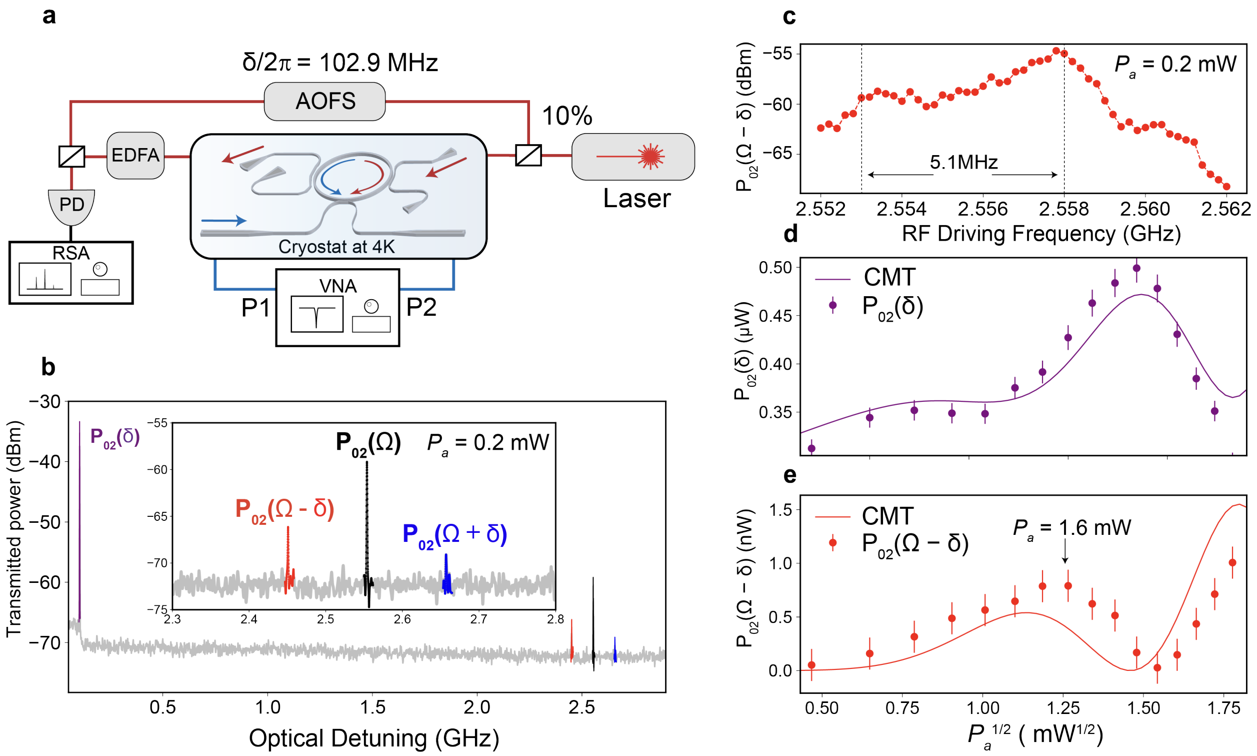

Figure 4.4: Microwave-to-optical frequency conversion using co-resonating modes [2]. **(a)** The measurement setup of the microwave-optical conversion experiment. **(b)** The output optical spectrum of the mixed signal between the reference signal and the output optical signal. **(c)** The $P_{02}(\Omega - \delta)$ signal intensity as a function of radio-frequency (RF) detuning. **(d)** The RF power dependent $P_{02}(\delta)$ signal intensity. **(e)** The RF power dependent $P_{02}(\Omega - \delta)$ signal intensity.

Chapter 5

Microwave-optical frequency transduction using silicon-on-sapphire optomechanical ring resonator

We demonstrate a silicon-on-sapphire (SOS) platform for a microwave-optical frequency transducer on an optomechanical ring resonator (OMR) with an integrated piezoelectric zinc-oxide (ZnO) layer to facilitate electromechanical conversions. By harnessing the triple traveling mode co-resonances in the OMR, we report a phonon pump-enhanced coupling rate $G_b = 3.6\ \mathrm{GHz/mW^{-1/2}}$ and a saturation power $P_{\mathrm{sat}} = 3.6$ mW. The SOS platform is also compatible with various superconducting-based qubit architectures, which provides an approach for monolithic integration between optical and microwave components.

This chapter has been published as:

I-Tung Chen, Nicholas S. Yama, Haoqin Deng, Qixuan Lin, Yue Yu, Abhi Saxena, Arka Majumdar, Kai-Mei C. Fu, and Mo Li. In review (2025).

5.1 A Hamiltonian perspective of optomechanical ring resonator

In the previous section, we describe the acoustic and optical mode coupling using the coupled mode theory approximate to a straight waveguide. In contrast, ideally, a quantum mechanical description can predict the coupling of resonant modes inside a cavity. Furthermore, by understand the system Hamiltonian and the time evolution of the system we would be able to estimate the optomechanical coupling rate, which can be used to compare our system to other cavity-optomechanical systems.

5.1.1 Three-modes propagation in an optomechanical waveguide

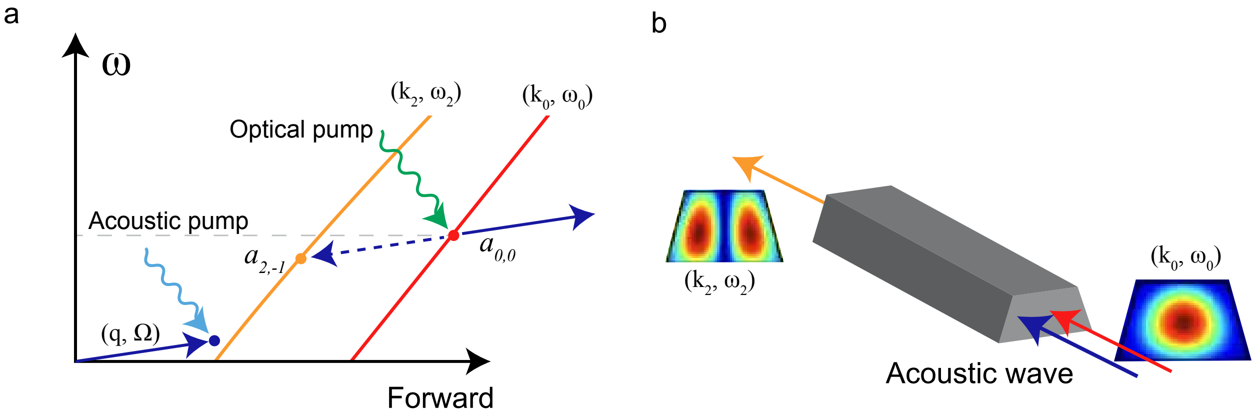

Figure 5.1: A straight optomechanical waveguide. a. A dispersion curve of the optomechanical waveguide with co-propagated modes. **b.** An illustration of the optomechanical waveguide with the cross-sectional optical mode profiles.

To better understand out system, we can model the intermodal scattering of a straight waveguide as a three mode coupling system. The Hamiltonian of such system can be expressed as

$$\begin{aligned} H =& H_0 + H_I \\ =& \sum_{i=0,2} \hbar\omega_i \hat{a_i}^\dagger \hat{a_i} + \hbar\Omega\hat{b}^\dagger\hat{b} + \sum_{i,j=0,2} \hbar g_{ij} \hat{a_i}^\dagger \hat{a_j}(\hat{b} + \hat{b}^\dagger), \end{aligned} \tag{5.1}$$

where $\hat{a}_i$ ($\hat{a}_i^\dagger$) and $\hat{b}$ ($\hat{b}^\dagger$) are the annihilation (creation) operator of the i-th photonic and phononic mode with frequency ω_i and Ω. The interaction Hamiltonian H_I includes the self-coupling and cross-coupling interactions. The self-coupling interaction ($i = j$) can be written as

$$H_{I(\text{self})} = \sum_{i=j=0,2} \hbar g_{ii} \hat{a_i}^\dagger \hat{a_i} (\hat{b} + \hat{b}^\dagger). \tag{5.2}$$

The self-coupling coefficient g_{ii} is the optomechanical coupling of an optical cavity with a mechanically moving mirror [30]. The cross-coupling interaction ($i \neq j$) describes the multi-modal interaction, which, in this case, two optical modes couple to a mechanical mode. This can be expressed as

$$H_{I(\text{crx})} = (\hbar g_{02} \hat{a_0}^\dagger \hat{a_2} + \hbar g_{20} \hat{a_2}^\dagger \hat{a_0})(\hat{b} + \hat{b}^\dagger). \tag{5.3}$$

The cross-coupling coefficient g_{ij} is the intermodal coupling between two optical modes facilitated by a mechanical mode. We will discuss g_{ij} in later section. So far, the expressions of the multi-modal optomechanical coupling are agnostic. This is similar to the two mode system that we modeled in the Chapter 2, but, now we have *two* optical modes instead of one.

We now consider traveling optical and mechanical modes in a straight optomechanical waveguide (Fig. 5.1). The translation symmetry of the optomechanical waveguide ensures the bosonic operators to be expressed as traveling modes using Bloch-Floquet expansion [73, 74].

$$\hat{a}_i(z,t) = \hat{a}_i e^{-i(k_i z - \omega_i t)} \tag{5.4}$$

$$\hat{b}(z,t) = \hat{b} e^{-i(qz - \Omega t)}, \tag{5.5}$$

where k_i and q are the wavevector of the i-th photonic and phononic modes that are traveling in z direction. Using equation (A.19b) and (A.19c), now (5.3) becomes

$$\begin{aligned} H_{I(\text{crx})} = &\hbar g (\hat{a}_0^\dagger \hat{a}_2 \hat{b} e^{-i(\Omega-\Delta)t + i(q-\delta)z} \\ &+ \hat{a}_0^\dagger \hat{a}_2 \hat{b}^\dagger e^{i(\Omega+\Delta)t + i(-q-\delta)z} \\ &+ \hat{a}_2^\dagger \hat{a}_0 \hat{b} e^{-i(\Omega+\Delta)t + i(q+\delta)z} \\ &+ \hat{a}_2^\dagger \hat{a}_0 \hat{b}^\dagger e^{i(\Omega-\Delta)t + i(-q+\delta)z}), \end{aligned} \tag{5.6}$$

where $\Delta = \omega_0 - \omega_2$, $\delta = k_0 - k_2$, and we assume $g = g_{20} = g_{02}$. This is essentially the well-known intermodal Brillouin scattering process [27, 23, 17], where two optical modes (ω_0, k_0) and (ω_2, k_2) exchange energy via an acoustic mode (Ω, q) when the phase-matching condition is satisfied.

Forward scattering process

In the forward scattering process, we consider the process of which the phase-matching condition satisfies $k_0 - k_2 + q = 0$. In this case, the non-phase-matching terms are suppressed, we can then simplify Eq. A.22b, A.22c. Meaning that the anti-Stokes scattering is the dominate process in the forward direction, if we pump at optical mode 2. We can expand the equations of motion through Fourier decomposition of the sidebands induced by the optomechanical coupling:

$$\hat{a}_0(t) = \sum_{n=-\infty}^{\infty} a_{0,n} e^{-i(n\Omega+\omega_{in})t} = a_{0,-1} e^{-i(\omega_{in}-\Omega)t} + a_{0,0} e^{-i\omega_{in}t} + a_{0,+1} e^{-i(\omega_{in}+\Omega)t}, \tag{5.7}$$

$$\hat{a}_2(t) = \sum_{n=-\infty}^{\infty} a_{2,n} e^{-i(n\Omega+\omega_{in})t} = a_{2,-1} e^{-i(\omega_{in}-\Omega)t} + a_{2,0} e^{-i\omega_{in}t} + a_{2,+1} e^{-i(\omega_{in}+\Omega)t}. \tag{5.8}$$

We then substitute the Fourier decomposition into Eq. A.22b, A.22c and solve for the intracavity amplitude of each mode.

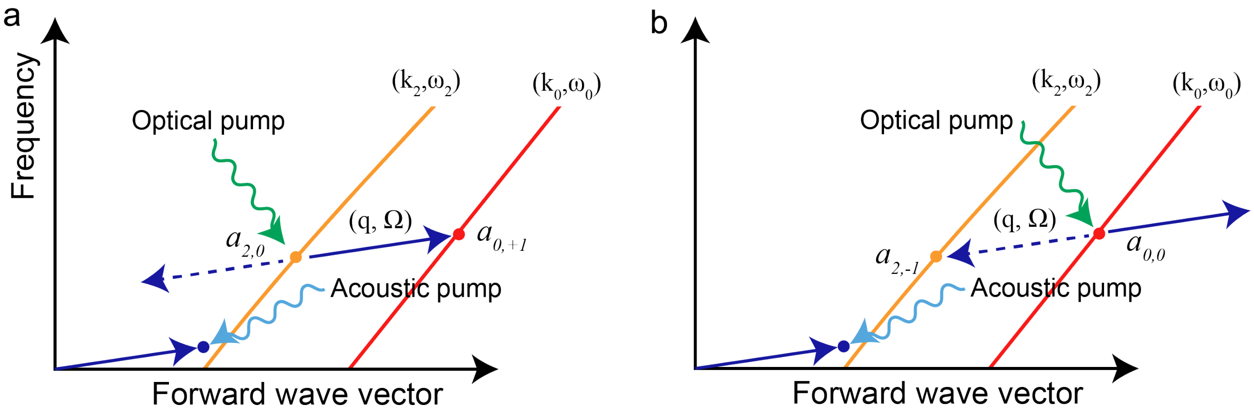

Figure 5.2: Forward scattering process. **(a)** The $a_{2,0}$ mode absorbing a phonon, resulted in a forward anti-Stokes mode $a_{0,+1}$. **(b)** The $a_{0,0}$ mode emitting a phonon, resulted in a forward Stokes mode $a_{2,-1}$.

$$a_{0,-1} = \frac{-igb\sqrt{\kappa_{ex2}}}{(\frac{\kappa_0}{2} - i(\Delta_0 - \Omega))(\frac{\kappa_2}{2} - i\Delta_2) + |g|^2|b|^2} a_{in}, \quad a_{2,-1} = \frac{-ig^*b^*\sqrt{\kappa_{ex0}}}{(\frac{\kappa_0}{2} - i\Delta_0)(\frac{\kappa_2}{2} - i(\Delta_2 - \Omega)) + |g|^2|b|^2} a_{in}, \tag{5.9}$$

$$a_{0,0} = \frac{(\frac{\kappa_2}{2} - i(\Delta_2 + \Omega))\sqrt{\kappa_{ex0}}}{(\frac{\kappa_0}{2} - i\Delta_0)(\frac{\kappa_2}{2} - i(\Delta_2 + \Omega)) + |g|^2|b|^2} a_{in}, \quad a_{2,0} = \frac{(\frac{\kappa_0}{2} - i(\Delta_0 - \Omega))\sqrt{\kappa_{ex2}}}{(\frac{\kappa_0}{2} - i(\Delta_0 - \Omega))(\frac{\kappa_2}{2} - i\Delta_2) + |g|^2|b|^2} a_{in}, \tag{5.10}$$

$$a_{0,+1} = \frac{-igb\sqrt{\kappa_{ex2}}}{(\frac{\kappa_0}{2} - i(\Delta_0 + \Omega))(\frac{\kappa_2}{2} - i\Delta_2) + |g|^2|b|^2} a_{in}, \quad a_{2,+1} = \frac{-igb\sqrt{\kappa_{ex0}}}{(\frac{\kappa_0}{2} - i\Delta_0)(\frac{\kappa_2}{2} - i(\Delta_2 + \Omega)) + |g|^2|b|^2} a_{in}, \tag{5.11}$$

where $a_{(0,2),(-1,+1)}$ denote the i-th mode's Stokes and anti-Stokes scattering process, and $a_{(0,2),0}$ denotes the carrier mode of the i-th mode. $\Delta_0(2)$ is the detuning of the optical cavity resonance 0(2) from the pump laser. We can express the forward scattering process using Eq. 5.9, 5.10 and 5.11. In the common system of a 1D optomechanical beams, the OM coupling rate g is at the range of kHz, which is much smaller than the optical loss rate $\kappa_{0(2)}$ at GHz range. Note that an optical cavity with linewidth 0.05 nm at 1550 nm ($Q_i = 62,000$), corresponds to a linewidth of 6 GHz. Therefore, we can assume $|g||b| << \sqrt{\kappa_1\kappa_2}/2$ at a small acoustic pump region. In this case, we can simply the equations to:

$$a_{0,0} = \frac{\sqrt{\kappa_{ex0}}}{(\frac{\kappa_0}{2} - i\Delta_0)} a_{in}, \tag{5.12}$$

$$a_{2,0} = \frac{\sqrt{\kappa_{ex2}}}{(\frac{\kappa_2}{2} - i\Delta_2)} a_{in}, \tag{5.13}$$

$$a_{0,+1} = \frac{-igb\sqrt{\kappa_{ex2}}}{(\frac{\kappa_0}{2} - i(\Delta_0 + \Omega))(\frac{\kappa_2}{2} - i\Delta_2)} a_{in}, \tag{5.14}$$

$$a_{2,-1} = \frac{-ig^*b^*\sqrt{\kappa_{ex0}}}{(\frac{\kappa_0}{2} - i\Delta_0)(\frac{\kappa_2}{2} - i(\Delta_2 - \Omega))} a_{in}. \tag{5.15}$$

In the forward direction, $a_{0,-1}$ and $a_{2,+1}$ are suppressed due to the phase mismatch of the modes. The output spectrum can then be obtained by using the input-output relation. The output spectrum S_{out} consist of the carrier $S_{out,0}$, Stokes $S_{out,+1}$ and anti-Stokes $S_{out,-1}$ modes:

$$S_{out} = S_{out,0} + S_{out,+1} + S_{out,-1}, \tag{5.16}$$

where

$$S_{out,0} = S_{in} - \sqrt{\kappa_{ex0}} a_{0,0} - \sqrt{\kappa_{ex2}} a_{2,0}, \tag{5.17}$$

$$S_{out,+1} = -\sqrt{\kappa_{ex2}} a_{0,+1}, \tag{5.18}$$

$$S_{out,-1} = -\sqrt{\kappa_{ex0}} a_{2,-1}. \tag{5.19}$$

The forward scattering spectrum is shown in Fig. 5.3.

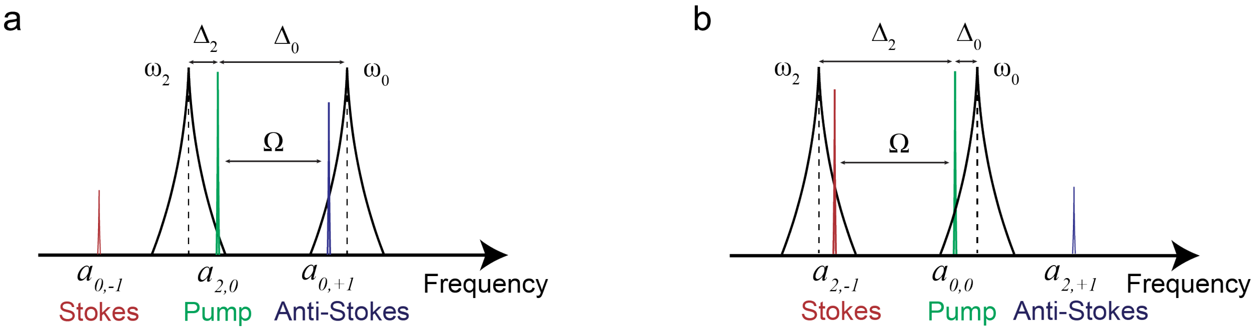

Figure 5.3: Output spectrum of the forward scattering process. $\Delta_{0(2)}$ is the detuning of the optical mode 0(2) from the pump laser. Ω is the acoustic mode frequency. **(a)** The $a_{2,0}$ mode is forward anti-Stokes scattered to $a_{0,+1}$ mode and the Stokes scattering is suppressed because of the phase mismatch. **(b)** The $a_{0,0}$ forward Stokes scattered to $a_{2,-1}$ mode and the Anti-Stokes scattering is suppressed because of the phase mismatch.

Backward scattering process

Similar to the forward scattering process, we can also use equation 5.9, 5.10 and 5.11 to describe the backward scattering process. Now we only consider the phase-matching condition of $k_0 - k_2 + q = 0$. As shown in Fig. 5.4. We can again go through the equations of motion and solve for the intracavity amplitude of each mode. However, this time, we set the g_f to zero, and we can express the

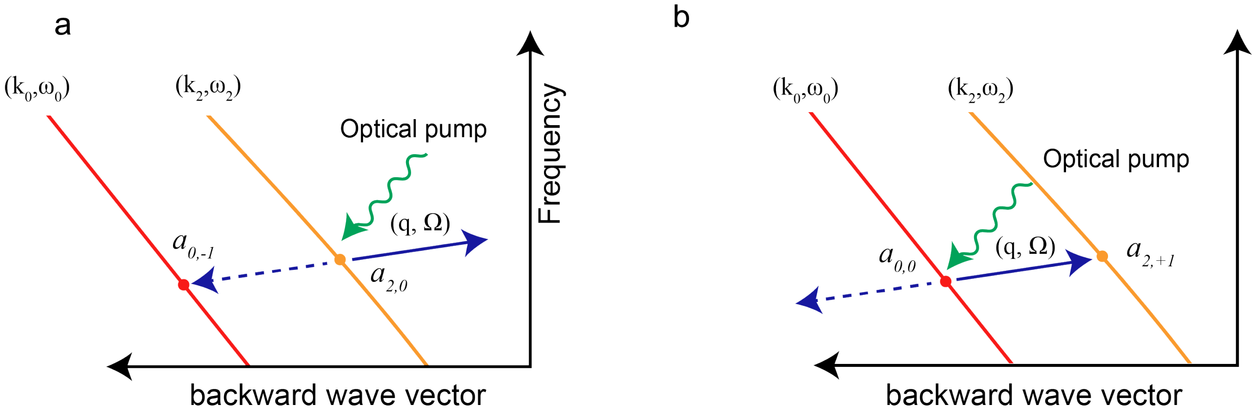

Figure 5.4: Backward scattering process. (a) The $a_{2,0}$ mode emits a phonon, resulted in a backward Stokes mode $a_{0,-1}$. **(b)** The $a_{0,0}$ mode absorbs a phonon, resulted in a backward anti-Stokes mode $a_{2,+1}$.

amplitudes as (in a small acoustic pump region, i.e. $|g||b| << \sqrt{\kappa_1\kappa_2}/2$):

$$a_{0,0} = \frac{\sqrt{\kappa_{ex0}}}{(\frac{\kappa_0}{2} - i\Delta_0)} a_{in}, \tag{5.20}$$

$$a_{2,0} = \frac{\sqrt{\kappa_{ex2}}}{(\frac{\kappa_2}{2} - i\Delta_2)} a_{in}, \tag{5.21}$$

$$a_{0,-1} = \frac{-igb\sqrt{\kappa_{ex2}}}{(\frac{\kappa_0}{2} - i(\Delta_0 - \Omega))(\frac{\kappa_2}{2} - i\Delta_2)} a_{in}, \tag{5.22}$$

$$a_{2,+1} = \frac{-ig^*b^*\sqrt{\kappa_{ex0}}}{(\frac{\kappa_0}{2} - i\Delta_0)(\frac{\kappa_2}{2} - i(\Delta_2 + \Omega))} a_{in}. \tag{5.23}$$

Consequently, the output spectrum S_{out} can be shown as:

$$S_{out} = S_{out,0} + S_{out,+1} + S_{out,-1}, \tag{5.24}$$

where

$$S_{out,0} = S_{in} - \sqrt{\kappa_{ex0}}a_{0,0} - \sqrt{\kappa_{ex2}}a_{2,0}, \tag{5.25}$$

$$S_{out,+1} = -\sqrt{\kappa_{ex2}}a_{2,+1}, \tag{5.26}$$

$$S_{out,-1} = -\sqrt{\kappa_{ex0}}a_{0,-1}. \tag{5.27}$$

The backward scattering spectrum is shown in Fig. 5.5. Now that we have established the output spectrum, we will analyze the power dependence of the intermodal scattering process.

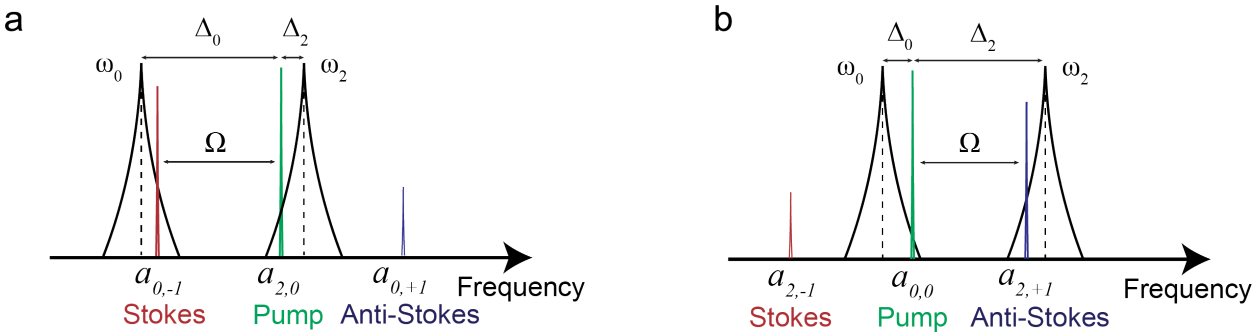

Figure 5.5: Output spectrum of the forward scattering process. $\Delta_{0(2)}$ is the detuning of the optical mode 0(2) from the pump laser. Ω is the acoustic mode frequency. **(a)** The $a_{2,0}$ mode is forward anti-Stokes scattered to $a_{2,+1}$ mode and the Stokes scattering is suppressed because of the phase mismatch. **(b)** The $a_{0,0}$ forward Stokes scattered to $a_{0,-1}$ mode and the Anti-Stokes scattering is suppressed because of the phase mismatch.

5.1.2 Triple resonance in a ring type cavity

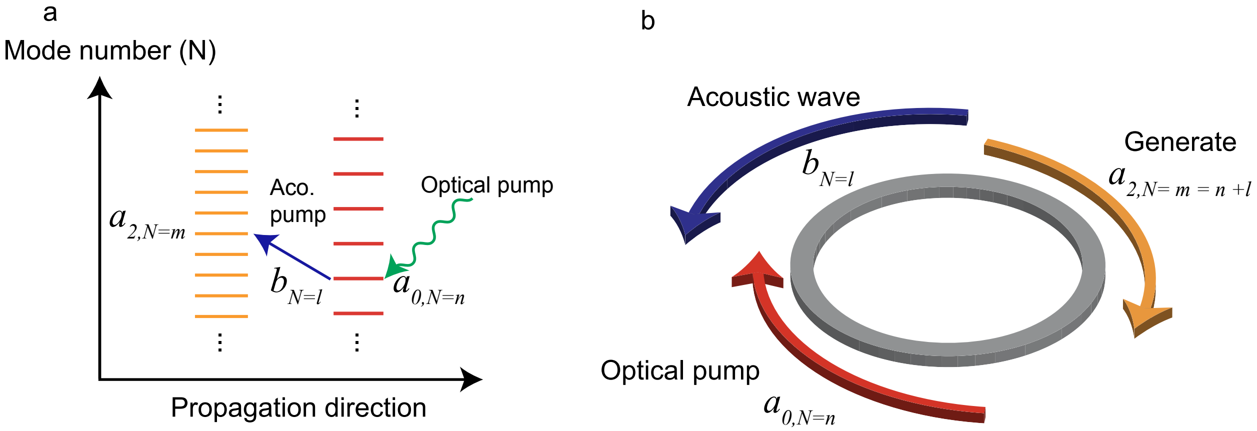

Figure 5.6: An optomechanical ring resonator. a. An optical energy level with different azimuthal mode number. **b.** An illustration of the optomechanical ring with optical and acoustic mode propagation direction that satisfied the phase-matching condition.

A ring cavity is simply a waveguide with one edge wrap around and connect the other end. A similar treatment can be applied for such multimodal ring cavity, by moving to cylindrical coordinate and applied a periodic boundary condition, we now choose

$$\hat{a}_i(t, r, \phi) = \hat{a}_i(r)e^{-i(m_i\phi - \omega_i t)} \tag{5.28}$$

$$\hat{b}(t, r, \phi) = \hat{b}(r)e^{-i(l\phi - \Omega t)}, \tag{5.29}$$

where m_i (l) is the azimuthal mode number of the i-th optical (acoustic) mode, and the r, z, ϕ corresponds to the cylindrical coordinate system in a ring-type itinerant wave cavity. The azimuthal mode numbers are integers ($m_i(l) \in \mathbf{N}$), and the positive or negative sign describes the propagating directions of the modes (i.e., clockwise (CW) or counter-clockwise (CCW)). Consequentially, a similar form of $H_{I(crx)}$ can be derived as

$$\begin{aligned} H_{I(\mathrm{crx})} =& \hbar g(\hat{a}_0^\dagger \hat{a}_2 \hat{b} e^{-i(\Omega-\Delta)t + i(l-\delta_m)\phi} \\ & + \hat{a}_0^\dagger \hat{a}_2 \hat{b}^\dagger e^{i(\Omega+\Delta)t + i(-l-\delta_m)\phi} \\ & + \hat{a}_2^\dagger \hat{a}_0 \hat{b} e^{-i(\Omega+\Delta)t + i(l+\delta_m)\phi} \\ & + \hat{a}_2^\dagger \hat{a}_0 \hat{b}^\dagger e^{i(\Omega-\Delta)t + i(-l+\delta_m)\phi}). \end{aligned} \tag{5.30}$$

The triple resonance condition (two optical and one mechanical) is satisfied when $\delta_m = \pm l$, which ± sign dictates the CW or CCW traveling direction (Fig. 5.6). We will leverage these properties to construct quantum state swapping and two-mode squeezing Hamiltonians in the following section.

5.1.3 Beam-splitter and two-mode squeezing Hamiltonian

One can leverage the phase-matching condition of the circuit optomechanics to realize microwave-to-optical quantum transduction and entanglement generation. In contrast to the two mode interaction that is introduced in Chapter 2, a three mode interaction can also provide a similar property to realize beam-splitter and two-mode squeezing Hamiltonians. This is, when the optical wavevector differences of the two optical modes $\Delta = \pm\Omega$ and $\delta = \pm q$, equation (5.30) becomes two different interactions.

(1) Quantum state transduction between microwave phonon and optical photon. Consider

$\Delta = +\Omega$, $\delta = +q$, and discarding fast rotating terms, equation (5.30) becomes

$$H_{I(\mathrm{crx})} = \hbar g(\hat{a}_0^\dagger \hat{a}_2 \hat{b} + \hat{a}_2^\dagger \hat{a}_0 \hat{b}^\dagger). \tag{5.31}$$

One can further treat optical mode as a classical pump ($\hat{a}_2 \to \langle \alpha_2 \rangle$) and equation (5.31) arrives at

$$H_{I(\mathrm{red})} = \hbar G_2(\hat{a}_0^\dagger \hat{b} + \hat{a}_0 \hat{b}^\dagger), \tag{5.32}$$

where the pump enhanced coupling coefficient $G_2 = g|\langle \alpha_2 \rangle|$. This is the beam-splitter Hamiltonian for photon-phonon quantum state transduction. This is identical to the beam-splitter interaction in Chapter 2.

(2) Photon-phonon entanglement generation and two-mode squeezing. Similarly, we now choose the same optical detuning $\Delta = +\Omega$, but $\delta = -q$, and linearize $\hat{a}_1 \to \langle \alpha_1 \rangle$ in the rotating frame. The Hamiltonian becomes

$$H_{I(\mathrm{blue})} = \hbar G_0(\hat{a}_2^\dagger \hat{b}^\dagger + \hat{a}_2 \hat{b}), \tag{5.33}$$

where $G_0 = g|\langle \alpha_0 \rangle|$. This is the Hamiltonian representing two-mode squeezing. Equation (5.32)-(5.33) are identical to red and blue detuning in cavity optomechanics. Since our model is a multimodal coupling scheme, both of the optical mode and the acoustic mode travel through the waveguide simultaneously, which maximize the interaction length.

To summarize, by choosing the pump $\Delta = +\Omega$ and $\delta_m = \pm l$ in a ring cavity, one can achieve equation (5.32) or (5.33). Note that in the ring cavity, the driving optical field is resonantly pumped on its respective cavity mode, which is different from the sideband pumping in cavity optomechanics. In this system, we select the pump direction ($\pm l$) instead of the detuning to achieve the beam-splitter and two-mode squeezing Hamiltonian.

5.2 Silicon-on-sapphire platform

With the theory developed for the optomechanical ring, we start to look at possible material platforms that are suitable for the realization of an optomechanical integrated circuit (OMIC).

An OMIC needs both good optical and acoustic index contrast between the slab material and the

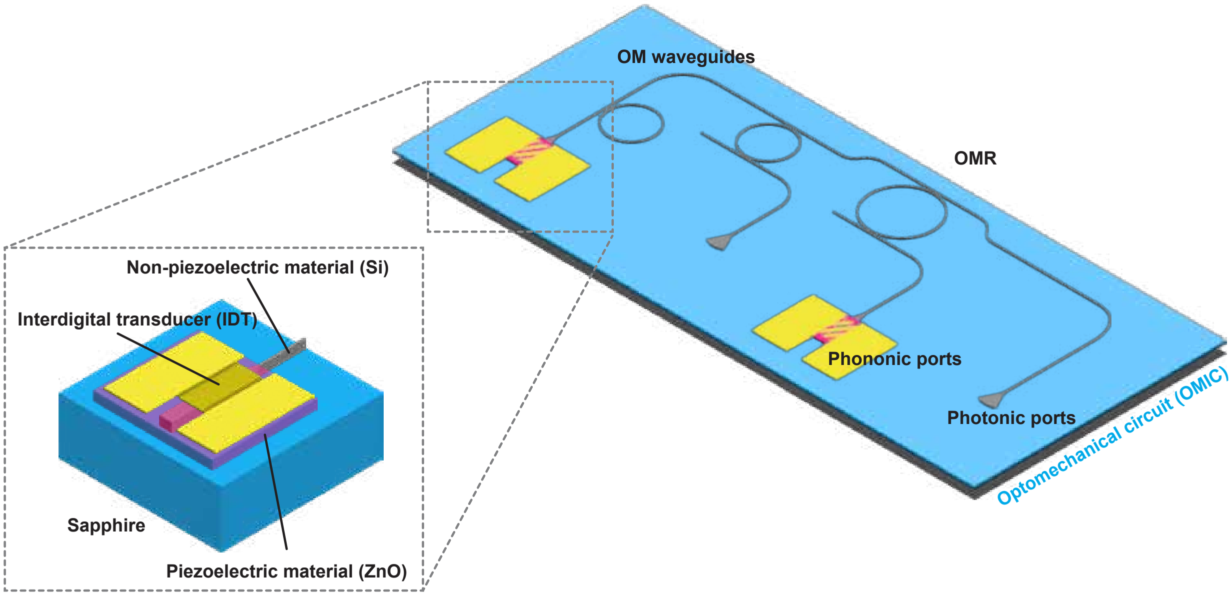

Figure 5.7: An illustration of optomechanical integrated circuit (OMIC) The OMIC consists of two different components, a phononic part and a photonic part. Both of which are monolithically integrated on the same substrate.

substrate material to be able to guide photonic and phononic mode simultaneously. For example, the waveguiding material would require a higher optical refractive index comparing to the substrate to be able to guide optical modes. And the acoustic velocity of the waveguiding material needs to be slower than that of the substrate (Fig. 5.7). Although one can suspend the waveguiding material but the structural integrity and the compatibility of such device would be compromise. Therefore, we targeted a silicon-on-sapphire (SOS) material platform.

Silicon provides a high acousto-optic figure-of-merit $\mathcal{M}_2 = 36.1$ ($\times 10^{-15}$ s^{3}kg^{-1}) [5, 6, 7], especially when compared to the sapphire substrate with its lower refractive index ($n_{\text{sapphire}} = 1.72$) [75], makes it an ideal material platform for optomechanical circuits. The acoustic velocity contrast between silicon ($v_{\text{si}} \sim 5000\ m/s$, surface acoustic wave) [76, 77] and sapphire ($v_{\text{sapphire}} \sim 10,600\ m/s$, longitudinal wave) [78] also enables acoustic waveguiding in the silicon layer without the need for freestanding structures. The SOS platform presented is also compatible with various superconducting-based qubit architectures [79, 80, 81, 82, 83, 84], which can be integrated easily without suspended nanostructures.

5.3 SOS-OMR device design

We start by considering a simple optomechanical resonator (OMR) design on the SOS platform. The OMR consists of a silicon ring resonator that supports both optical and mechanical modes. The optical mode is confined within the silicon ring due to the high refractive index contrast between silicon and sapphire. The mechanical mode, on the other hand, is confined within the ring due to the acoustic velocity contrast between silicon and sapphire.

The design parameters of the OMR, such as the ring radius, waveguide width, and gap between the ring and the bus waveguide, are optimized to achieve strong optomechanical coupling. The optical mode in the ring resonator interacts with the mechanical mode through radiation pressure and photoelastic effects, leading to the modulation of the optical resonance frequency by the mechanical vibrations. We design the OMR to have two main functionalities: 1. a microwave-to-optical transduction mode (Fig. 5.8 left panel), where microwave signal is being converted to a mechanical mode and converted to an optical mode. 2. an entanglement generation mode where an optical input is down-converted to a mechanical and a second optical mode (Fig. 5.8 right panel).

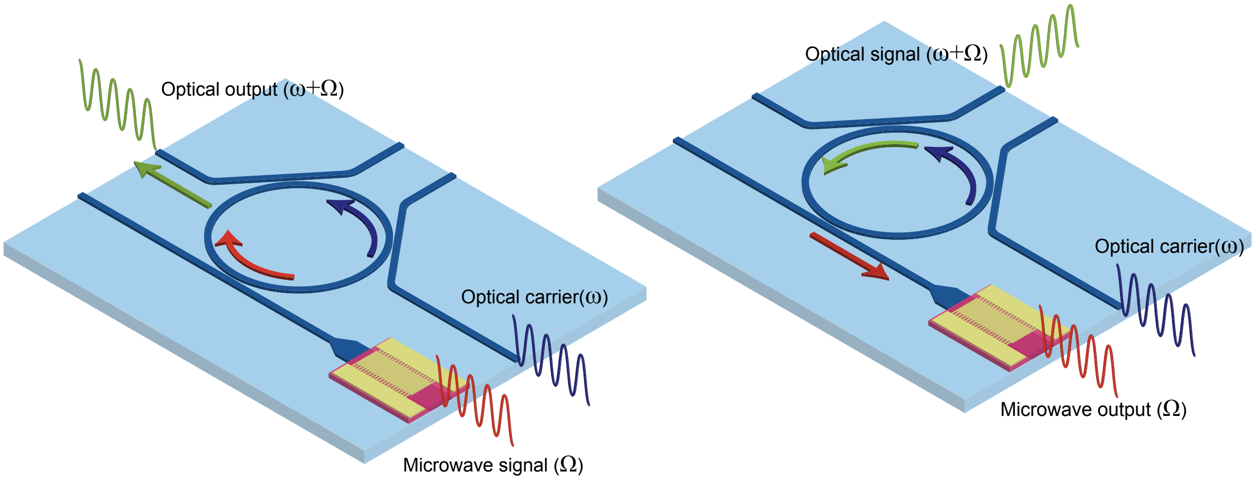

Figure 5.8: Design of a silicon-on-sapphire optomechanical resonator (OMR) The OMR consists of a silicon ring resonator that supports both optical and mechanical modes. The design parameters are optimized to achieve strong optomechanical coupling.

We first perform optical dispersion simulations to better understand the design parameters of the waveguides. A simulated waveguide dispersion is shown in Fig. 5.9. Since this is a ring resonator, multiple azimuthal modes can be seen on the dispersion curve. Contrasting standing wave resonators, the OMR supports optical modes (ω_0, β_0) and (ω_1, β_1) which exchange energy via a co-resonant acoustic mode (Ω, q) when the phase matching conditions $\beta_0 + q = \beta_1$ and $\omega_0 \pm \Omega = \omega_1$ are satisfied. The multi-resonant phase-matched interaction enables efficient bidirectional microwave-to-optical and optical-to-optical conversion. Under a suitable coherent drive, the interaction manifests in the form of inter-modal Brillouin scattering for microwave-to-optical and optical-to-optical conversion or a stimulated Brillouin emission process for optical-to-microwave conversion. Figure 5.9a-5.9b show the simulated photonic and phononic modes dispersion curve of the OMR, as well as the resonant frequencies at which the microwave-optical conversion process is enhanced by satisfying both the frequency and phase differences. The acoustic dispersion of the OMR can also be simulated, and we can see that the acoustic waves have a MHz level FSR (Fig. 5.10).

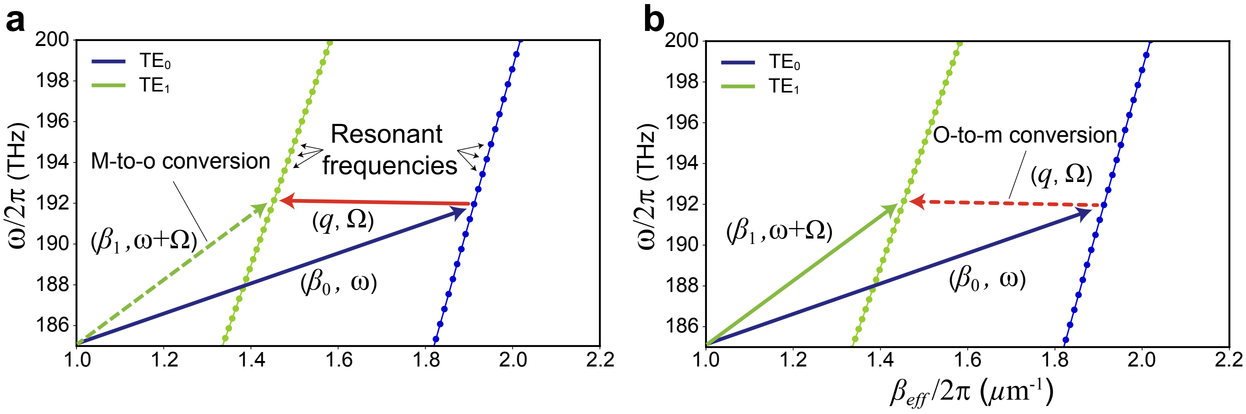

Figure 5.9: Simulated optical dispersion of the OMR a, b. Schematic illustrations of OMR using the zinc oxide (ZnO)-SOS material platform. **a.** show a microwave signal being converted to optical output via Brillouin Scattering. **b.** shows an optical signal being down-converted as microwave signal output via stimulated Brillouin emission.

The OMR is fabricated using a commercial SOS wafer with a 330 nm silicon layer epitaxially grown on c-plane sapphire substrate. Figure 5.11a shows the cross-section of the OMR waveguide design. The silicon ridge waveguide has a width w = 800 nm, a sidewall angle $\theta = 82°$, and a bending radius r = 50 μm. The refractive index contrast of silicon and sapphire enables a non-suspending device design that supports both TE$_0$ and TE$_1$ modes at 193.4 THz, as shown in Fig.

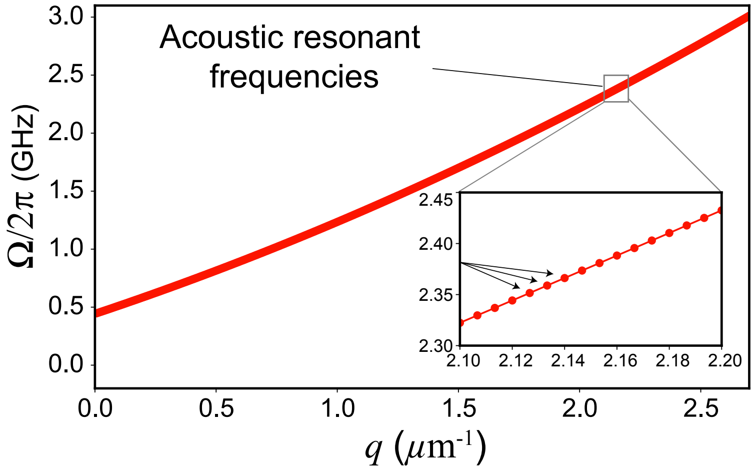

Figure 5.10: Simulated acoustic dispersion of the OMR The acoustic dispersion of the OMR, the solid dots are acoustic resonance frequencies.

5.9a and 5.9b. Similarly, the sound speed difference between silicon and sapphire also facilitates the support of Love modes (L_0) in the silicon waveguide without needing to suspend structure (Fig. 5.11d, 5.11e).

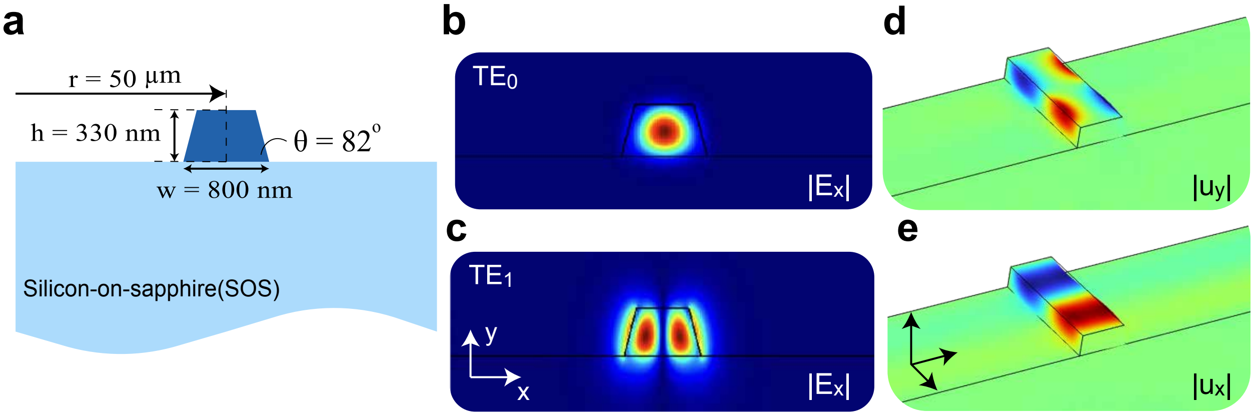

Figure 5.11: Simulated mode profiles a. The cross-section of the OMR waveguide. The silicon waveguide height $h = 330$ nm with a width $w = 800$ nm and bending radius of 50 μm. The sidewall angle from the fabricated waveguide $\theta = 82°$. **b, c.** Simulated waveguide electric field profiles ($|E_x|$) of the supported TE_0 and TE_1 modes. **d, e.** The simulated waveguide displacement field profile ($|u|$) of the supported Love (L_0) mode in y-direction (in **d.**) and x-direction (in **e.**).

5.4 SOS acoustic propagation loss characterization

We characterize the SOS acoustic performance by fabricating acoustic delay lines with two different designs but identical IDT aperture size: a slab design (Fig. 5.12 upper right panel)-the acoustic wave travel through the silicon layer without waveguide-and a waveguide design (Fig. 5.12 middle right panel). The slab design allows us to extract the intrinsic acoustic loss of the SOS platform, while the waveguide design reveals the guided wave loss. By varying the delay line length L and measuring RF transmission intensity I_{s21}, we can extract the acoustic loss constant α using

$$I_{s21} = e^{-\alpha L}.$$

We also estimate the α varying the temperature from 4 K to RT (300 K) to extract the temperature dependent loss constant. We found that waveguide design has a higher acoustic loss (5 ± 0.3 dB/mm) comparing to that of the slab design (0.5 ± 0.35 dB/mm). Furthermore, we suspect this is the result from the acoustic wave scattering at the tapering region and the side wall roughness of the ridge acoustic waveguide. By further lowing the temperature to mK regions, which is the superconducting electronic's typical operating temperature, we extrapolate the intrinsic acoustic loss can achieve less than 0.1 dB/mm.

5.5 Initial device calibration

A fabricated OMR on SOS is shown in Fig. 5.13. The OMR is designed using the dispersion simulated from Fig. 5.9. We choose a corresponding waveguide such that the TE_0 and TE_1 can both propagates in the OMR. The fabricated device (Fig. 5.13a) consists of two main components: optical and radio-frequency (RF) input/output (I/O) ports. In total, five grating couplers (GC) are fabricated, and four of the GCs are functioned as the TE_0 and TE_1 I/O ports. The fifth GC is used to align the optical fiber array (See Supplementary Note 3. for fiber array setup). The photonic circuit consists of two key waveguide designs: a multimode waveguide ($W_0 = 800$ nm) and a single mode waveguide ($W_1 = 450$ nm). The multimode waveguide, which share the same width as the OMR, supports both TE_0 and TE_1 mode. In contrast, the narrower single mode waveguide only

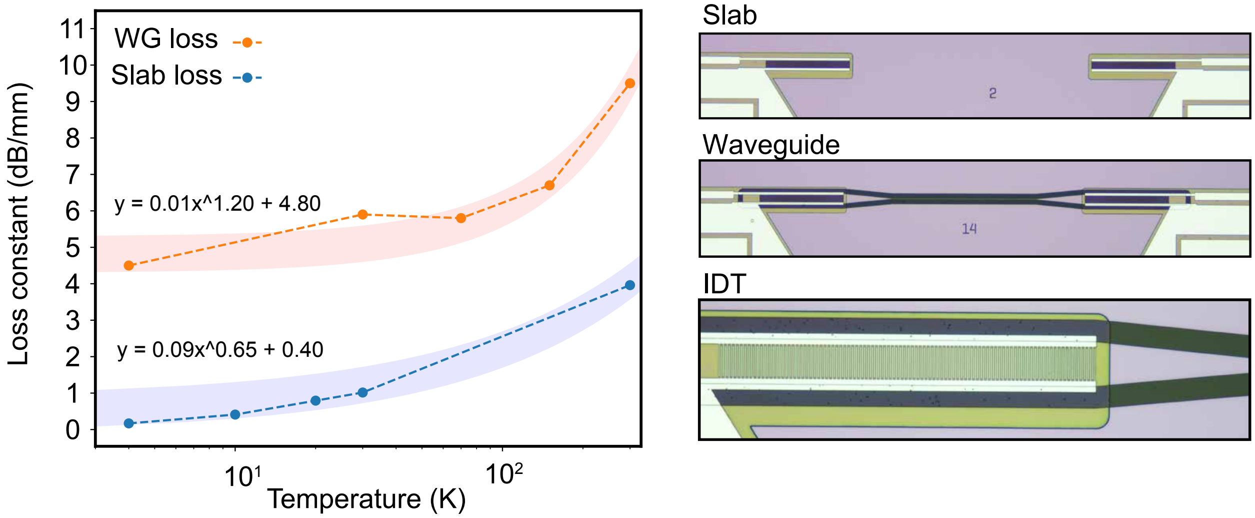

Figure 5.12: Temperature-dependent loss estimation. Left The extracted acoustic loss at various measurement temperature. The shaded area is within the two standard deviations of the fitting error. **Right** Optical image of a slab and a ridge waveguide acoustic delayline design.

guides a fundamental TE mode, whose effective refractive index n_{eff} matches to that of the TE_1 mode in the multimode waveguide. Building on our previous work [2], this design spatially filters the undesired output modes. Both types of waveguides connect to the OMR using a separate add-drop configuration, allowing selective coupling of the TE_0 and TE_1 modes (Fig. 5.13b). A waveguide taper at the drop port's terminus is used to minimize back-reflections of the input laser (See Supplementary Note 4. for full photonic design parameters).

A strongly piezoelectric ZnO film (280 nm) is deposited at each end of the phononic waveguide, and interdigital transducers (IDTs) with a period $\Lambda = 2.85$ μm are fabricated on top of ZnO to generate and detect the acoustic waves (Fig. 5.13c). The phononic waveguides are linearly tapered from the excitation region, transitioning from an initial width of $W_{IDT} = 15$ μm to the OMR waveguide width over a length of 150 μm, thereby preserving the generated L_0 mode.

We first characterize the interdigital transducer (IDT) on the ZnO and the waveguide. We first measure the radio-frequency reflection spectrum of the IDT, as shown in Fig. 5.14. We can see a sharp resonance feature at around 2.21 GHz. This corresponds to the excited acoustic mode. We also see that the IDT resonance intensity increases as we measure the same device at cryogenic temperature. The 3.1 dB increases in S_{11} indicates the IDT becomes more efficient at cryogenic

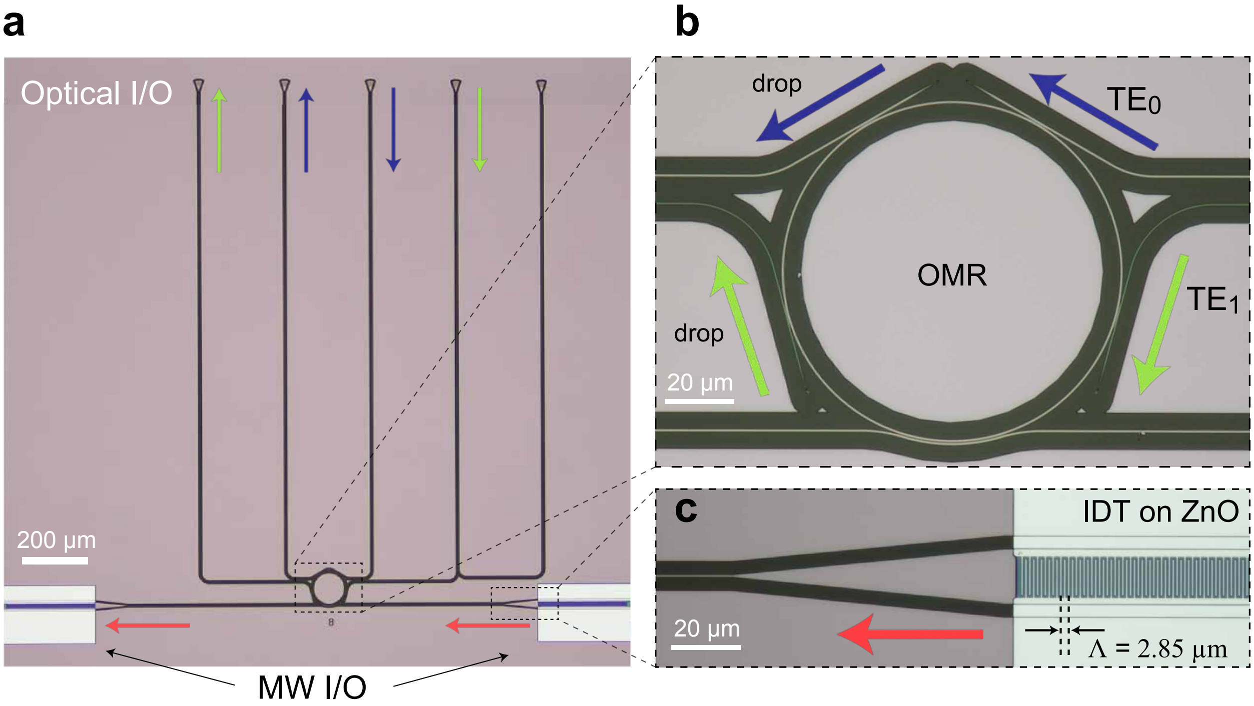

Figure 5.13: OMR on SOS with optical and acoustic input-output ports a. An optical image of the of an OMR on SOS. The TE_0 (TE_1) mode optical signal propagation direction is indicated by the blue (green) arrows. The microwave signal propagation direction is represented by the red arrows. The photonic and phononic mode propagation label here is the configuration used to measure the data in Fig. 5.13 **b.** An enlarged optical image of the OMR. There are two pairs of bus waveguides coupling to the OMR, and they correspond to the TE_0 (blue arrows) and TE_1 mode (green arrows) couplings, respectively. **c.** A zoomed-in optical image of an aluminum IDT on silicon phononic waveguide. The IDT is deposited on ZnO and has a pitch of $\Lambda = 2.85\ \mu m$.

temperature, which can be explained by the metal resistance reduces at low temperature. To characterize the mechanical component, the RF reflection coefficient S_{11} spectrum is measured at one IDT using a vector network analyzer (VNA) at different temperatures (Fig. 5.14) inside a 4 K cryogenic probe station (See Appendix II for measurement setup). Based on finite element analysis, the resonance signal $\sim$ 2.21 GHz corresponds to the desired acoustic L_0 mode. The L_0 has a dominant shear displacement field, which enables the optomechanical coupling between the two optical modes traveling inside the OMR. The resonance signal becomes stronger at cryogenic temperature, indicating a higher electromechanical conversion efficiency η_{em}. Applying the modified Butterworth Van Dyke (mBVD) model [24] to the measured S_{11} spectrum yields $\eta_{\text{em}} = 70\%$ at 4K.

Then we proceed with characterization of the acoustic transmission. We measure the acoustic

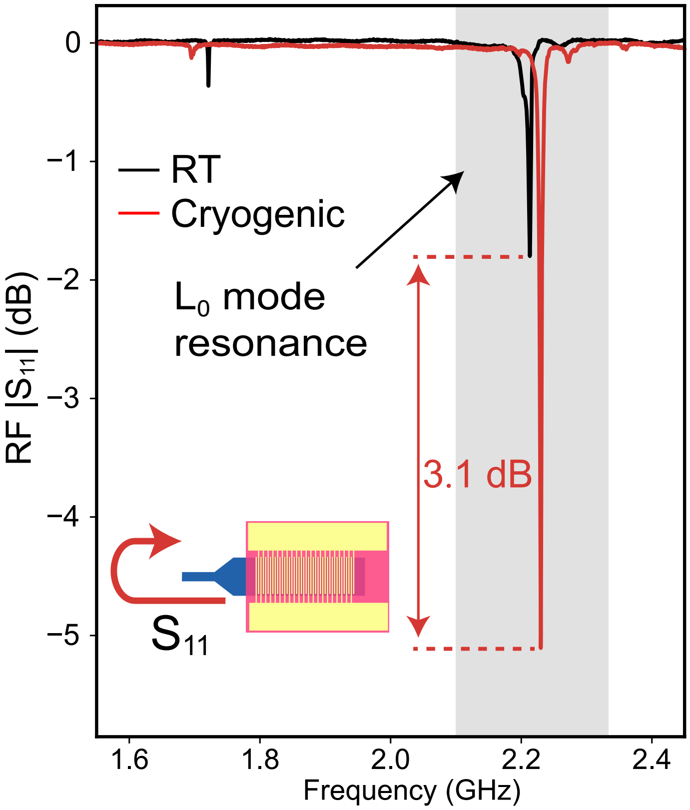

Figure 5.14: Radio-frequency reflection spectrum (S_{11}) of the IDT The inset shows an illustration of the S_{11} signal direction.

transmission spectrum $S_2 1$ by using a pair of IDTs on the opposite end of the acoustic waveguide. The phononic resonant property of the OMR is investigated by the RF transmission coefficient S_{21} spectrum, which measured the transmitted power ratio that propagates through the phononic waveguide and the OMR. The S_{21} is susceptible to free-space crosstalk, so, a time-domain gating technique is generally used to filter out the signal in the time-domain that is much faster than the expected acoustic responses [69]. The S_{21} is measured with two IDTs on the opposite side of the phononic waveguide at RF driving power 0 dBm. We filter out the signal outside 175–700 ns to remove the crosstalk. The main transmission signal centered at 2.21 GHz has a −3-dB bandwidth of 23 MHz, which is determined by the IDT design. Inside the transmission window, several evenly spaced resonance dips can be seen. These dips correspond to the resonance frequencies of the phononic mode circulating within the OMR (Fig. 5.15). The signal intensity of the transmission window at cryogenic temperature is ~ 3 times stronger than that at RT, which is explained by the reduced phonon scattering at lower temperature [51] and the increased η_{em} of the IDT. The highest phononic intrinsic quality factor $Q_a = 3,000$ (1,000) at 4K (RT). A temperature dependent acoustic loss characterization is also performed, which shows a dominant loss channel to be the thermal phonon scattering in the material.

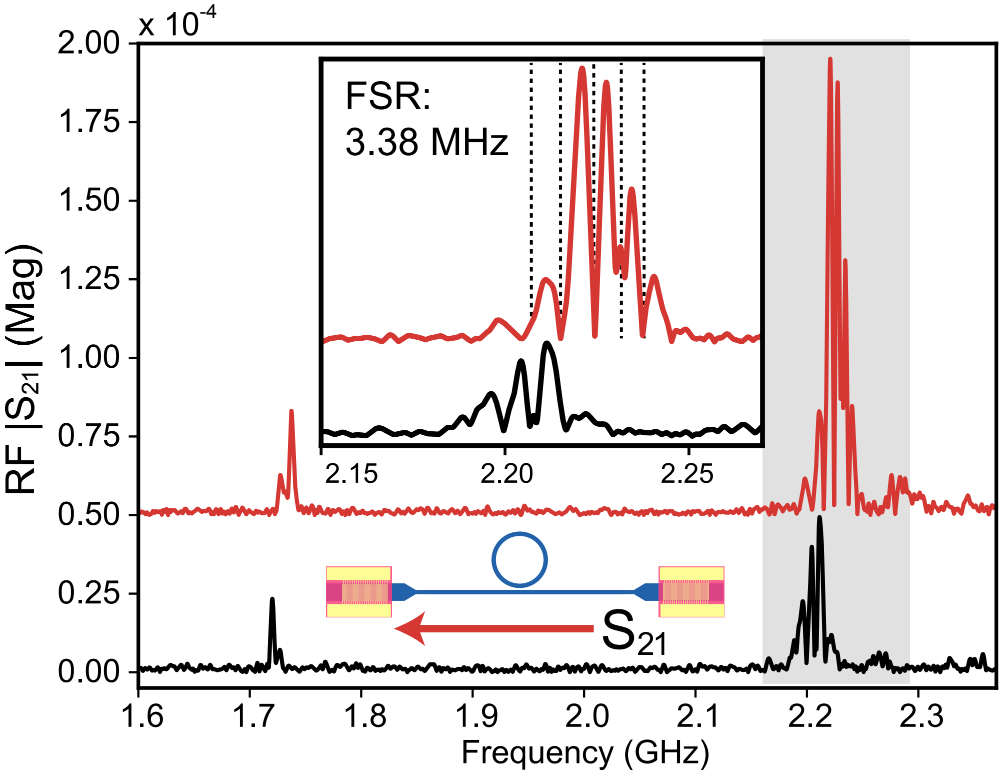

Figure 5.15: Radio-frequency transmission spectrum (S_{21}) of the acoustic wave The inset shows an illustration of the S_{21} signal direction.

Following the acoustic characterization, we shine a tunable laser around 1550 nm through the TE_0 (TE_1) input port which couples to the OMR and monitor the optical power via the respective drop port output. A photodetector receives the output signal from the GC as the laser sweeps over resonant wavelengths. The traveling optical wave constructively interferes at the out-coupled region, which results in a series of resonant peaks in the output spectrum. The free spectral range (FSR) of the output TE_0 and TE_1 port is used to determine the circulating mode in the OMR (Fig. 5.16b). The measured TE_0 and TE_1 FSR $\Delta\lambda_0 = 1.86$ nm and $\Delta\lambda_1 = 1.53$ nm match the simulated TE_0 and TE_1 mode ($\Delta\lambda_{0-sim} = 1.85$ nm and $\Delta\lambda_{1-sim} = 1.57$ nm), therefore, we can conclude that the desired mode is indeed circulating within the OMR. The highest TE_0 mode intrinsic optical quality factor $Q_o = 103,800$ is extracted from fitting the resonance signal with a Lorentzian function (Fig. 5.16a).

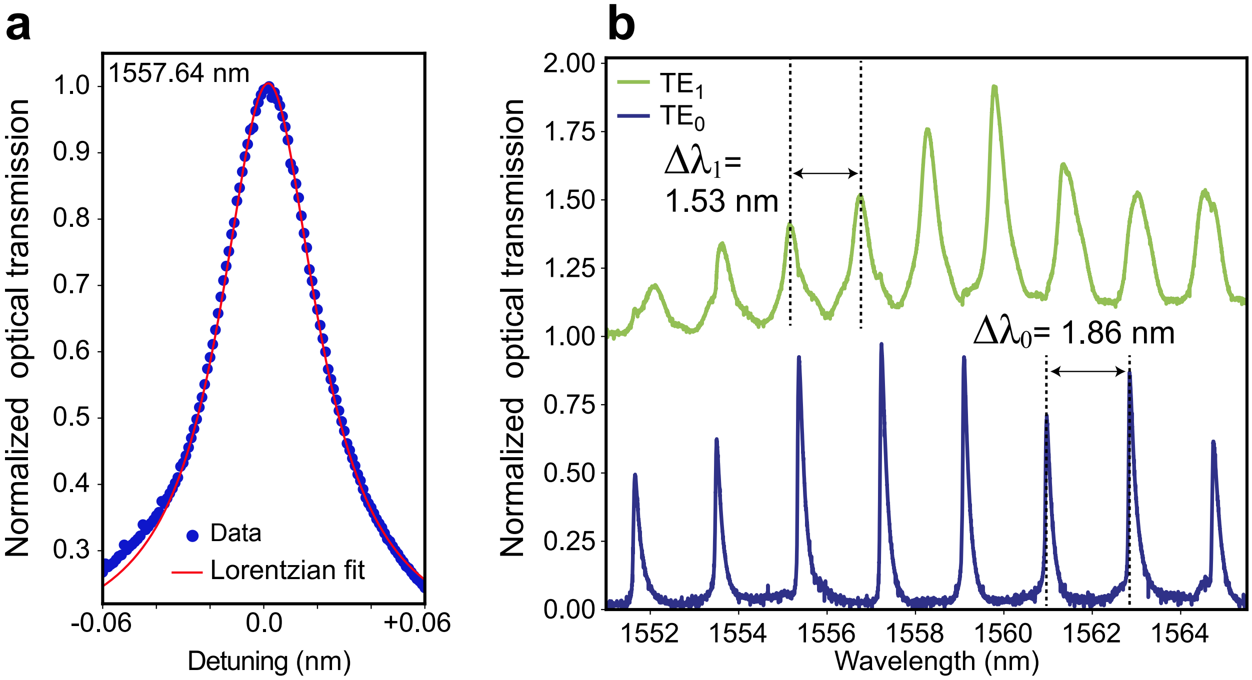

Figure 5.16: Optical transmission spectrum of TE_0 and TE_1 ports a. Lorentzian fitting of the normalized transmission of the TE_0 output signal at 1557.64 nm. **b.** Normalized optical transmission of TE_0 and TE_1 output signal.

5.6 Optomechanical interaction in OMR

5.6.1 Continuous RF frequency driving

After the initial acoustic and optical characterizations, we turn our attention to the optomechanical interaction inside the OMR. First, we explain the measurement setup of a linear frequency sweep RF pump on the IDT. The measurement configuration can be shown in Fig. 5.17. In our experiment, the input carrier TE_0 mode is counter-propagating with the L_0 mode (Fig. 5.17a). The generated TE_1 signal inside the OMR is then out-coupled to the TE_1 waveguide and then read out by a high-speed photodetector (HPD), where the HPD signal is referenced to the RF driving frequency of the

VNA (Fig. 5.17b). To harness the triple resonances of the OMR, the optical TE_0 pumping is first fixed at 1555.8 nm, where TE_0 and TE_1 resonance has the large frequency overlap (Fig. 5.16b), with a pump power 5 dBm while the RF drive sweep across the IDT resonance frequency 2.21 GHz with a 0 dBm RF drive power. A typical HPD response (optical S_{21}) at RT and cryogenic temperature (Fig. 5.19) shows multiple evenly spaced peaks across the main signal at 2.20-2.24 GHz. In the S_{21} spectrum, the average peak spacing $\delta f_{avg} = 3.38$ MHz. This corresponds to an effective acoustic group velocity $v_{\text{L-eff}} = 1382$ m/s, which matches with the simulated dispersion curve in simulation ($v_{\text{L-sim}} = 1300$ m/s). In theory, only one resonance should be effectively phase-matched, however, we see multiple resonances at the main transmission window.

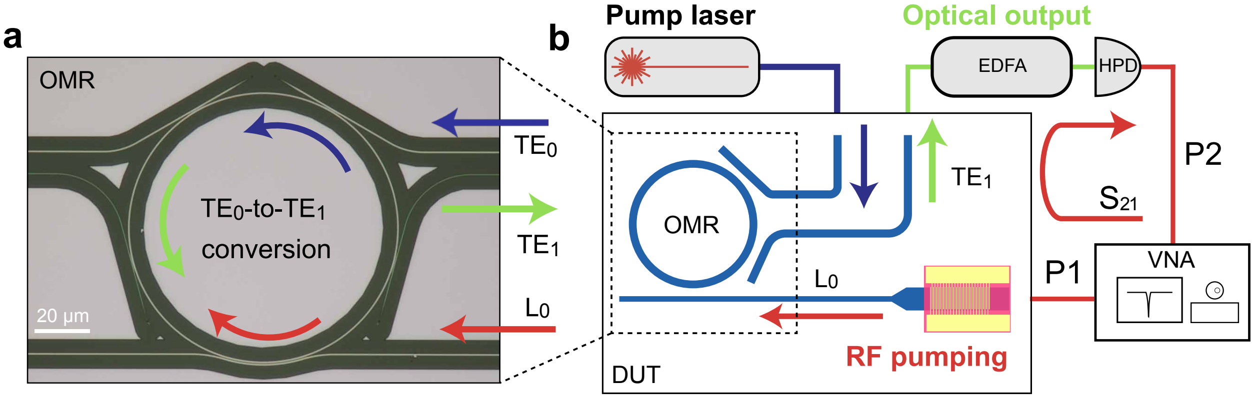

Figure 5.17: Measurement setup for RF frequency sweep RF pump a. Input signal configuration of the TE_0-to-TE_1 intermodal scattering experiment. The TE_0 (L_0) mode's propagation direction is indicated as blue (red) arrow. The TE_1 is generated via Brillouin scattering inside the OMR and coupled out through the TE_1 output port (green arrow). **b.** A simplified optical S_{21} measurement schematic. EDFA: erbium-doped fiber amplifier, HPD: high-speed photodetector, VNA: vector network analyzer.

For instance, the full-width-half-maximum (FWHM) of a photonic resonance $\delta\lambda = 0.3$ nm at 1550 ($Q_o \sim 46,500$) corresponds to a bandwidth $\delta f = 35$ GHz. But, a phononic resonance at 2.2 GHz with a quality factor $Q_a \sim 5000$ only has a bandwidth of several MHz. This effect is illustrated in Fig. 5.18, where a single optical pump can be scattered into multiple phononic resonances that reside within one photonic resonance. We observe a similar optical response at both RT and 4K cryogenic temperature, this suggests that strong optomechanical interaction coupling between the photonic and phononic modes.

To further explore the capability of our system, we construct a 2-D map of the system response

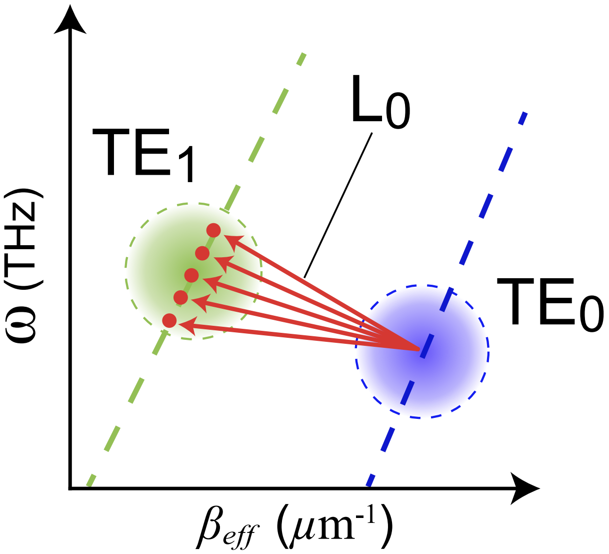

Figure 5.18: Intermodal scattering direction. Illustration of multiple phononic resonances reside within one photonic resonance. The red circles indicate the phononic resonance. The blue (green) translucent area indicate the finite TE$_0$ (TE$_1$) momentum and frequency spread on the dispersion diagram.

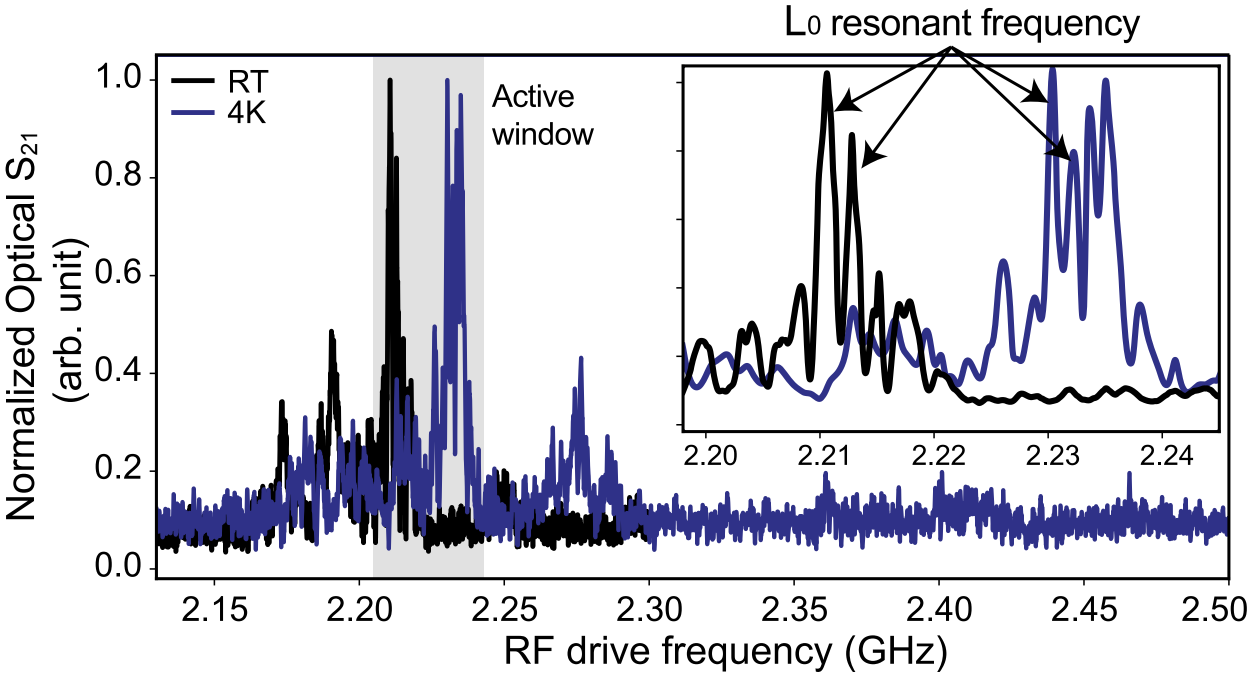

Figure 5.19: Multiple resonances inside an optical resonance Optical S_{21} spectrum of the multi-resonance intermodal scattering response at RT and 4 K. Inset: zoom-in of the optical S_{21} at 2.20-2.25 GHz.

under simultaneous optical and RF frequency sweeps. Using the same configuration as in Fig. 5.17b, we perform a step-wise wavelength sweep using the tunable laser from 1555 to 1561 nm at an optical input power 5 dBm while the RF drive is fixed at a linear sweep from 2.15 to 2.25 GHz at an RF drive power 10 dBm. The output optical signal is sent to the HPD and the response is referenced to the RF drive frequency. The resulting optical S_{21} map (Fig. 5.20) shows similar characteristic as in the single-frequency optical-pump condition. We also observe a 10 dB signal-to-noise ratio (SNR) between the on- and off-resonance optical pumping (the horizontal bright and dark streaks). In addition to a large SNR, we also observe fringe-like features on the 2D map. The bright vertical fringes corresponds to the case where both photonic and phononic resonant conditions are met, while the dark fringes represent only the optical resonance conditions are met. This shows that our device is capable of operating at multiple optical resonance frequency driving, allowing a wavelength-frequency-division multiplexing functionality as demonstrated in Fig. 5.21. We show the optomechanical resonances converts microwave signal at multiple resonances from 1537.55 nm to 1563.17 nm.

5.6.2 Single RF frequency driving

The anti-Stokes scattering process of our system can also be described using the interaction Hamiltonian using

$$H_{\text{int}} = \hbar G_b(\hat{a_1}\hat{a_0}^\dagger + \hat{a_1}^\dagger\hat{a_0}) \tag{5.34}$$

when $\Delta = +\Omega$, $\delta_\beta = -q$, and the carrier signal b is treated as a classical pump $\hat{b} \rightarrow \langle\hat{b}\rangle$. In essence, the propagating phononic mode introduces a new wavevector degree of freedom that allows the beam-splitter Hamiltonian to translate microwave signals into the optical domain. Moreover, this traveling-wave optomechanical architecture mitigates the parasitic down-conversion effect typically observed in multi-modal cavity systems [85].

To spectrally resolve different frequency components involved in our system, a heterodyne measurement scheme is utilized (Fig. 5.22b and Methods). The tunable laser signal is first separated into a pump and a reference signal. Then, an acousto-optic frequency shifter (AOFS) shifts the reference signal by $\delta/2\pi = 102.9$ MHz, which is later combined with the device output signal. Finally,

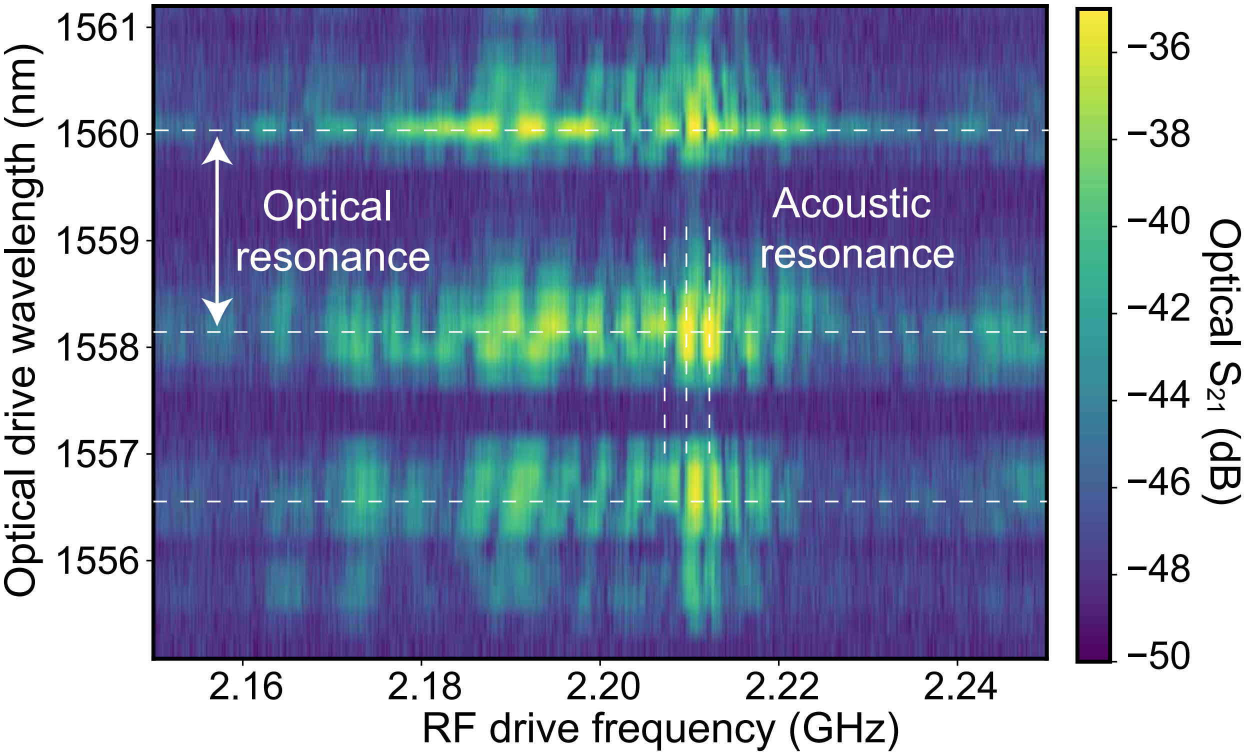

Figure 5.20: A constellation of the optomechanical co-resonance A 2D map of the optical S_{21} spectrum. The VNA is driving the IDT over a linear RF frequency sweep from 2.15 to 2.25 GHz, while the input laser is performing a 0.25 nm stepwise sweep. The data acquired on VNA is averaged 50 times at each laser sweep step.

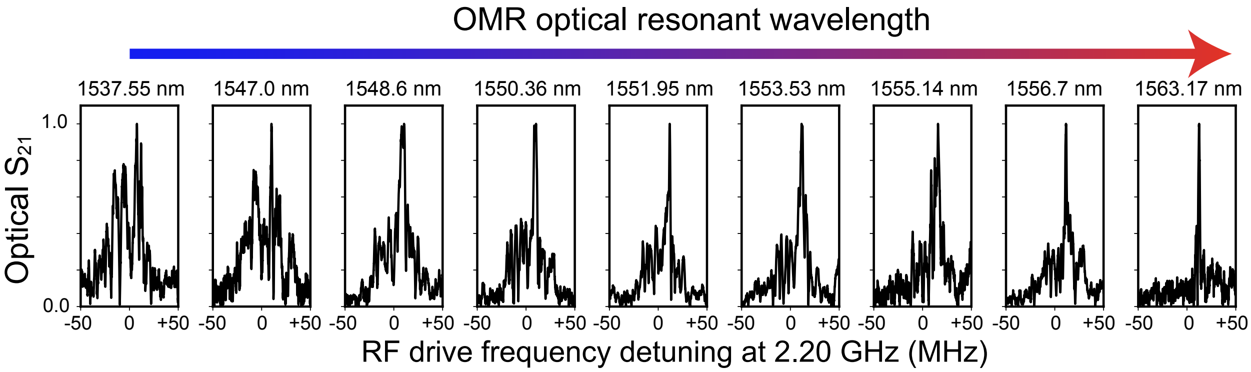

Figure 5.21: Multichannel microwave-to-optical conversion Optical S_{21} spectrum at various optical resonant channel. The VNA is driving across the same RF frequency while changing the optical resonant frequency.

the combined signal is detected by an HPD that is connected to a real-time spectrum analyzer (RSA). A beating signal spectrum of the counter-propagating anti-Stokes process (Fig. 5.22a) is shown in Fig. 5.23c for an RF drive frequency of $\Omega/2\pi = 2.21$ GHz. Four distinct beating tones are relevant to this experiment: (1) P_r, the unscattered reference signal at $\delta/2\pi = 102.9$ MHz. (2) P_{AS}, the anti-Stokes (phonon absorption) signal at $(\Omega - \delta)/2\pi = 2.107$ GHz. (3) P_S, the Stokes (phonon emission) signal at $(\Omega + \delta)/2\pi = 2.312$ GHz. And (4) P_0, the self-interference tone at $\Omega/2\pi = 2.21$ GHz. The 8 dB signal intensity asymmetry of P_{AS} and P_S verifies that the counter-propagating phononic mode dominates the scattering process, which is consistent with the theoretical prediction. In a closer inspection of the self-interference tone, we observe a P_0 signal intensity variation at different optical pumping wavelength. This self-interference (homodyne) tone origins from the Stokes and anti-Stokes scattered signal beating with the unscattered pump signal. As we change the optical pump wavelength, we observe a certain wavelength doesn't generate this homodyne signal, this implies that either the unscattered pump does not couple to the output port or the unscattered pump is depleted. Both of the case is ideal in our system.

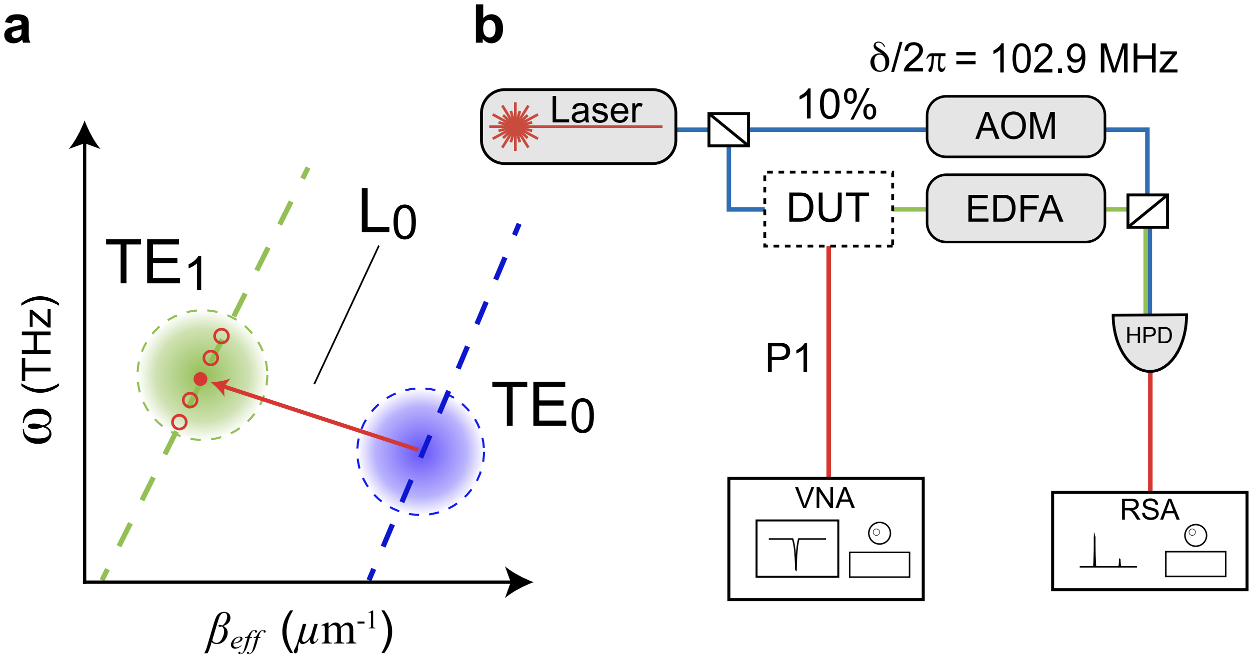

Figure 5.22: Single RF frequency driving set up a. Phase-matching condition of a single frequency intermodal scattering. The solid circle and the arrow indicate the phononic resonance and the RF drive to satisfy the phase-matching. **b.** A simplified heterodyne measurement schematic. EDFA: erbium-doped fiber amplifier, RSA: real-time spectrum analyzer, AOFS: acousto-optic frequency shifter. The reference signal is generated by shifting the laser frequency by $\delta/2\pi = 102.9$ MHz using an AOFS.

To assess the transduction efficiency and the optomechanical coupling coefficient, we analyze the acoustic scattering signal P_{AS} and P_S across varying RF drive power (Fig. 5.24a). The measurements were conducted with a tunable laser pumped on resonance at 1555.8 nm with a 10 dBm input power. We observe that P_{AS} and P_S increases as the RF drive amplitude increases (Fig. 5.24a). However, a distinct oscillatory behavior appears in the P_{AS} signal (Fig. 5.24b right panel). To better understand this, we model our system using a scattering matrix analysis, which takes the known device parameters such as the total loss rates and the number of ports. This model allows us to estimate the coupling coefficient of the system, which models both the Stokes and anti-Stokes signal as a function of the RF drive amplitude. The fitted results are shown as the black line in Fig. 5.24b. As a result, we extract a $P_{\mathrm{sat}} = 3.6$ mW at 4K. And the highest TE$_0$-to-TE$_1$ mode conversion efficiency is 1.2% at 3.6 mW RF drive power. We can also extract a microwave power normalized optomechanical coupling coefficient using the following formula

$$G_b = g_0 \frac{\sqrt{\kappa_b} S_{b+}}{i(\Delta_\Omega) + (\gamma_b + \kappa_b)/2}, \tag{5.35}$$

where κ_b (γ_b) is the extrinsic (intrinsic) coupling rate of the mechanical mode of the OMR, S_{b+} is the mechanical driving amplitude, and Δ_Ω is the RF detuning. And the calculated $G_b = 3.655$ GHz (mW)$^{-1/2}$. At the same time, we have $G_b = g_0\langle\hat{b}\rangle$. A single phonon at $f = 2.21\,\mathrm{GHz}$ corresponds to an energy $E = hf \approx 1.5 \times 10^{-21}$ J. Taking into account the electromechanical efficiency $\eta_{em} \approx 0.70$, 1 mW of RF power corresponds to 0.70 mW of phonons in the waveguide. And We can find the intrinsic optomechanical coupling rate

$$|g_0| = \frac{3.6\,\mathrm{GHz}}{\langle|\hat{b}|\rangle} \approx 350\,\mathrm{Hz}. \tag{5.36}$$

A microwave-to-optical transduction efficiency is calculated to be 1.5×10^{-5} with a 10 mW optical power.

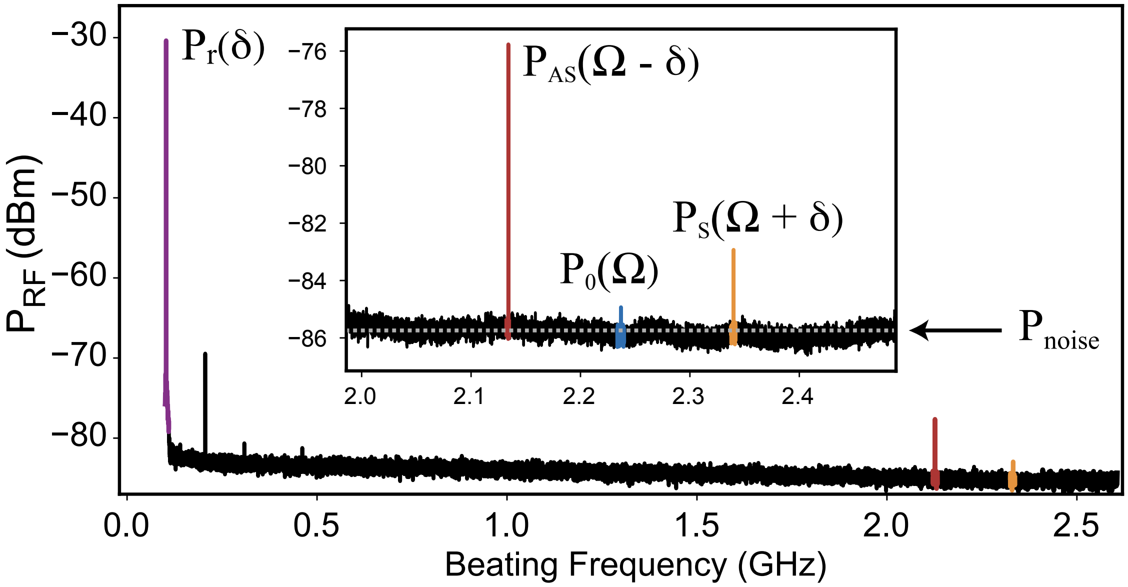

Figure 5.23: A heterodyne spectrum of OMR A broadband spectrum of the heterodyne response. The red and yellow signals correspond to the anti-Stokes $P_{\mathrm{AS}}(\Omega-\delta)$ and Stokes $P_{\mathrm{S}}(\Omega+\delta)$ signals of the optomechanical ring resonator (OMR), respectively. The purple self-interference signal $P_{\mathrm{r}}(\delta)$ is generated by the interference of the unscattered TE_0 mode and the Brillouin scattered signal. Inset: zoom-in of the signals $P_{\mathrm{AS}}(\Omega-\delta)$, $P_{\mathrm{r}}(\Omega)$, and $P_{\mathrm{S}}(\Omega+\delta)$.

5.7 Summary

In summary, we demonstrate a OMIC using commercial SOS, which has a robust design with non-suspended material platform, as improved from our previous work [2]. With a high acousto-optics figure-of-merit of silicon and a large acoustic velocity contrast, SOS is an ideal platform for non-suspended optomechanical architectures. The non-suspended sapphire heat-sink [86] also mitigates the photothermal effect of optical pump power [87], which is one of the critical challenge in achieving high efficiency microwave-to-optical conversion at single-photon level. Alternatively, 2D optomechanical crystals [88, 89] can also be used to reduce the photothermal effect, but the delicate structures are needed which limit the scalability and the compatibility to superconducting qubits. The sapphire substrate's compatibility with superconducting electronics also makes it a desirable monolithic platform to integrate quantum photonic and electronic devices on-chip, such as high-quality-factor superconducting resonators [90]. Despite the non-ideal photonic and phononic loss in the SOS, a GHz pump-enhanced coupling rate is achieved by harnessing the co-resonance of pho-

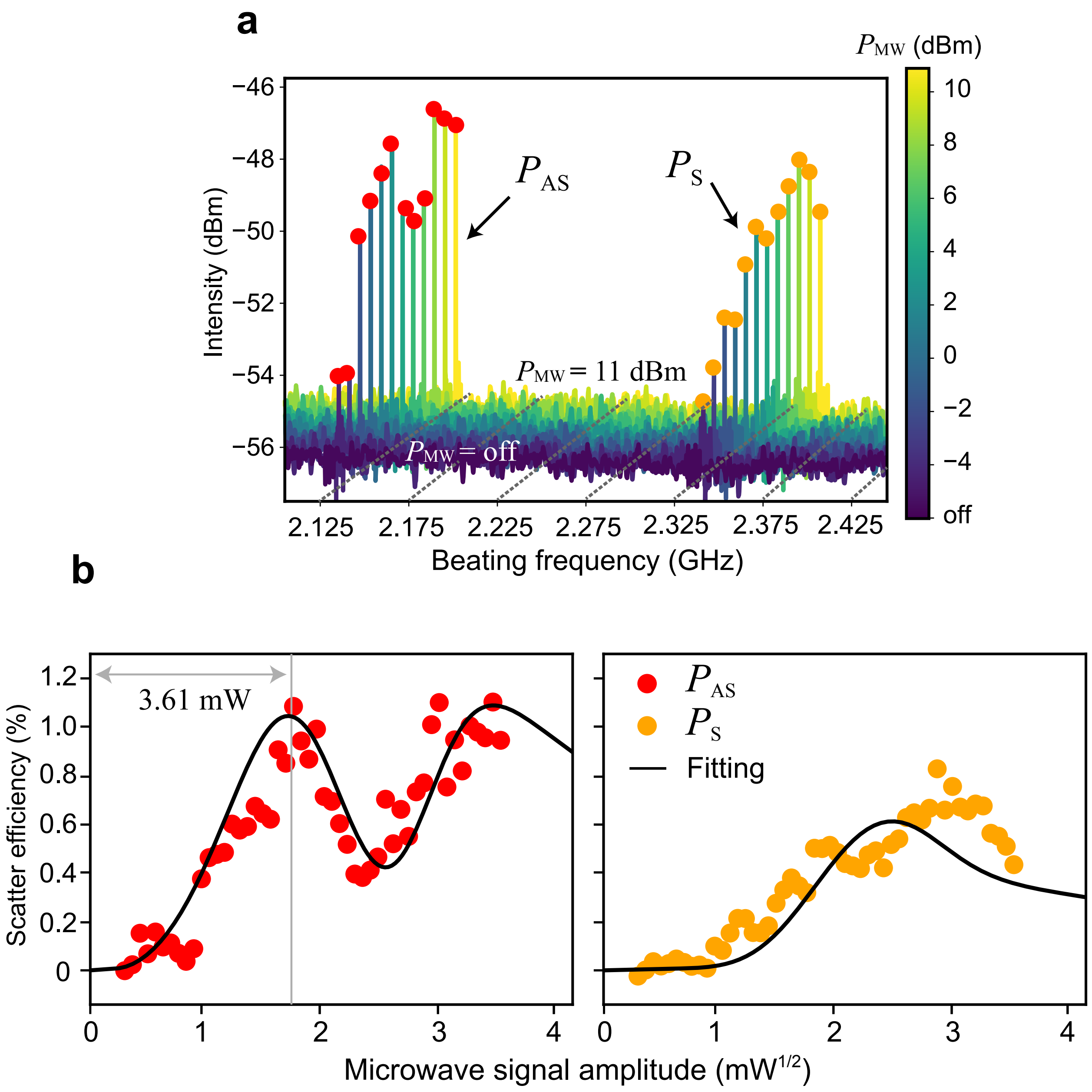

Figure 5.24: A heterodyne spectrum of OMR a. A waterfall plot of anti-Stokes and Stokes signals, with each trace vertically offset according to its corresponding RF power level. The baseline measurement, shown at the bottom, was taken with the RF pump disabled. The gray dotted line serves as a reference for the x-axis values. **b.** The traced intensity of the Stokes and anti-Stokes signal as a function of the RF drive amplitude. A fitted curve using the OMR system input-output formalism is also plotted.

tonic and phononic modes. Our OMR's g_0 exceeds similar triply resonant electro-optic systems [91] by a factor of 10 ($g_0 = 30$ Hz). However, it remains approximately three orders lower than the state-of-the-art piezo-optomechanical quantum transducer [89] (g_0 = 919 kHz). A finite element analysis (FEA) estimates the theoretical $g_0 \simeq 15$ kHz of an OMR with ring radius $r = 20$ μm. (see Supplementary Note 1D for the FEA simulation detail). The sapphire heat-sink also enables a possible high power optical pump that result in a high pump-enhanced coupling rate. Several improvements can be engineered to further increase the experimental g_0: instead of using four different photonic waveguides to couple to the OMR, as presented in the current design, a single photonic multimode waveguide can be used to reduce the photonic loss channels. Furthermore, by optimizing the mode overlap incorporating a cryogenic optical resonance tuning mechanism [4] would also improve the experimental g_0. Finally, with the OMR demonstrated on the SOS, the material platform is promising for classical applications such as optical mode converters [29], frequency shifters [92], non-magnetic optical isolators [93], or, quantum applications, such as microwave-to-optical quantum transduction and multichannel optical readout for superconducting qubits [94].

Chapter 6

Outlook and challenges of OMR

In this chapter, we discuss the possibility of using the OMR to achieve optical readout and reduce the need for RF cables in a dilution refrigerator. One of the main challenges is to achieve a perfect phase-matching condition due to the momentum and frequency mismatch in the OMR system. A tunable resonance via electrical control is desirable for achieving high optommechanical coupling rate. Here we discuss a potential solution to achieve an ideal phase-mismatch using phase-changing materials.

6.1 Challenges of achieving phase-matching condition in OMR

The progress of cryogenic microwave-optical transducers has achieved impressive results such as a high conversion efficiency (93.1%) using optomechanical crystals [89] and demonstration of qubit optical readout [95, 96]. Still, there are a lot of challenges toward a truly scalable optical readout, or optical interconnect. This includes the high optical pump power required for microwave-optical frequency conversion, the low bandwidth of the device, and the open question of how to integrate a transducer with multiple qubits. The OMR that we developed is trying to address the high pump power issue by moving to a co-resonance ring type cavity, where co-resonant optical and acoustic modes enhance this microwave-to-optical conversion process. And use a non-suspended material platform such as silicon-on-sapphire (SOS) that further decrease the thermal energy build-up by introducing a sapphire substrate to dissipate the heats generated in the process. The bandwidth issue is partly addressed by the multi-operational channels at different resonances that could also perform the microwave-to-optical conversion. Nonetheless, the microwave-to-optical conversion efficiency is still limited ($10^{-5} \sim 10^{-3}$ %). Consider that OMR has only been first demonstrated in 2023, this efficiency is already comparable to some early works done using optomechanical crystals and electro-optical cavities [13, 97]. With mode overlap and device design optimization, we expect a higher efficiency can be achieved without sacrificing the intrinsic advantages of the OMR. Another critical issue is the satisfying of the phase-matching condition between the acoustic and optical modes. Without a phase-matching, the co-resonance effect could not be fully exploited. Therefore, a method to control the resonance frequency is ideal to achieve a practical microwave-to-optical transducer.

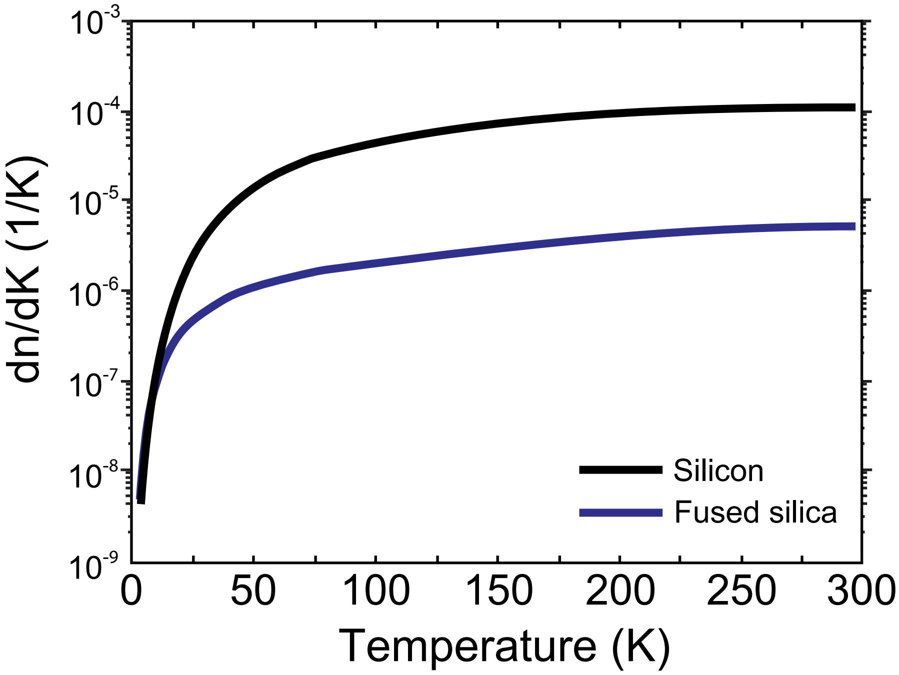

Figure 6.1: Thermal-optic coefficient of silicon at 1550 nm and cryogenic temperatures Thermo-optic coefficients of silicon and fused silicon at 1550 nm at various temperature. This figure is reproduced from [3] under CCBY license.

A common method to tune the optical resonances is through the thermo-optic effect—a change of refractive index due to thermal energy. In conventional photonic integrated circuit, a metal pad is fabricated next to the waveguides to tune the refractive index by applying current to heat up the waveguides. However, the thermo-optic effect is extremely weak (silicon's thermo-optic coefficient degrades from $\sim 10^{-4}$ at 300K to $\sim 10^{-4}$ at 4K, as shown in Fig. 6.1) [3]. In addition, to maintain the thermo-optic effect, a constant DC current is needed, this would result in a large power dissipation, which is not ideal due to the limited cooling power budget of a dilution refrigerator. Therefore, it is important to develop a non-volatile resonance tuning mechanics to achieve resonance tuning on the OMR.

6.2 Phase-change materials photonic resonance tuning

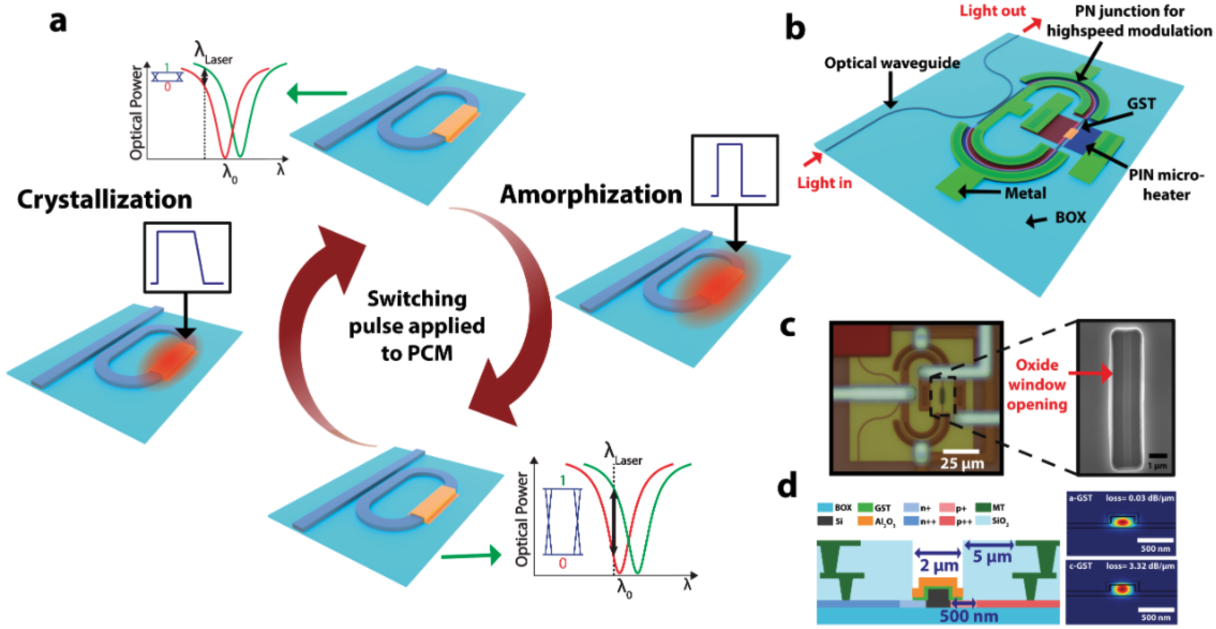

Figure 6.2: **a** The concept of tuning the MRM resonance in a non-volatile fashion using cryogenic PCM, **b** Device illustration of PIN micro-heater integrated with racetrack MRM, **c** Cross-section of PIN micro-heater and mode profile simulation with 10nm-thick GST on the waveguide. This figure is reproduced from [4].

We try to address the aforementioned challenge by monolithic integration of non-volatile phase-change materials (PCM) with silicon photonics to tune a silicon micro-ring modulator (MRM) at sub-4K temperatures. MRM enables ultra-low-power modulation with a 10 GHz bandwidth using the free-carrier-plasma dispersion effect [98, 99], MRMs naturally support wavelength division multiplexing (WDM), allowing simultaneous communication over multiple wavelengths through a single fiber. On the other hand, PCM has two distinct states: amorphous or crystalline, with different optical refractive index. The PCM can be switched back-and-forth between the two states by applying heat pulses, and the state is non-volatile and requires no static current biasing once set. The principle of the resonant shifting is shown in Fig. 6.2. The photonic integrated chip (PIC) is fabricated using a commercial process on a silicon-on-insulator (SOI) substrate. A rib waveguide is designed with a PIN-micro-heater pad to enable PCM switching. The PCM is post-fabricated on the open window in the PIC using an in-house sputter in the Washington Nanofabrication Facility (WNF).

We characterize the resonance tuning by monitoring the MRM transmission spectrum at different state of the PCM. When we apply different heat pulse length to the heater, we can see the resonance is shifted, as seen if Fig. 6.3. We observe a multi-level switching of the PCM, indicating the optical resonances can be shifted continuously between the two states of the PCM. Furthermore, the optical transmission remains generally the same across different resonances, indicating the different state of PCM does not degrade the optical device performances.

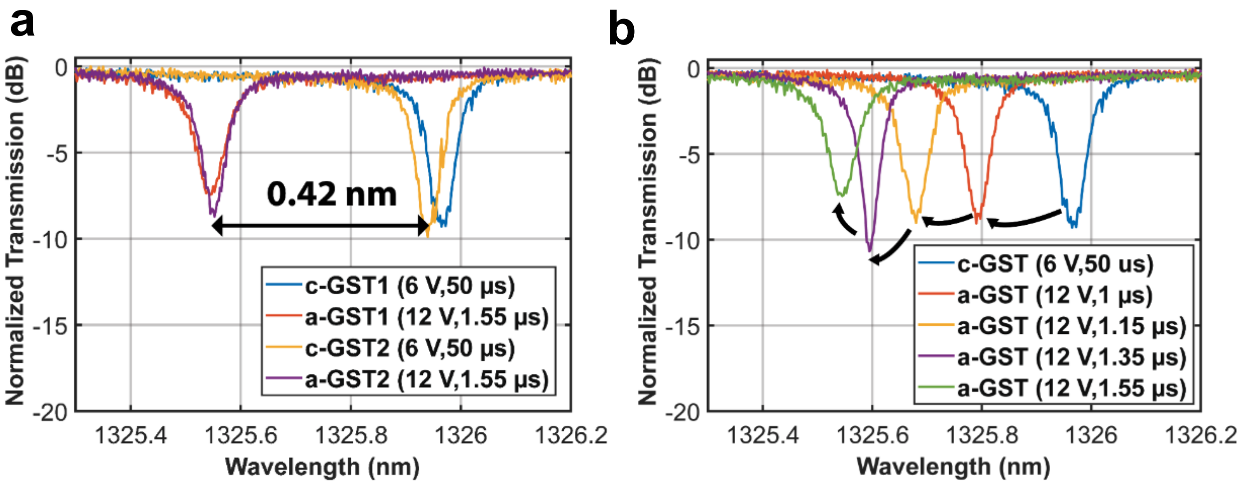

Figure 6.3: PCM tuning characterization: a Normalized transmission plot demonstrating the MRM phase shift induced by GST switching at 4K. **b** Multilevel switching of GST at 4K. This figure is reproduced from [4].

6.3 Applying PCM to OMR resonance tuning

One can imagine applying the resonance tuning mechanism to OMR to achieve better phase matching. The tuning range of the PCM is roughly 1 nm, which is well within the frequency mismatch of the TE_0 and TE_1 mode ($\sim 0.5\ nm$) presented in Chapter 5. By tuning the two optical mode completely align at the same frequency (at a bad optical cavity regime, i.e. optical linewidth $\kappa \gg$ acoustic linewidth γ), the co-resonance effect can be greatly enhanced. Furthermore, since the OMR is operation in the cryogenic 4 K temperature, once the PCM state is set and the phase-matching condition is satisfied, no additional power is required to maintain the optical biasing. One thing of concern is the higher optical loss introduced by the additional layer of the PCM on top of the silicon waveguide. As shown in Fig. 6.5, the crystalline GST has a higher refractive index, such that the optical mode profile is more concentrated to the dielectric-air boundary. More investigation is needed to determine the feasibility of integration between GST and OMR.

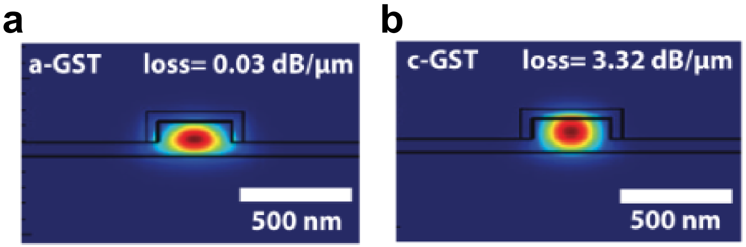

Figure 6.4: Optical mode profile of PCM on a silicon waveguide a. Amorphous GST on silicon-on-insulator **b.** Crystalline GST on silicon-on-insulator This figure is reproduced from [4].

6.4 Potential use case of OMR in a dilfridge

Using PCM is not the only way to tune the optical resonances under cryogenic temperature, other examples such as piezo-optomechanical tuning [100], electro-optics [10], and PN junctions tuning [99] are also demonstrated. Nonetheless, once the engineering problem of resonance tuning can be solved without degrading the microwave-to-optical conversion efficiency, we can think about where we should put these OMR devices. In this section, we discuss a way forward to put these OMR devices to practice.

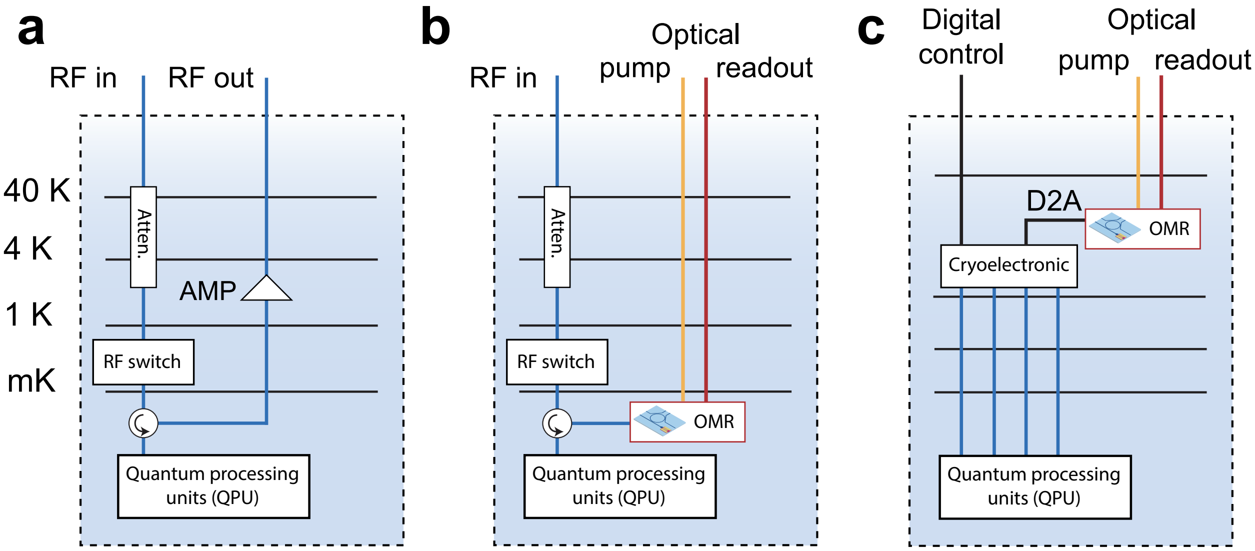

Figure 6.5: OMR's potential placement in a dilfridge. a. An all RF input-output controlling a superconducting based QPU. **b.** An optical readout using the OMR at millikelvin stage in a dilfridge. **c.** Using the OMR as a classical optical transmitter at 4 K stage.

The benefit of optical interconnect is the low heatload [101] from the optical fibers, replacing the bulky RF co-axial cables with the optical fibers could help the scaling of qubits in a dilfridge (Fig. 6.5a). First, if we still keep the input RF drive, and simply replacing the output RF lines with an optical readout, then roughly 50% of the heatload from the RF lines can be reduced, as the configuration shown in Fig. 6.5b. This configuration would require a direct interfacing between the QPU and the OMR, which is a coherent state swap between RF and optics. The benefit of this type of optical interconnect is a distributed entanglement can be achieved when the optical output is connected to another dilfridge. But, the efficiency and the fidelity requirement of the OMR would be much higher in this configuration. Another less demanding configuration is to use OMR as a classical optical transmitter at a 4K stage. A cryogenic digital electronic processor [102] is needed, however, the requirement on the OMR efficiency and fidelity is much relaxed. The optical signal can be modulated by the cryogenic processor and transmitted out of the dilfridge using optical fibers, as shown in Fig. 6.5c. This configuration can still benefit from the low heatload of the optical fibers and the scalability of the optical interconnect. The digital cryoelectronic must include all the RF components such as an arbitrary waveform generator (AWG), RF amplifier, digital-to-analog converter (DAC), analog-to-digital (ADC) converter, and so forth. Just like the server racks that is currently being used in the data center around the world.

6.5 Summary

In summary, achieving phase-matching OMR is crucial for efficient microwave-to-optical conversion. The integration of PCM with silicon photonics offers a promising solution for non-volatile resonance tuning at cryogenic temperatures. This method can significantly enhance the co-resonance effect and improve the overall conversion efficiency. Additionally, the potential use of OMR in a dilution refrigerator for optical interconnects presents a scalable approach to qubit readout and communication, reducing heat load and enabling distributed entanglement. Future work should focus on optimizing phase-matching condition and exploring other resonance tuning mechanisms to further improve performance.

Appendix I: Cryogenic probe station setup

Basic model of the VNA

We follow a few open source information to design a cryogenic calibration kit for dilfridge measurement IEEE paper, IN3OTD blog, and Henry's blog to help design the PCB board.

To know how to calibrate a VNA, we need to know what the error sources of a VNA are. We can model it in a certain way, but let's not get too much into the math here. In the 4 K Lakeshore cryostat, we calibrate the RF probes (50 μm and 100 μm pitch) with a calibration substrate CS-15 purchase from GGB inc. The calibration substrate has a short, open, 50 Ω load, and through (SOLT) calibration standards. However, in the mK emvironments, SOLT calibration is problematic, because the 50 Ω load at room-temperature is not 50 Ω at mK temperatures. Therefore, we use a through-reflect-line (TRL) calibration, which is a more accurate calibration method for cryogenic measurements and does not require a 50 Ω load.

Cryogenic probe station measurement setup

Figure. A.1 shows the measurement setup that is used for all measurements in the main text. The fiber array probe consists of four channels: two channels are used as inputs and the other two as outputs. The input optical switch (OS1) is used to control the input optical mode based on different optical polarization. For instance, bar (cross) state optical switch is for TE_0 (TE_1)

input. One fiber array output channel connects to a photodetector (PD0) for optical alignment. And the second fiber array output connects to an output optical switch (OS2), which configures the output signal to be received by either a photodetector (PD1) or a high-speed photodetector (HPD). The HPD signal output is connected to an RSA for heterodyne experiment and a VNA for the optical S_{21} measurements. In the heterodyne experiment, 10% of the laser input power is used as a reference arm, which is frequency-shifted by the acousto-optic frequency shifter (AOFS). This reference arm is then combined with the device under test (DUT) output signal during the heterodyne measurement.

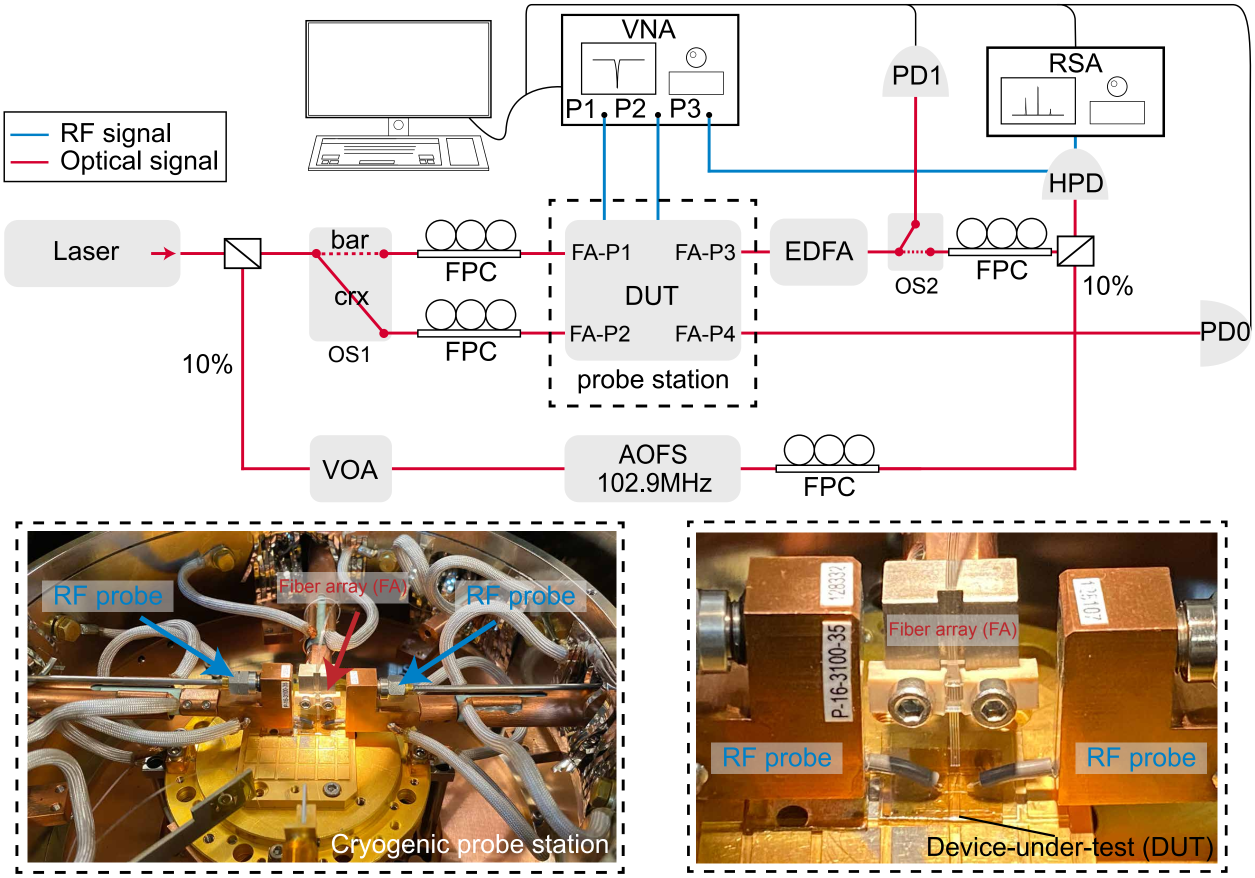

Figure A.1: The measurement setup. Acronyms: OS: optical switch, FPC: fiber polarization controller, FA: fiber array, EDFA: erbium-doped fiber amplifier, PD: photodetector, HPD: high-speed photodetector, VOA: variational optical attenuator, AOFS: acousto-optic frequency shifter, DUT: device-under-test, VNA: vector network analyzer, RSA: real-time spectrum analyzer.

Appendix II: Butterworth Van-Dyke (BVD) electromechanical conversion efficiency fitting

Lumped element modeling

Circuit Model and the Physical Meaning of Each Circuit Elements

The electromechanical conversion process in our system can be described using the modified Butterworth Van-Dyke (BVD) model [103]. The effective BVD circuit (Fig. A.2a) consist of the mechanical lumped elements: R_m, L_m, and C_m. The effective circuits of these elements can be further abstracted to a mechanical impedance Z_m. This is the component that generates the acoustic waves in our effective circuit. Apart from the mechanical elements, the mBVD also includes a series resistance R_s and series inductance L_s. The series resistance represents the metal electrodes behavior of the IDT, ideally. Furthermore, a parallel capacitance C_p and resistance R_p represents the capacitance and resistance between the electrode pair.

The RF reflection spectrum is measured on a vector network analyzer (VNA) (Keysight N5230C PNA-L), on a cryogenic probe station (Lakeshore CRX-4K). The VNA was calibrated at room-temperature and under vacuum, to the tips of the RF probes as the reference using a calibration substrate (GGB Inc. CS-15). To extract the IDT's electromechanical conversion efficiency, we use the BVD effective circuit, as shown in Fig. A.2a, to obtain the value of the circuit lump elements

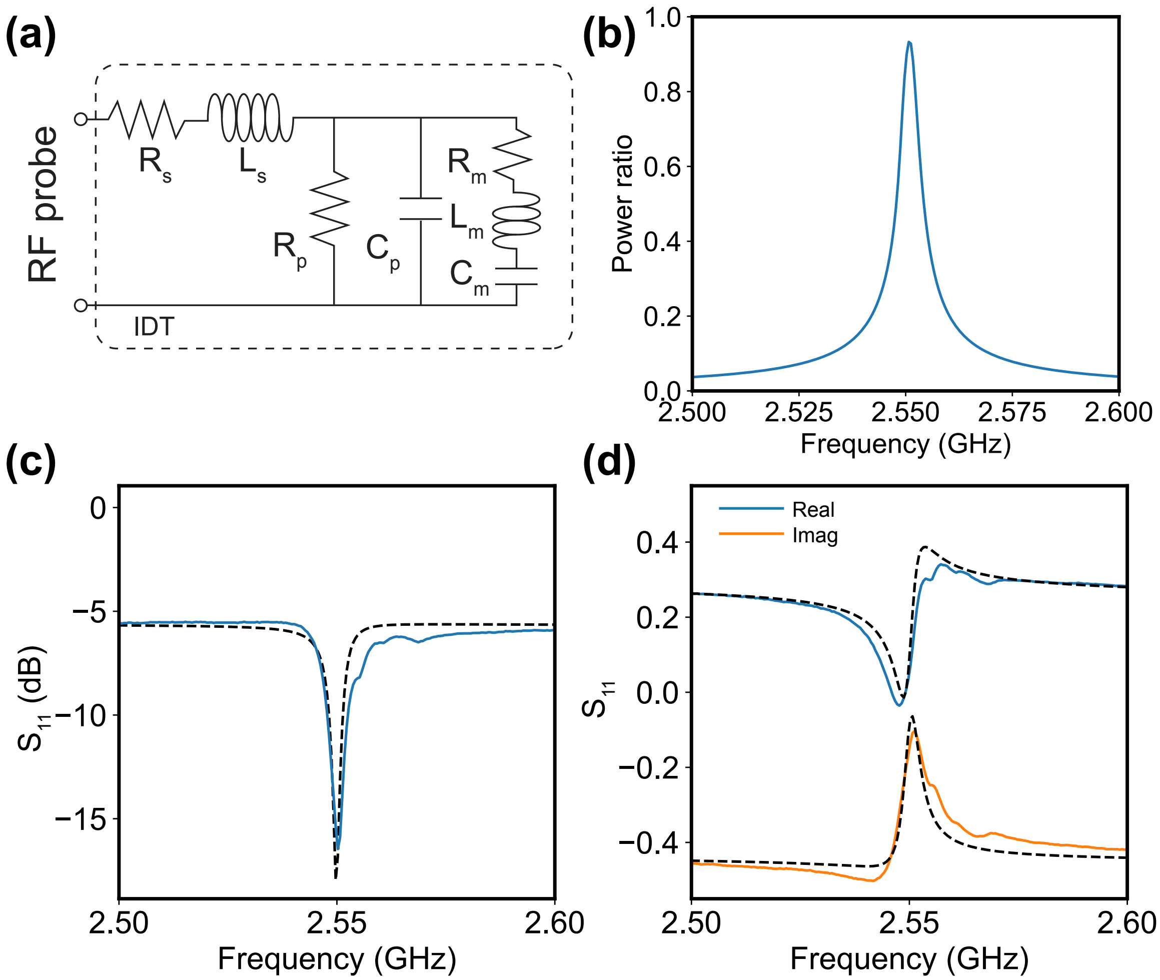

Figure A.2: Fitting result of the mBVD model at $4\ K$ **(a)** The mBVD model that is used to fit the RF reflection spectrum (S_{11}). **(b)** The ratio of electrical power dissipated on the mechanical lumped element (R_m), which corresponds to the power converted to the mechanical power. **(c)** The measured S_{11} spectrum (solid blue line) and the mBVD model fitting (black dashed line). **(d)** The real and imaginary part of the S_{11} spectrum of the measured IDT. The dashed lines are the mBVD fitting.

and calculate the power load on the motional elements. We can express the load impedance Z_{L} as:

$$Z_{\mathrm{total}} = Z_s + Z_{\mathrm{L}}, \tag{A.1}$$

$$Z_s = R_s + j\omega L_s, \tag{A.2}$$

$$Z_{\mathrm{L}} = \left(\frac{1}{Z_p} + \sum_N Y_m^{(N)}(\omega) \right)^{-1}, \tag{A.3}$$

$$Z_p = \frac{1}{j\omega C_p + 1/R_p} \tag{A.4}$$

$$Y_m(\omega) = \frac{1}{Z_m} = \frac{1}{R_m + j\omega L_m + 1/j\omega C_m}. \tag{A.5}$$

R_s accounts for the total resistance between the RF probe and the IDT and L_0 accounts for the inductive background signal of the free space RF signal. The shunt resistor R_p accounts for the power dissipation/loss of the dielectric, while the shunt capacitor C_p accounts for the static capacitance of the IDT the electrodes. $L_m(\omega)$, $C_m(\omega)$, and $R_m(\omega)$ are the mechanical elements at the target resonance frequency. We can combine C_p and R_p as effective load Z_p. In our case, we only fit one resonance, therefore $N = 1$. The BVD model fit of Z_L is shown in Fig. A.2b and the $|S_{11}|$ fit is shown in Fig. A.2c. The BVD model fitting is consistent with the acquired S_{11} data, and is used to extract the electromechanical conversion efficiency. Similar methods are used in previous works [103, 24]. The estimation of the electromechanical efficiency using BVD model fitting has a $< 5\%$ deviation from direct measurement. After extracting the lump element values, we can calculate the voltage V_{Y_m} and current I_{Y_m} across Y_m using the Ohm's law. We find the power ratio of the total input power that is loaded on Y_m to be

$$P_{Y_m} = Re\left[\tilde{V}_{Y_m} \cdot \tilde{I}^*_{Y_m}\right]. \tag{A.6}$$

The calculated power ratio on Y_m is shown in the inset of Fig. A.2c,which shows $\sim 80\%$ of the total input power is loaded on Y_m at 4 K.

The following shows the analytical equations of power distribution in each lumped elements, and we can use them to calculate the power ratio that is distributed on Y_m and thus calculate the RF to mechanical conversion efficiency. The effective circuit can first be simplified as a series connection of R_s and Z_L(The effective complex impedance of the R_p, C_p and Y_m). The power distribution on series resistance, P_{Rs}, and complex impedance, P_{Z_L} is

$$P_{Rs} = P_{in}\frac{R_s}{R_s + Re(Z_L(\omega))}$$

$$P_{Z_L} = P_{in}\frac{Re(Z_L(\omega))}{R_s + Re(Z_L(\omega))}.$$

We can then further analysis the power distribution on the three parallel component: P_{Rp}, P_{Cp} and P_{Ym}. Using the current and voltage relationship of parallel connected circuit elements, we can have the following equations

$$P_{R_p} = P_{Z_L}\frac{R_p^{-1}}{R_p^{-1} + Re(Y_m(\omega))}$$

$$P_{Y_m} = P_{Z_L}\frac{Re(Y_m(\omega))}{R_p^{-1} + Re(Y_m(\omega))}$$

$$P_{C_p} = 0.$$

Substituting P_{Z_L} on both equations above we can have

$$P_{R_p} = P_{in}\frac{Re(Z_L(\omega))}{R_s + Re(Z_L(\omega))}\frac{R_p^{-1}}{R_p^{-1} + Re(Y_m(\omega))} \tag{A.7}$$

$$P_{Y_m} = P_{in}\frac{Re(Z_L(\omega))}{R_s + Re(Z_L(\omega))}\frac{Re(Y_m(\omega))}{R_p^{-1} + Re(Y_m(\omega))} \tag{A.8}$$

where $Z_L(\omega) = (R_p)^{-1} + (1/j\omega C_p)^{-1} + (1/Y_m(\omega))^{-1}$, and P_{in} can be inferred from vector network analyzer (VNA) complex amplitude (polar chart) data, which we will explain on how to calculate in more detail later. Note that R_s, R_p and C_p can be fitted using the least squares curve fitting in python and are independent of frequency. And in this case we take $L_s = 0$.

Extract R_s, R_p and C_p from S11 data

To extract the lumped elements values from the equivalent circuit model, we perform the least square curve fit near the resonance peak ω **exclude** the admittance(Y_m) element to obtain R_s, R_p and C_p. The reason we can exclude the admittance(Y_a) is because that power reflected at the resonance peak (dip in the S11/reflected power plot) can be solely attributed to the effect of Y_m, which is a function of frequency ω. The total load impedance Z_0' after excluding Y_m then becomes

$$Z_0' = R_s + \frac{1}{R_p^{-1} + j\omega C_p}$$

where

$$Z_0' = R_{char} \times \frac{1+\mathbb{C}(S11(\omega))}{1-\mathbb{C}(S11(\omega))}, R_{char} = 50\Omega$$

Note that S11 is a complex number, which can be extracted from the polar chart in VNA. In this way, we can relate the measured data S11 to the lumped elements. An example of the fitting result from which we can extract R_s, R_l and C_e. The resulting R_s, R_p and C_p are 17.94Ω, 1641.00Ω and 6.45×10^{-4}nF in this example.

Extract Y_m from the fitted parameters

Since we have R_s, R_p and C_p at our hands, we can use them to calculate the admittance Y_m by re-apply Y_m in the equivalent circuit. The total impedance Z_0 **including** Y_m becomes

$$Z_0 = R_s + \frac{1}{R_p^{-1} + j\omega C_p + Y_m(\omega)} \equiv R_{char}\frac{1+\Gamma}{1-\Gamma} = R_{char} \times \frac{1+\mathbb{C}(S11(\omega))}{1-\mathbb{C}(S11(\omega))}$$

where Γ is the reflection coefficient and everything is known expect Y_m, so we can rearrange the equation and get

$$Y_m(\omega) = \frac{1}{Z_0 - R_s} - (\frac{1}{R_p} + j\omega C_p). \tag{A.9}$$

Estimate the Electromechanical Conversion Efficiency Using Y_m

Revisiting the power distribution analytical equations

In section6.5, we derive the power distribution equations of our effective circuit as shown in equation (1) and (2). So far, the total power input of the effective circuit, P_{in}, is the term that we still need to figure out. Using power-voltage relation equation $P = V^2/Z_0$, and we can represent the total load impedance(Z_0) using S parameter

$$P_{in} = \frac{V_{in}^2}{Z_0} = \frac{V_{in}^2}{R_{char}\frac{1+\mathbb{C}(S11(\omega))}{1-\mathbb{C}(S11(\omega))}} = \frac{V_{in}^2}{R_{char}}\frac{1-\mathbb{C}(S11(\omega))}{1+\mathbb{C}(S11(\omega))}. \tag{A.10}$$

And by plugging this result into equation (1) and (2), we will have

$$P_{R_p} = \frac{V_{in}^2}{R_{char}} \frac{1-\mathbb{C}(S11(\omega))}{1+\mathbb{C}(S11(\omega))} \frac{Re(Z_L(\omega))}{R_s + Re(Z_L(\omega))} \frac{R_p^{-1}}{R_p^{-1} + Re(Y_m(\omega))} \tag{A.11}$$

$$P_{Y_m} = \frac{V_{in}^2}{R_{char}} \frac{1-\mathbb{C}(S11(\omega))}{1+\mathbb{C}(S11(\omega))} \frac{Re(Z_L(\omega))}{R_s + Re(Z_L(\omega))} \frac{Re(Y_m(\omega))}{R_p^{-1} + Re(Y_m(\omega))} \tag{A.12}$$

Using numerical analysis to calculate power ratio

In reality, we approach the problem with numerical analysis to compute the power ratio between $P_R s$, P_{R_p} and P_{Y_m} in python. We know that the root-mean-square power distribution on each element can be written generally in the complex form

$$P_{RMS} = Re[\tilde{V} \cdot \tilde{I^*}]$$

where $\tilde{V}$ is the voltage in phaser form and $\tilde{I^*}$ is the complex conjugate of the current in phaser form. We can use equation (4) above to find out the V_{in} assuming the power input is normalized to 1. Then, we can have the following voltage and current relations of each lumped elements

$$\begin{aligned}
\tilde{V}_{in} &= \sqrt{\frac{(1+\Gamma)^2}{1-\Gamma^2} \cdot R_{Char} P_{in}} = \sqrt{\frac{(1+S_{11})^2}{1-S_{11}^2} \cdot R_{char} P_{in}} \\
\tilde{I}_{in} &= \frac{\tilde{V}_{in}}{Z_0} \\
\tilde{V}_{R_s} &= \tilde{I}_{R_s} \cdot R_{s_{\text{fit}}} \\
\tilde{I}_{R_s} &= \tilde{I}_{Z_L} = \tilde{I}_{in} \\
\tilde{V}_{Y_m} &= \tilde{V}_{in} - \tilde{V}_{R_s} \\
\tilde{I}_{Y_m} &= \tilde{V}_{Y_m} \cdot \tilde{Y}_{m_{\text{fit}}} \\
\tilde{V}_{R_p} &= \tilde{V}_{Y_m} \\
\tilde{I}_{R_p} &= \frac{\tilde{V}_{R_p}}{R_{p_{\text{fit}}}},
\end{aligned}$$

finally the power ratio of each element is

$$P_{R_s} = Re[\tilde{V}_{R_s} \cdot \tilde{I}^*_{R_s}] \tag{A.13}$$

$$P_{R_p} = Re[\tilde{V}_{R_p} \cdot \tilde{I}^*_{R_p}] \tag{A.14}$$

$$P_{Y_m} = Re[\tilde{V}_{Y_m} \cdot \tilde{I}^*_{Y_m}]. \tag{A.15}$$

Key part of Python source code

Listing 1: Python code

```
#Load ,fit data and spit out the normalized admittence.
#And show the lump elements of the fitted data
def f(cmplx_imp_opt, y_data):

    #Setup the least square fitting function

    cmplx_imp_data = 50*(1+y_data)/(1-y_data)
    residule = cmplx_imp_opt - cmplx_imp_data
    return residule

def f_wrap(x,freq,y_data):
    resSers = np.array(x[0]) #x[0]
    resLeak = np.array(x[1]) #x[1]
    capElcd = np.array(x[2]) #x[2]

    jOmega = 1j*2*np.pi*np.array(freq)*1e-9
    jOmegaCapElcd = jOmega*capElcd

    fx = f(x[0] + 1/(x[1]**(-1)+jOmega*x[2]) , y_data)
    #for i in range(len(fx)):
    return np.array([fx.real, fx.imag]).flatten()

def process_data(file_name,selected_fit_data):
```

```
print(file_name)
#import data with the given name
f1,r1,i1 = import_pol_data(file_name)
r1 = np.array(r1)
i1 = np.array(i1)
freq = np.array(f1)

#convert real and imaginary to complex Gamma
cmplGamma = r1 + i1*1j
phase = np.angle(cmplGamma)
r = (r1**2 + i1**2)**0.5

#Start the fitting process form the data

#Initialized the parameters
cmplImpChrt = 50
ftResSersInit = 6 # (Ohm)
ftResLeakInit = 300 # (Ohm)
ftCapElcdInit = 0.2e-4 # (nF)
ft_Init = [ftResSersInit,ftResLeakInit,ftCapElcdInit]

#From the imported frequency
freq_select = np.append(freq[selected_fit_data[0]:selected_fit_data[1]],\
freq[selected_fit_data[2]:selected_fit_data[3]])

#From the complex gamma value
cmplGamma_select = np.append(cmplGamma[selected_fit_data[0]:
    selected_fit_data[1]],\ cmplGamma[selected_fit_data[2]:
    selected_fit_data[3]])

#least square function set up
res_wrapped = least_squares(f_wrap, (5, 300, 0.0015), args=(freq_select,
    cmplGamma_select),\
```

```
    xtol=1e-11, ftol=1e-11, loss = 'cauchy',max_nfev=3000, bounds
        =([0,5000]))

#Print the fitted params
print('Fitting results:')
print('fitted R_s=', res_wrapped.x[0])
print('fitted R_L=',res_wrapped.x[1])
print('fitted C=',res_wrapped.x[2])

#print(res_wrapped)

#Use the fitted parameter to calculate the physical value
fit_resSers = np.array(res_wrapped.x[0]) #x[0]
fit_resLeak = np.array(res_wrapped.x[1]) #x[1]
fit_capElcd = np.array(res_wrapped.x[2]) #x[2]

jOmega = 1j*2*np.pi*np.array(freq)*1e-9
jOmegaCapElcd = jOmega*fit_capElcd

cmpl_imp_load = 50*(1+cmplGamma)/(1-cmplGamma)

#Calculate the fitted load, gamma and admittnace using the fitted
    parameter
ft_cmpl_re_im_load = fit_resSers+ 1/(fit_resLeak**(-1) + jOmegaCapElcd)
ft_cmpl_gamma = (ft_cmpl_re_im_load-50)/(ft_cmpl_re_im_load+50)
ft_cmplAdm = 1/(cmpl_imp_load-fit_resSers) - 1/fit_resLeak - jOmegaCapElcd

#The following calculation assume the complex Characteristic Impedance (
    cmpl_chrt_Imp) is real = 50 ohm
cmpl_chrt_Imp = 50
Pwr_input = 1

Vol_Load_RMS = np.sqrt(Pwr_input*cmpl_chrt_Imp/(1-cmplGamma**2))*(1+
    cmplGamma)
Crt_Load_RMS = Vol_Load_RMS/cmpl_imp_load
```

```
    Crt_Res_Sers_RMS = Crt_Load_RMS
    Vol_Res_Sers_RMS = Crt_Res_Sers_RMS * fit_resSers

    Vol_Adm_RMS = Vol_Load_RMS - Vol_Res_Sers_RMS
    Vol_Res_Leak_RMS = Vol_Adm_RMS
    Crt_Adm_RMS = Vol_Adm_RMS*ft_cmplAdm
    Crt_Res_Leak_RMS = Vol_Res_Leak_RMS/fit_resLeak

    Pwr_refletion_from_data = cmplGamma.real**2 + cmplGamma.imag**2
    Pwr_Res_Sers = Vol_Res_Sers_RMS*np.conj(Crt_Res_Sers_RMS)
    Pwr_Res_Leak = Vol_Res_Leak_RMS*np.conj(Crt_Res_Leak_RMS)
    Pwr_Adm = Vol_Adm_RMS*np.conj(Crt_Adm_RMS)

    return Pwr_Adm, freq

fitted R_s= 17.939761039741587
fitted R_L= 1640.9995649398836
fitted C= 0.0006451710805663596
```

Appendix III: Additional OMR theory notes

Hamiltonian

As opposed to cavity optomechanics, where the wavevectors of the propagating modes are typically not taken into account for analysis, the circuit optomechanics leverage the phase-matching condition (PMC) of the traveling modes. The PMC is crucial in our analysis because only by satisfying the momentum conservation between the modes ensures the optomechanical coupling of optical and mechanical modes. First, we explore the PMC is an optomechanical waveguide and how it can be useful and then in a ring type cavity to show that one can choose the PMC such that the functionality of the optomechanical device can be selected.

The model is essentially a multi-modal optomechanical coupling interactions. The bare Hamiltonian of such system can be expressed as

$$\frac{H_0}{\hbar} = \omega_0 \hat{a_0}^\dagger \hat{a_0} + \omega_1 \hat{a_1}^\dagger \hat{a_1} + \Omega \hat{b}^\dagger \hat{b} \tag{A.16}$$

where $\hat{a}_i$ ($\hat{a}_i^\dagger$) and $\hat{b}$ ($\hat{b}^\dagger$) are the annihilation (creation) operator of the i-th photonic and phononic mode with frequency ω_i and Ω. The interaction Hamiltonian H_I of the optomechanical ring consist of a well-known cavity optomechanical interaction ($i = j$) and a three mode mixing interaction ($i \neq j$). This multimode interaction Hamiltonian by optical mode linearization $\hat{a}_i \rightarrow \bar{\alpha}_i + \hat{a}_i$ can be written as

$$\begin{aligned}\frac{H_I}{\hbar} &= g_0\hat{a_0}^\dagger\hat{a_1}(\hat{b}+\hat{b}^\dagger) + g_1\hat{a_1}^\dagger\hat{a_0}(\hat{b}+\hat{b}^\dagger) \\ &= g_0(\bar{\alpha}_0+\hat{a_0})^\dagger(\bar{\alpha}_1+\hat{a_1})(\hat{b}+\hat{b}^\dagger) + g_1(\bar{\alpha}_1+\hat{a_1})^\dagger(\bar{\alpha}_0+\hat{a_0})(\hat{b}+\hat{b}^\dagger) \\ &\simeq g\bar{\alpha}_1(\hat{a_0}^\dagger\hat{b}+\hat{a_0}\hat{b}) + g\alpha_0(\hat{a_1}^\dagger\hat{b}+\hat{a_1}\hat{b}) + c.c., \end{aligned} \tag{A.17}$$

where the vacuum optomechanical coupling coefficient $g_0 = g_1 = g$ is a combination effect from PMC, photoelastic effect, and moving boundary effect. This will be discussed in detail at a later section. And $\bar{\alpha}_i$ is the classical optical amplitude of the i-th optical mode.

Therefore, the full Hamiltonian is given by

$$\frac{H}{\hbar} = \omega_0\hat{a_0}^\dagger\hat{a_0} + \omega_1\hat{a_1}^\dagger\hat{a_1} + \Omega\hat{b}^\dagger\hat{b} + [g\bar{\alpha}_1(\hat{a_0}^\dagger\hat{b}+\hat{a_0}\hat{b}) + g\bar{\alpha}_0(\hat{a_1}^\dagger\hat{b}+\hat{a_1}\hat{b}) + c.c.] \tag{A.18}$$

So far, the expressions of the multi-modal optomechanical coupling are agnostic. Without the loss of generality, we now consider traveling optical and mechanical modes in a straight optomechanical waveguide [57]. The translation symmetry of the optomechanical waveguide ensures the bosonic operators to be expressed as traveling modes using Bloch-Floquet expansion [73, 74]

$$\bar{\alpha}_i(z,t) = A_i\ \exp(ik_iz - i\omega_it) \tag{A.19a}$$

$$\hat{a}_i(z,t) = \hat{a}_i\ \exp(ik_iz - i\omega_it) \tag{A.19b}$$

$$\hat{b}(z,t) = \hat{b}\ \exp(iqz - i\Omega t), \tag{A.19c}$$

where k_i and q are the wavevector of the i-th photonic and phononic modes that are traveling in z direction. Using equation (A.19a)-(A.19c), and in the case of only considering $\hat{a}_1 \to \bar{\alpha}_1$, (A.17) becomes

$$\frac{H_I}{\hbar}|_{\hat{a}_1\to\bar{\alpha}_1} = g|\bar{\alpha}_1|(\hat{a_0}^\dagger\hat{b}e^{-i(\Omega-\Delta)t+i(q-\delta)z} + \hat{a_0}\hat{b}e^{i(\Omega+\Delta)t+i(-q-\delta)z}) + c.c.,$$

where $\Delta = \omega_0 - \omega_1$, $\delta = k_0 - k_1$. This is essentially the well-known intermodal Brillouin scattering process, where two optical modes (ω_0, k_0) and (ω_1, k_1) exchange energy via an acoustic mode (Ω, q) when the PMC is satisfied. Interestingly, when we choose a $\Delta = \Omega = \omega_0 - \omega_1$ and $\delta = +q = k_0 - k_1$, a beam-splitter like Hamiltonian can be realized as

$$\frac{H_I}{\hbar}|_{\mathrm{bs}} = g|\bar{\alpha}_1|(\hat{a_0}^\dagger\hat{b} + \hat{a_0}\hat{b}^\dagger), \tag{A.20}$$

where $G_i = g|\alpha_i|$ is the pumped enhanced coupling coefficient. This form effectively enables the state-swapping between $\hat{a_0}$ and $\hat{b}$, which is used in quantum transduction. Conversely, if we choose the condition of $\Delta = -\Omega = \omega_0 - \omega_1$ and $\delta = -q = k_0 - k_1$, a two-mode squeezing like Hamiltonian can be expressed as

$$\frac{H_I}{\hbar}|_{\mathrm{ts}} = g|\bar{\alpha}_1|(\hat{a_0}^\dagger\hat{b}^\dagger + \hat{a_0}\hat{b}), \tag{A.21}$$

which is used for entanglement generation between $\hat{a_0}$ and $\hat{b}$. In other words, the additional directional degree of freedom enables us to perform either quantum transduction or entanglement generation by selecting different pump directions. For a ring-type cavity, such as the optomechanical ring resonator, the same interaction Hamiltonian can be achieved simply by replacing the Cartesian coordinate displacement variables (x, y, z) with cylindrical coordinates (r, θ), and substituting the wavevector (k, q) with the azimuthal mode numbers of optical and acoustic resonant modes (m, l).

Heisenberg-Langevin equation of motion

We simplify the equation-of-motion (EOM) analysis by ignoring the second-order perturbation of the Hamiltonian (i.e., the $\hat{a}_i\hat{a}_j$ terms). We can express the simplified EOM as

$$\dot{\hat{b}} = -(i\Omega + \frac{\kappa_b}{2})\hat{b} - iG_1\hat{a_0} - iG_0\hat{a_1} + \sqrt{\kappa_{e,b}}\hat{b}_{\mathrm{e}} + \sqrt{\kappa_{i,b}}\hat{b}_{\mathrm{i}} \tag{A.22a}$$

$$\dot{\hat{a}}_0 = -(i\omega_0 + \frac{\kappa_0}{2})\hat{a}_0 - iG_1\hat{b} + \sqrt{\kappa_{e,0}}\hat{a}_{\mathrm{e},0} + \sqrt{\kappa_{i,0}}\hat{a}_{\mathrm{i},0} \tag{A.22b}$$

$$\dot{\hat{a}}_1 = -(i\omega_1 + \frac{\kappa_1}{2})\hat{a}_1 - iG_0\hat{b} + \sqrt{\kappa_{e,1}}\hat{a}_{\mathrm{e},1} + \sqrt{\kappa_{i,1}}\hat{a}_{\mathrm{i},1}. \tag{A.22c}$$

where $\kappa_{(b,0,1)} = \kappa_{e,(b,0,1)} + \kappa_{i,(b,0,1)}$ is the total resonator linewidth of the OMR. We can further analyze the HOM with input-output theory to understand the system dynamics. The EOM can be rewritten as a matrix form

$$\dot{\hat{\mathbf{s}}} = A\hat{\mathbf{s}} + B\hat{\mathbf{s}}_{\text{in}} \tag{A.23a}$$

$$\hat{\mathbf{s}}_{\text{out}} = C\hat{\mathbf{s}} + D\hat{\mathbf{s}}_{\text{in}}, \tag{A.23b}$$

where $\hat{\mathbf{s}} = [\hat{b},\ \hat{a}_0,\ \hat{a}_1]^T$, $\hat{\mathbf{s}}_{\text{in}} = [\hat{b}_e,\ \hat{b}_i,\ \hat{a}_{e,0},\ \hat{a}_{i,0},\ \hat{a}_{e,1},\ \hat{a}_{i,1}]^T$, and $\hat{\mathbf{s}}_{\text{out}} = [\hat{b}_{\text{out}},\ \hat{a}_{\text{out},0},\ \hat{a}_{\text{out},1}]^T$. And the full-form of the transfer matrix can be written as

$$A = \begin{pmatrix} -(i\Omega + \frac{\kappa_b}{2}) & -iG_1 & -iG_0 \\ -iG_1 & -(i\omega_0 + \frac{\kappa_0}{2}) & 0 \\ -iG_0 & 0 & -(i\omega_1 + \frac{\kappa_1}{2}) \end{pmatrix},$$

$$B = \begin{pmatrix} \sqrt{\kappa_{e,b}} & \sqrt{\kappa_{i,b}} & 0 & 0 & 0 & 0 \\ 0 & 0 & \sqrt{\kappa_{e,0}} & \sqrt{\kappa_{i,0}} & 0 & 0 \\ 0 & 0 & 0 & 0 & \sqrt{\kappa_{e,1}} & \sqrt{\kappa_{i,1}} \end{pmatrix},$$

$$C = \begin{pmatrix} \sqrt{\kappa_{e,b}} & 0 & 0 \\ 0 & \sqrt{\kappa_{e,0}} & 0 \\ 0 & 0 & \sqrt{\kappa_{e,1}} \end{pmatrix},$$

$$D = \begin{pmatrix} -1 & 0 & 0 & 0 & 0 & 0 \\ 0 & 0 & -1 & 0 & 0 & 0 \\ 0 & 0 & 0 & 0 & -1 & 0 \end{pmatrix}.$$

Transduction efficiency

Using the input-output formalism, the transduction efficiency can be calculated by the scattering matrix

$$\hat{s}_{\text{out}} = \mathbf{S}\hat{s}_{\text{in}}, \tag{A.24}$$

and one can solve $\mathbf{S}$ by using the A, B, C, and D matrix. The solution of the scattering matrix would be

$$\mathbf{S} = C(-i\boldsymbol{\omega} - A)^{-1}B + D, \tag{A.25}$$

where

$$\boldsymbol{\omega} = \begin{pmatrix} \Omega & 0 & 0 \\ 0 & \omega_{0,\text{in}} & 0 \\ 0 & 0 & \omega_{1,\text{in}} \end{pmatrix}$$

is the driving frequency of the optical modes from the bus waveguide. In the case of counter-propagating acoustic wave TE_0 to TE_1 anti-Stokes scattering, as presented in the main text, only the TE_0 mode and the acoustic mode are driven in the OMR, and we can consider the pump-enhanced coupling coefficient $G_0 \gg G_1$. We then plug this into Eq. A.25 and solve for $\mathbf{S}$. The transduction process here converts a microwave mode ($\hat{b}$) into an TE_1 mode output ($\hat{a}_1$), so we can rewrite Eq. A.24 as

$$\begin{pmatrix} \hat{b}_{\text{out}} \\ \hat{a}_{1,\text{out}} \end{pmatrix} = \begin{pmatrix} \frac{\kappa_{e,b}(-i\delta_1-\kappa_1/2)}{(i\delta_1+\kappa_1/2)\kappa_b/2-G_0^2} - 1 & \frac{G_0\sqrt{\kappa_{e,1}\kappa_{e,b}}}{(i\delta_1+\kappa_1/2)\kappa_b/2-G_0^2} \\ \frac{G_0\sqrt{\kappa_{e,1}\kappa_{e,b}}}{(i\delta_1+\kappa_1/2)\kappa_b/2-G_0^2} & -\frac{\kappa_{e,1}\kappa_b/2}{(i\delta_1+\kappa_1/2)\kappa_b/2-G_0^2} - 1 \end{pmatrix} \begin{pmatrix} \hat{b}_{\text{e}} \\ \hat{a}_{e,1} \end{pmatrix}, \tag{A.26}$$

where the optical detuning $\delta_1 = (\omega_{1,\text{in}} - \omega_1)$, and the diagonal elements of the scattering matrix $\mathbf{S}$ are the microwave-optical conversion efficiency. At $\hat{a}_{1,\text{in}} = 0$ and zero optical detuning ($\delta_1 = 0$), the extrinsic microwave-to-optical conversion efficiency

$$\eta_{\text{ext}} = |\frac{\hat{a}_{1,\text{out}}}{\hat{b}_{\text{in}}}|^2 = |\frac{G_0\sqrt{\kappa_{e1}\kappa_{eb}}}{\kappa_1\kappa_b/4 - G_0^2}|^2. \tag{A.27}$$

Added noise

In our system, the input-referred added noise n_{add} at the optical output $\hat{a}_{1,\text{out}}$ mainly has two noise sources: 1, the $\hat{a}_{0,\text{in}}$ pumping that is used to enhance coupling rate G_0. This $\hat{a}_0$ pump generates a thermal bath that contributes to the optical added noise $n_{e,0}$. And, 2, the RF drive at the IDT that also contribute to this heat bath which induces thermal noise $n_{i,b}$ that contributes to the output added noise. We only take into account $n_{i,b}$ since the thermal bath occupancy at optical frequency is negligible ($n_{e,0} \simeq 0$). The added noise is therefore written as

$$n_{\text{add}} = \frac{\kappa_{i,b}}{\kappa_{e,b}} n_{i,b} \tag{A.28}$$

where is the resonator thermal occupancy.

Appendix IV: COMSOL simulations

The Goal of This Note

There are several things to calculate before actually move on to design the device, The first thing we have to confirm is the mode overlap of the acoustic and optical modes.

- Calculate the K-vector(K_{op}) for the optical modes with current acoustic WG design.
- Calculate the K-vector(K_{ac}) for the acoustic mode for the current acoustic WG design.
- Find the optical mode that matches the K_{op} and K_{ac}.
  - In our case the acoustic wave is symmetric(x-y plane), so we need either two more symmetric optical modes to make sure in the mode integral is not zero.
- Note: $K_{op} = \frac{2\pi}{\lambda_{op}/n} = 13.07(\mu m^{-1})$ and $K_{ac} = \frac{2\pi}{\lambda_{ac}} = 9.24(\mu m^{-1})$
  - n: In BGaP suspended film, the reflective index n of both BGaP and GaP used in simulation is 3.20346.
  - λ_{op}: We picked the highest transmission wavelength in suspended GC/RR measurements, which is 1540nm.
  - λ_{ac}: With the current IDT design(May 24th 2022), the period(λ_{ac}) is 0.68nm. $V_{Fast-ac} = 4246, V_{Slow-ac} = 3009(m^{-1})$

The OMR Design Process

Here we investigate the OMR for intermodal scattering purpose and elaborate the design process. The design process is listed as following:

- Select the corresponding TE modes that satisfy the phase matching condition:

  $$k_1 - k_2 = \Delta k = K_a.$$

  In this case, we use TE0 and TE5 modes.

- Use COMSOL to find the optical wavevector of each mode and calculate the ΔK.

- Use a directional coupler to couple out the TE_5 mode such that the TE_0 mode is kept inside the bus waveguide

- Find the corresponding effective mode index with different waveguide width. i.e. find the effective mode index for TE_5 in the bus waveguide, and that of TE_0 in coupling waveguide. Match the both mode index such that the TE_5 and *only* TE_5 can be coupled to the coupling waveguide. The TE_5 that couples to the thin waveguide is effectively TE_0 in the coupling waveguide.

- Then we can proceed to use COMSOL to simulate a hybrid structure with both bus and coupling waveguide to find the effective mode index that has a π phase shift and record the Δn_{eff}.

- The coupling length can be calculated using the Δn_{eff} by the equation:

  $$L_{coup} = \frac{\lambda_o/2}{\Delta n_{eff}}(\mu m)$$

  i.e. $\frac{1.55/2}{0.03} \sim 25\mu m$. If the Δn_{eff} is too small, we can decrease the coupling gap to increase the If the Δn_{eff}.

- After getting the coupling length, we can use Lumerical to simulate the time domain coupling situations.

Below extract the code to calculate the FSR for different ring diameters from the jupyter notebook:

```
n_g = 3
c = 3e8 #m/s
fsr_o = c/(n_g*ring_dias*np.pi*1e-6) #Hz

print("Ring diameters=" + str(ring_dias) + ’um’)
print("Optical FSR=" + str(fsr_o/1e9) + ’GHz’)

#convert to nm at 1550nm region
telecom_freq = 3e8/1550*1e9 #Hz
freq_o_hz = telecom_freq + fsr_o
freq_nm = 3e8/freq_o_hz*1e9

fsr_nm = abs(freq_nm - 1550)

print("Optical FSR=" + str(fsr_nm) + ’nm’)
```

output:

```
Acoustic speed_1=2734.68m/s
Acoustic speed_2=2014.35m/s

Ring diameters=[100 150 200 250]um
Acoustic FSR=[8.70 5.80 4.35 3.48]MHz

Ring diameters=[100 150 200 250]um
Optical FSR=[318.30988618 212.20659079 159.15494309 127.32395447]GHz
Optical FSR=[2.54494625 1.69755991 1.27351862 1.01898234]nm
```

Some of the ideas that we can use for the OMR, eventually we choose the intermode scattering as our application.

- Inter-mode scattering of TE_0 to TE_2 for acoustic waveguide width = 1.010um.
- Optical isolator
  - The problem with optical isolator is that the optical Q of our device is not hight enough to resolve the two modes inside the OMR, $Q_{op} > 20\text{K}$. And the phase matching is difficult, e.g. from TM_0 to TM_{01} acoustic waves ~ 800MHz.
- Out-of-plane frequency shifter
  - We can just observe the light scattering out from the rings. If the efficiency is high then we demonstrate the acousto-optic effect is high in a co-confined resonator.

COMSOL Simulation Note

To design a proper mode overlap between optical and acoustic modes, we use COMSOL ver5.5 to simulate the mode shapes, strength, multiplication of the O/A modes. And the details are as the follows:

Optical mode simulations

We first use a 2D model of the BGaP waveguide to find the optical eigenmodes in a given waveguide geometry. Specifically, we can obtain the k-vector of the desire mode and then use the k-vector as an input in 3D model to compute the optical mode shape distribution in 3D. Otherwise, in 3D simulation we will not be able to find the k-vector.

Find the k-vector in COMSOL 2D simulation:

1. Create a 2D model in COMSOL for the designated structure.
2. In `Physics`, choose `Electromagnetic Waves, Frequency Domain` for eigenmode simulations.

3. In `Mesh`, build the proper mesh resolutions.

4. In `Study`, choose `Mode Analysis`, which will find the TE/TM modes of the cross section of the WG.

5. In `Mode Analysis`, `Transform`, select either `Effective Mode Index` or `Out-of-Plane Wave Number` as desire.

6. Compute the simulation and note the desire k-vector for later use.

Find the mode overlap in COMSOL 3D simulation:

1. Create a 3D model in COMSOL for the designated structure.

2. In `Physics`, choose `Electromagnetic Waves, Beam Envelopes` for optical mode simulation.

    - Click on `Electromagnetic Waves, Beam Envelopes` and select `Unidirectional` for number of directions. Also change the `Wave vector` direction in the propagation direction as *ewbe.beta_1*.

    - Create `Port 1` for mode excitation. Turn the `Wave excitation at this port` to on and change the `Type of port` to `Numeric`. Select the input surfaces on the model.

    - Create `Port 2`. Turn the `Wave excitation at this port` to off and change the `Type of port` to `Numeric`. Select the output surfaces on the model.

3. In `Mesh`, build the proper mesh resolutions.

4. In `Study`, create `Boundary Mode Analysis`. In `Transform` choose wavevector. Specify the port as **1** and input frequency as 194.3 THz(1540nm).

5. Duplicate the first BMA and specify the port as **2**. Search for modes around **k** Mrad/m for TE0 mode.

6. The **k** in last step is the wavevector calculated from the 2D simulation. E.g. k=10.73 is TE0 mode.

7. In `Study`, create `Frequency Domain` as step 3 for the optical mode study and specify the frequency.
8. Compute the simulation should generate the corresponding modes*.

*: The solver configurations should consist of `Eigensolver1` and `Eigensolver2` for the two BMA and `Stationary Solver 1` for frequency domain.

Appendix V: Layout design with python package: omgds.py

Overview

The link for this program can be found on GitHub (omgds.py).

The optomechanical graphical design system (omgds) is a Python package that provides a simple and intuitive way to optimize integrated optomechanical design layouts. With omgds_py, you can easily create both integrated photonic and electronic circuits, and create an array of different designs to optimize the performance of your optomechanical circuits. This package is based on the GDSFactory and gdshelpers package, which are Python packages that provide ways to create GDSII files for use in integrated photonic devices.

Installation

To download the omgds_py codes, simply run the following command:

```
git clone https://github.com/itungc/omgds_py.git
```

The current version of the omgds_py only supports Python 3.10 or above. It is recommended to use a virtual environment to run the program. To create a virtual environment, run the following command using conda:

```
conda create —n omgds_env python=3.10
```

After creating the virtual environment, activate the environment by running the following command:

```
conda activate omgds_env
```

Then, install the required packages by running the following command:

```
pip install -r requirements.txt
```

Usage

After installing the necessary packages, the user can run the program by running the main.py file in the omgds_py directory.

Here's a quick example to get you started:

For Mac users, the user should run the following command in the omgds_py directory to run the program:

```
/Users/[user_name]/opt/anaconda3/envs/[your_env_name]/bin/python ./
    omgds_py/main.py
```

For Windows users, the user should run the following command to run the program:

```
C:/Users/[user_name]/AppData/Local/anaconda3/envs/[your_env_name]/
    python.exe ./omgds_py/main.py
```

Upon running the program, the user will be prompted to enable the GDSFactory (GF) package:

```
Enable GDSFactory? (input 'n' to use gdshelper) (y/n):
```

Input `yes` or `y` to enable the GDSFactory package. Input `no` or `n` will default to the gdshelpers package.

Then, it will prompt the user to either save or show the cells.

Input `show` to generate a single PCell and it will show the single cell in KLayout.

```
Input(save/show, case sensitive):show
```

Input `save` to generate PCell arrays and save it in the gds_files directory.

```
Input(save/show, case sensitive):save
```

The program is structured as the following:

```
.
omgds_py
__init__.py
main.py
/generators
/subcomponents
/gds_files
/test_paramters
```

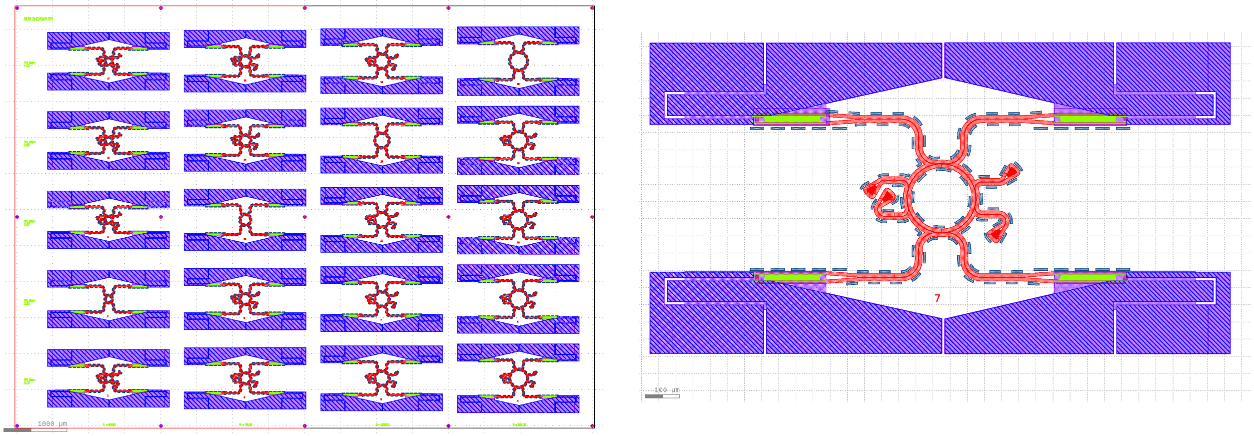

Figure A.3: A generated design example. This is the OMR on BGaP layout generated using the omgds.

Directory Structure

main.py

This is the main function that lays out the cells. The user should change the scan_parameters in this `main.py` function. This is the highest level of the omgds design process. Input the scan parameters and the program will generate the cells based on the scan parameters. The user can also input the save or show command to save the cells or show the cells.

generators

This directory contains all the generators for different chips. Each chip has its own generator file. The user can add their own generator file to this directory. The user should use each subcomponent to generate a single cell. After the subcomponents are generated, the user can use translation function to move the subcomponents around to build their own cell.

subcomponents

This directory contains the basic components that are used in the generator. The user will have the highest degree of freedom in the subcomponents, including changing the metal pad sizes, the waveguide sizes, interdigital transducer (IDT) pitches.

Contributing

We welcome contributions from the community! If you have any ideas, bug reports, or feature requests, please open an issue on our GitHub repository or submit a pull request.

License

omgds_py is licensed under the MIT License. See the LICENSE file for more information.

References

The devices in the following papers were created using the omgds_py package:

1. Chen, IT., Li, B., Lee, S. et al. Optomechanical ring resonator for efficient microwave-optical frequency conversion. Nat Commun 14, 7594 (2023). https://doi.org/10.1038/s41467-023-43393-x
2. N. S. Yama*, I. T. Chen*, et al. "Silicon-Lattice-Matched Boron-Doped Gallium Phosphide: A Scalable Acousto-Optic Platform", Advanced Materials, doi.org/10.1002/adma.202305434 (2023) *equal contribution authors

Appendix VI: Laser and VNA control software

This software is written in python, and the can simultaneously the laser (Santec TSL-570) and VNA (Agilent). It also acquires the optical output from two photodetectors, so one can monitor the optical transmission from two separate port at the same time. This software is used frequently when performing optical measurements for the OMR.

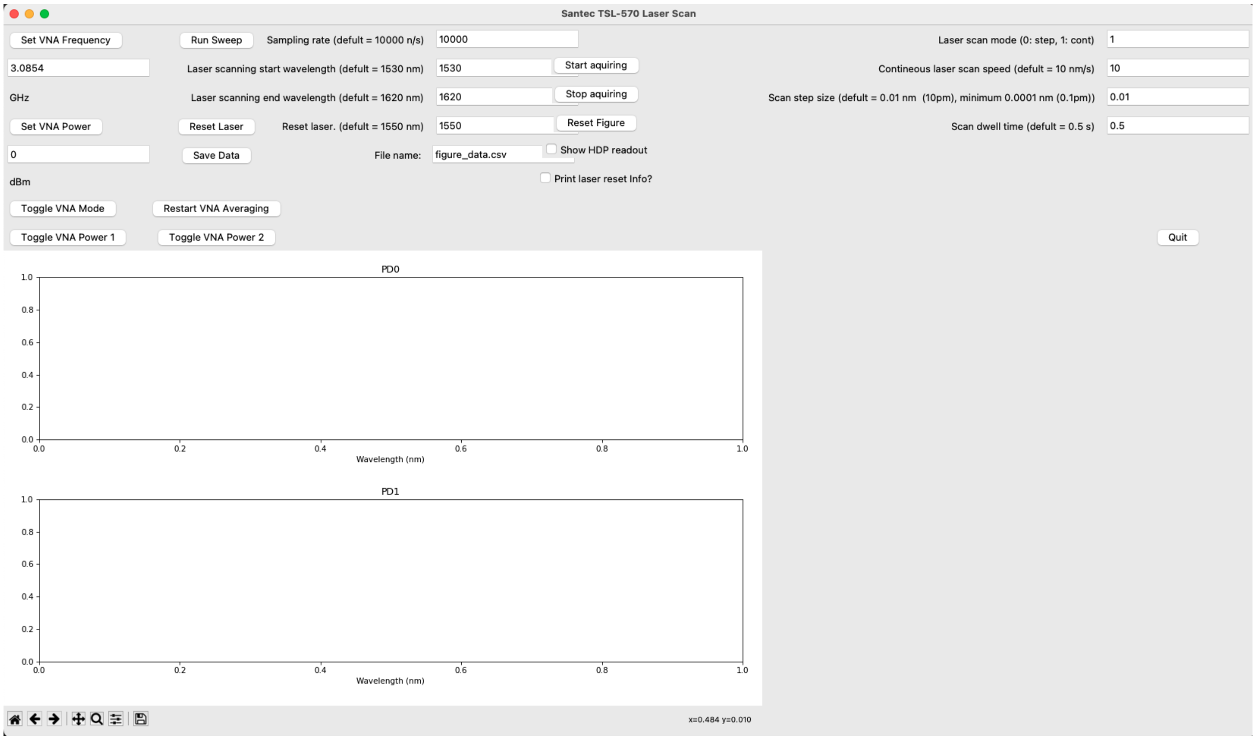
Santec TSL-570 Laser Scan

3.0854 GHz

0 dBm

Sampling rate (defult = 10000 n/s) 10000

Laser scanning start wavelength (defult = 1530 nm) 1530

Laser scanning end wavelength (defult = 1620 nm) 1620

Reset laser. (defult = 1550 nm) 1550

File name: figure_data.csv

☐ Show HDP readout

☐ Print laser reset Info?

Laser scan mode (0: step, 1: cont) 1

Contineous laser scan speed (defult = 10 nm/s) 10

Scan step size (defult = 0.01 nm (10pm), minimum 0.0001 nm (0.1pm)) 0.01

Scan dwell time (defult = 0.5 s) 0.5

x=0.484 y=0.010

Figure A.4: The VNA and laser control software.

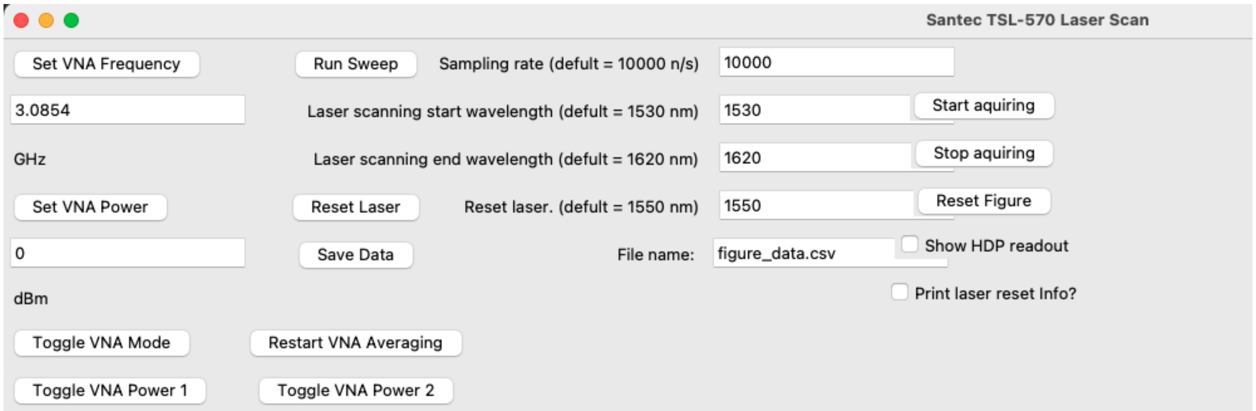

3.0854 GHz

0 dBm

Sampling rate (defult = 10000 n/s) 10000

Laser scanning start wavelength (defult = 1530 nm) 1530

Laser scanning end wavelength (defult = 1620 nm) 1620

Reset laser. (defult = 1550 nm) 1550

File name: figure_data.csv

☐ Show HDP readout

☐ Print laser reset Info?

Figure A.5: The VNA and laser software control panel

Listing 2: Python code

```python
import matplotlib.pyplot as plt
import tkinter as tk
from matplotlib.backends.backend_tkagg import FigureCanvasTkAgg
from matplotlib.figure import Figure
from matplotlib.animation import FuncAnimation
import random
from itertools import count
import nidaqmx
from nidaqmx.constants import (AcquisitionType, CountDirection, Edge,
    READ_ALL_AVAILABLE, TaskMode, TriggerType)
from nidaqmx.stream_readers import CounterReader
import numpy as np
import pprint
import pyvisa
import time
import threading
from matplotlib.backends.backend_tkagg import NavigationToolbar2Tk
import csv


def setup_laser_sweep(TLS_570, start_wl, end_wl, scan_mode, scan_speed = 10,
                      step_size = 0.1, dwell_time = 0.5, print_info = False):

    cmd = 'sour:pow:stat?'
    laser_on = TLS_570.query(cmd)

    cmd = 'trig:conf loop'
    TLS_570.write(cmd)

    # Laser scan start wavelength
    set_start_wl = ':wav:swe:star '+ str(start_wl)
    TLS_570.write(set_start_wl)

    # Laser scan end wavelength
    set_end_wl = ':wav:swe:stop '+ str(end_wl)
    TLS_570.write(set_end_wl)
```

```
    # Scan mode
    TLS_570.write(':wav:swe:mod ' + str(scan_mode))
    """
    0: Step sweep mode and One way
        Set the step width for step mode
        Set the step to 0.01 nm. (10 pm)
        :WAV:SWE:STEP 0.01
        :WAV:SWE:STEP 10pm
        :WAV:SWE:STEP 1.0E-11
    1: Continuous sweep mode and One way
        Only support 1,2,5,10,20,50,100,200 (nm/s)
        Set the contineous speed to 200 nm/s
        :WAV:SWE:SPE 200
    2: Step sweep mode and Two way
    3: Continuous sweep mode and Two way
    """
    if scan_mode == 0:
        # Step sweep mode and One way
        set_step_size = ':WAV:SWE:STEP ' + str(step_size)
        TLS_570.write(set_step_size)

        # Set dewelltime to 0.1s
        set_dwell_time = ':WAV:SWE:DWEL ' + str(dwell_time)
        TLS_570.write(set_dwell_time)

    if scan_mode == 1:
        # Continuous sweep mode and One way
        # Laser sweep speeds
        query_speed = ':wav:swe:spe?'
        current_speed = TLS_570.query(query_speed)
        set_speed = ':wav:swe:spe '+ str(scan_speed)
        TLS_570.write(set_speed)


    # Trigger set to stanby
    cmd = ':TRIG:INP:STAN 1'
    TLS_570.write(cmd)

    TLS_570.write(':WAV:SWE 0')


# Laser control functions
def run_pd01_sweep(laser_scan_speed, laser_scan_range, sampling_rate):

    # Acquire the user input
    scan_mode = float(scan_mode_entry.get())
    start_wl = float(start_wl_entry.get())
    end_wl = float(end_wl_entry.get())
    scan_speed= float(speed_entry.get())
    step_size = float(step_size_entry.get())
    dwell_time = float(dwell_time_entry.get())

    # Calculate the total number of samples to acquire
    if scan_mode == 0:
        # Calculate the total number of steps
        total_steps = int(laser_scan_range / step_size)
```

```
        # Calculate the total time of the scan
        total_time = total_steps * dwell_time

        # Calculate the total number of samples
        tot_sample_num = int(total_time * sampling_rate)
        samples_per_step = tot_sample_num // total_steps

    if scan_mode == 1:
        tot_sample_num = int(sampling_rate * (laser_scan_range / laser_scan_speed)
            )
    pd2 = []
    pd1 = []
    pd0 = []
    timeup = 2
    start_time = time.time()

    pp = pprint.PrettyPrinter(indent=4)

    with nidaqmx.Task() as task:
        if scan_mode == 0:
            task.ai_channels.add_ai_voltage_chan("Dev1/ai0")
            task.ai_channels.add_ai_voltage_chan("Dev1/ai1")
            task.ai_channels.add_ai_voltage_chan("Dev1/ai2")
            # Configure the task to start when a rising edge is detected on the
                trigger line
            task.triggers.start_trigger.cfg_dig_edge_start_trig("/Dev1/PFI1",
                trigger_edge=nidaqmx.constants.Edge.RISING)
            task.timing.cfg_samp_clk_timing(rate=sampling_rate, samps_per_chan=
                tot_sample_num)
            task.start()
            # Set the laser to generate output trigger when starting a wl sweep
            # Start the laser sweep
            time.sleep(2.5)
            TLS_570.write(’:WAV:SWE 1’)
            time.sleep(3.5)
            steps = np.linspace(start_wl, end_wl, int((end_wl - start_wl)/
                step_size))
            for step in steps:
                time.sleep(dwell_time)
                cmd = ’:TRIG:INP:SOFT’
                TLS_570.write(cmd)

            data = task.read(number_of_samples_per_channel=tot_sample_num, timeout
                =30)

            # Take the number of steps and average the data
            num_steps = int(len(data[0]) / samples_per_step)
            reshaped_pd0 = np.reshape(data[0], (num_steps, samples_per_step))
            reshaped_pd1 = np.reshape(data[1], (num_steps, samples_per_step))
            reshaped_pd2 = np.reshape(data[2], (num_steps, samples_per_step))
            pd0 = np.mean(reshaped_pd0, axis=1)
            pd1 = np.mean(reshaped_pd1, axis=1)
            pd2 = np.mean(reshaped_pd2, axis=1)

            task.stop()
```

```
        if scan_mode == 1:
            task.ai_channels.add_ai_voltage_chan("Dev1/ai0")
            task.ai_channels.add_ai_voltage_chan("Dev1/ai1")
            task.ai_channels.add_ai_voltage_chan("Dev1/ai2")
            # Configure the task to start when a rising edge is detected on the
                trigger line
            task.triggers.start_trigger.cfg_dig_edge_start_trig("/Dev1/PFI1",
                trigger_edge=nidaqmx.constants.Edge.RISING)
            task.timing.cfg_samp_clk_timing(rate=sampling_rate, samps_per_chan=
                tot_sample_num)
            task.start()
            # Set the laser to generate output trigger when starting a wl sweep
            # Start the laser sweep
            time.sleep(2.5)
            TLS_570.write(’:WAV:SWE 1’)
            time.sleep(2.5)
            cmd = ’:TRIG:INP:SOFT’
            TLS_570.write(cmd)
            # Aquiring the data
            data = task.read(number_of_samples_per_channel=tot_sample_num, timeout
                =30)

            # Save the read data to the corresponding variables
            pd0 = data[0]
            pd1 = data[1]
            pd2 = data[2]
            task.stop()

    end_time = time.time()

    time.sleep(3)
    setup_laser_sweep(TLS_570, start_wl, end_wl, scan_mode, scan_speed, step_size,
        dwell_time)
    time.sleep(1)

    return pd0, pd1, pd2

def run_sweep():
    # Acquire the user input
    scan_mode = float(scan_mode_entry.get())
    scan_speed = float(speed_entry.get())
    sampling_rate = float(rate_entry.get())
    start_wl = float(start_wl_entry.get())
    end_wl = float(end_wl_entry.get())
    step_size = float(step_size_entry.get())
    dwell_time = float(dwell_time_entry.get())

    # Calculate the laser scan range
    laser_scan_range = end_wl - start_wl

    setup_laser_sweep(TLS_570, start_wl, end_wl, scan_mode, scan_speed, step_size,
        dwell_time)

    # Update status label
    status_label.config(text="Scanning in progress...", fg="red")
```

```
    root.update()  # Force the GUI to update the label text

    # Start scanning the laser
    root.pd0, root.pd1, root.pd2 = run_pd01_sweep(scan_speed, laser_scan_range,
        sampling_rate)

    # Calculate the X-axis (wavelength based on scan mode)
    if scan_mode == 0: # Step scan mode
        # Calculate the total number of steps
        total_steps = int(laser_scan_range / step_size)

        # Calculate the total time of the scan
        total_time = total_steps * dwell_time

        # Calculate the total number of samples
        total_samples = int(total_time * sampling_rate)

        try:
            # Calculate the number of samples per step
            # Check if total_samples is a multiple of total_steps
            if total_samples % total_steps != 0:
                raise ValueError("Total samples is not a multiple of total steps")

            samples_per_step = total_samples // total_steps

            # Generate the x-axis values for each step
            root.x_values = np.arange(start_wl, end_wl, step_size)
            #root.x_values = np.repeat(np.arange(start_wl, end_wl, step_size),
                samples_per_step)
        except ValueError as e:
            print(f"Error: {e}")
            return  # Exit the function or handle the error as appropriate

        # Generate the x-axis values for each step
        #root.x_values = np.repeat(np.arange(start_wl, end_wl, step_size),
            samples_per_step)
        root.x_values = np.arange(start_wl, end_wl, step_size)

    if scan_mode == 1: # Continuous scan mode
        tot_sample_num = int(sampling_rate * (laser_scan_range / scan_speed))
        root.x_values = np.linspace(start_wl, end_wl, tot_sample_num)

    if show_dev2.get():
        ax1.cla()
        if scan_mode == 0:
            ax1.scatter(root.x_values, root.pd2, c = ’tab:green’)
        if scan_mode == 1:
            ax1.plot(root.x_values, root.pd2, c = ’tab:green’)
        ax1.set_title(’Dev2/ai2’)
        ax1.set_xlabel(’Wavelength (nm)’)

    if show_dev2.get() == False:
        ax1.cla()
        if scan_mode == 0:
            ax1.scatter(root.x_values, root.pd0)
        if scan_mode == 1:
```

```
            ax1.plot(root.x_values, root.pd0)
        ax1.set_title('PD0')
        ax1.set_xlabel('Wavelength (nm)')

    ax2.cla()
    if scan_mode == 0:
        ax2.scatter(root.x_values, root.pd1, c = 'tab:red')
    if scan_mode == 1:
        ax2.plot(root.x_values, root.pd1, c = 'tab:red')
    ax2.set_title('PD1')
    ax2.set_xlabel('Wavelength (nm)')

    ax1.grid()
    ax2.grid()
    fig.tight_layout()

    # Update status label
    status_label.config(text="Scanning completed", fg="green")
    root.update()  # Force the GUI to update the label text

    canvas.draw()
    toolbar.update()

    reset_laser()

def save_figure_data(wavelength_data, pd0_data, pd1_data, filename="figure_data.
    csv"):
    filename = tk.filedialog.asksaveasfilename(defaultextension=".csv",
        initialfile = filename)
    if filename:  # If a filename was selected
        with open(filename, 'w', newline='') as f:
            writer = csv.writer(f)
            writer.writerow(["Wavelength", "PD0", "PD1"])  # Write the headers
            for wavelength, pd0, pd1 in zip(wavelength_data, pd0_data, pd1_data):
                writer.writerow([wavelength, pd0, pd1])

def reset_laser():
    wl = float(reset_entry.get())
    cmd = ':wav:swe 0'
    TLS_570.write(cmd)
    cmd = ':wav ' + str(wl)
    TLS_570.write(cmd)

def quit_program():
    wl = float(reset_entry.get())
    cmd = ':wav:swe 0'
    TLS_570.write(cmd)
    cmd = ':wav ' + str(wl)
    TLS_570.write(cmd)
    root.destroy()

def run_laser_scan_thread():
    threading.Thread(target=run_sweep).start()

def animate(i):
    global x_vals
```

```
    global y_vals
    global y_vals2
    global y_vals3  # For "Dev2/ai2"
    global show_dev2  # For toggling "Dev2/ai2"
    x_vals.append(next(index))
    with nidaqmx.Task() as task:
        task.ai_channels.add_ai_voltage_chan("Dev1/ai0")
        in_stream = task.in_stream
        task.ai_channels.add_ai_voltage_chan("Dev1/ai1")
        task.ai_channels.add_ai_voltage_chan("Dev1/ai2")
        data2 = task.read(number_of_samples_per_channel=1)
        y_vals.append(data2[0])
        y_vals2.append(data2[1])
        y_vals3.append(data2[2])

    x_vals = x_vals[-300:]
    y_vals = y_vals[-300:]
    y_vals2 = y_vals2[-300:]
    y_vals3 = y_vals3[-300:]

    # If show_dev2 is True, plot y_vals3 in a new subplot
    if show_dev2.get():
        ax1.cla()
        ax1.plot(x_vals, y_vals3, c = 'tab:green')
        ax1.set_title('Dev2/ai2')
        ax1.set_xlabel('Samples')
    if show_dev2.get() == False:
        ax1.cla()
        ax1.plot(x_vals, y_vals)
        ax1.set_title('PD0')
        ax1.set_xlabel('Samples')

    ax2.cla()
    ax2.plot(x_vals, y_vals2, c = 'tab:red')
    ax2.set_title('PD1')
    ax2.set_xlabel('Samples')

    ax1.grid()
    ax2.grid()

    fig.tight_layout()

def start_animation():
    global ani
    ani = FuncAnimation(fig, animate, interval=50, cache_frame_data=False)
    canvas.draw()

def stop_animation():
    global ani
    if ani is not None:
        ani.event_source.stop()
        ani = None

def reset_figure():
    global ani, x_vals, y_vals, y_vals2, y_vals3
    if ani is not None:
```

```
        ani.event_source.stop()
        ani = None
    x_vals.clear()
    y_vals.clear()
    y_vals2.clear()
    y_vals3.clear()
    ax1.clear()
    ax2.clear()
    canvas.draw()
    ax1.set_title(’PD0’)
    ax2.set_title(’PD1’)

# VNA control functions
def VNA_Power_on1():
    VNA.write(’SOUR:POW1:MODE ON’)

def VNA_Power_off1():
    VNA.write(’SOUR:POW1:MODE OFF’)

def VNA_Power_on2():
    VNA.write(’SOUR:POW2:MODE ON’)

def VNA_Power_off2():
    VNA.write(’SOUR:POW2:MODE OFF’)

def toggle_VNA_power1():
    # If the power is on, turn it off
    if VNA_power_status1.get():
        VNA_power_status1.set(False)
        VNA_Power_off1()  # Call the function to turn off the VNA power
        VNA_power_on_button1.config(text="VNA Power (1) is OFF", fg="red")
    # If the power is off, turn it on
    else:
        VNA_power_status1.set(True)
        VNA_Power_on1()  # Call the function to turn on the VNA power
        VNA_power_on_button1.config(text="VNA Power (1) is ON", fg="green")

def toggle_VNA_power2():
    # If the power is on, turn it off
    if VNA_power_status2.get():
        VNA_power_status2.set(False)
        VNA_Power_off2()  # Call the function to turn off the VNA power
        VNA_power_on_button2.config(text="VNA Power (2) is OFF", fg="red")
    # If the power is off, turn it on
    else:
        VNA_power_status2.set(True)
        VNA_Power_on2()  # Call the function to turn on the VNA power
        VNA_power_on_button2.config(text="VNA Power (2) is ON", fg="green")

def VNA_CW_mode():
    VNA.write(’SENS:SWEEP:TYPE CW’)

def VNA_LIN_mode():
    VNA.write(’SENS:SWEEP:TYPE LIN’)

def toggle_VNA_mode():
```

```
    # If in CW, turn to Lin
    if VNA_mode_status.get():
        VNA_mode_status.set(False)
        VNA_LIN_mode()  # Call the function to turn off the VNA power
        VNA_CW_mode_button.config(text="VNA in LIN mode", fg="black")
    # If the LIN, turn CW
    else:
        VNA_mode_status.set(True)
        VNA_CW_mode()  # Call the function to turn on the VNA power
        VNA_CW_mode_button.config(text="VNA in CW mode", fg="blue")

def VNA_set_CW_freq():
    VNA_freq = float(VNA_freq_entry.get())
    commend = 'SENS:FREQ ' + str(VNA_freq) + ' GHZ'
    VNA.write(commend)

def VNA_set_power():
    VNA_pow = float(VNA_pow_entry.get())
    commend = 'SOUR:POW2  ' + str(VNA_pow)
    VNA.write(commend)


if __name__ == "__main__":

    x_vals = []
    y_vals = []
    y_vals2 = []
    y_vals3 = []

    index = count()

    rm = pyvisa.ResourceManager()
    print(rm.list_resources())

    TLS_570 = rm.open_resource('GPIB0::1::INSTR')
    print(TLS_570.query('*IDN?'))

    # Set the laser to generate output trigger when starting a wl sweep
    TLS_570.write('trig:outp 2')

    VNA = rm.open_resource('TCPIP0::A-N5230C-0117::inst0::INSTR')

    root = tk.Tk()
    root.title("Santec TSL-570 Laser Scan")
    # Configure column 1 to have a minimum size and prevent it from stretching
    root.grid_columnconfigure(0, minsize=10, weight=0)

    # Setting the laser scan parameters
    # Create an Entry widget for each parameter
    scan_mode_entry = tk.Entry(root)
    start_wl_entry = tk.Entry(root)
    end_wl_entry = tk.Entry(root)
    speed_entry = tk.Entry(root)
    rate_entry = tk.Entry(root)
    reset_entry = tk.Entry(root)
    step_size_entry = tk.Entry(root)
```

```
dwell_time_entry = tk.Entry(root)
filename_entry = tk.Entry(root)

# GUI layout
# Column 0
tk.Label(root, text = "Sampling rate (defult = 10000 n/s)").grid(row=0, padx
    =5, pady=5, sticky=tk.E)
tk.Label(root, text = "Laser scanning start wavelength (defult = 1530 nm)").
    grid(row=1, padx=5, pady=5, sticky=tk.E)
tk.Label(root, text = "Laser scanning end wavelength (defult = 1620 nm)").grid
    (row=2, padx=5, pady=5, sticky=tk.E)
tk.Label(root, text = "Reset laser. (defult = 1550 nm)").grid(row=3, padx=5,
    pady=5, sticky=tk.E)
tk.Label(root, text = "File name: ").grid(row=4, padx=5, pady=5, sticky=tk.E)

# Column 1
rate_entry.grid(row=0, column=1, padx=5, pady=5, sticky=tk.W)
start_wl_entry.grid(row=1, column=1, padx=5, pady=5, sticky=tk.W)
end_wl_entry.grid(row=2, column=1, padx=5, pady=5, sticky=tk.W)
reset_entry.grid(row=3, column=1, padx=5, pady=5, sticky=tk.W)
filename_entry.grid(row=4, column=1, sticky=tk.W)

# Column 2
tk.Label(root, text = "Laser scan mode (0: step, 1: cont)").grid(row=0, column
    =2, padx=5, pady=5, sticky=tk.E)
tk.Label(root, text = "Contineous laser scan speed (defult = 10 nm/s)").grid(
    row=1, column=2, padx=5, pady=5, sticky=tk.E)
tk.Label(root, text = "Scan step size (defult = 0.01 nm  (10pm), minimum
    0.0001 nm (0.1pm))").grid(row=2, column=2, padx=5, pady=5, sticky=tk.E)
tk.Label(root, text = "Scan dwell time (defult = 0.5 s)").grid(row=3, column
    =2, padx=5, pady=5, sticky=tk.E)

# Column 3
# Place the entry widgets in the GUI
scan_mode_entry.grid(row=0, column=3, padx=5, pady=5, sticky=tk.W)
speed_entry.grid(row=1, column=3, padx=5, pady=5, sticky=tk.W)
step_size_entry.grid(row=2, column=3, padx=5, pady=5, sticky=tk.W)
dwell_time_entry.grid(row=3, column=3, padx=5, pady=5, sticky=tk.W)

# insert defult values
scan_mode_entry.insert(0, "1")  # Default scan mode
speed_entry.insert(0, "10")  # Default laser scan speed
rate_entry.insert(0, "10000")  # Default sampling rate
start_wl_entry.insert(0, "1530")  # Default start wavelength
end_wl_entry.insert(0, "1620")  # Default end wavelength
reset_entry.insert(0, "1550") # Default reset wavelength
step_size_entry.insert(0, "0.01")  # Default step size
dwell_time_entry.insert(0, "0.5")  # Default dwell time
filename_entry.insert(0, "figure_data.csv")  # Default filename

# Plot laser scan
fig = Figure(figsize=(10, 6), dpi=100)
ax1 = fig.add_subplot(2, 1, 1)
ax2 = fig.add_subplot(2, 1, 2)
canvas = FigureCanvasTkAgg(fig, master=root)  # A tk.DrawingArea.
canvas.get_tk_widget().grid(row=8, column=0, columnspan=2, sticky=tk.NSEW)
```

```
toolbar_frame = tk.Frame(root)
toolbar_frame.grid(row=9, column=0, columnspan=2, sticky=tk.NSEW)

canvas = FigureCanvasTkAgg(fig, master=root)  # A tk.DrawingArea.
canvas.get_tk_widget().grid(row=8, column=0, columnspan=2, sticky=tk.NSEW)

toolbar = NavigationToolbar2Tk(canvas, toolbar_frame)
toolbar.update()

ax1.set_title('PD0')
ax2.set_title('PD1')
ax1.set_xlabel('Wavelength (nm)')
ax2.set_xlabel('Wavelength (nm)')
fig.tight_layout()

# Pring laser setup info
print_info_var = tk.BooleanVar()
print_info_checkbutton = tk.Checkbutton(root, text="Print laser reset Info?",
    variable=print_info_var)
print_info_checkbutton.grid(row=5, column=1, sticky=tk.N)

tk.Button(root, text='Run Sweep', command=run_laser_scan_thread).grid(row=0,
    column=0, sticky=tk.N, pady=5)
tk.Button(root, text='Reset Laser', command=reset_laser).grid(row=3, column=0,
     sticky=tk.N, pady=5)
tk.Button(root, text='Quit', command=quit_program).grid(row=7, column=3,
    sticky=tk.N, pady=5)
tk.Button(root, text='Save Data',
      command=lambda: save_figure_data(root.x_values, root.pd0, root.pd1,
          filename_entry.get())).grid(row=4, column=0, sticky=tk.N, pady=5)

status_label = tk.Label(root, text="", font=("Helvetica", 12, "bold"))
status_label.grid(row=6, column=1)

# Animation for contineous PD
start_button = tk.Button(master=root, text="Start aquiring", command=
    start_animation)
start_button.grid(row=1, column=1, sticky=tk.N)

stop_button = tk.Button(master=root, text="Stop aquiring", command=
    stop_animation)
stop_button.grid(row=2, column=1, sticky=tk.N)

reset_button = tk.Button(master=root, text="Reset Figure", command=
    reset_figure)
reset_button.grid(row=3, column=1, sticky=tk.N)

show_dev2 = tk.BooleanVar()
show_dev2_HPD_checkbutton = tk.Checkbutton(root, text="Show HDP readout",
    variable=show_dev2)
show_dev2_HPD_checkbutton.grid(row=4, column=1, sticky=tk.N)

# VNA related control
# Create an entry for the VNA frequency
```

```
# Create a button to set the VNA frequency
VNA_freq_button = tk.Button(root, text="Set VNA Frequency", command=
    VNA_set_CW_freq)
VNA_freq_button.grid(row=0, column=0, padx=5, pady=5, sticky=tk.W)
# Create an entry for the VNA frequency
VNA_freq_entry = tk.Entry(root)
VNA_freq_entry.insert(0, "3.0854")  # Set the default value
VNA_freq_entry.grid(row=1, column=0, padx=3, pady=5, sticky=tk.W)  # Add
    padding and align to the right
tk.Label(root, text="GHz").grid(row=2, column=0, padx=5, pady=5, sticky=tk.W)

# Create a button to set the VNA power
VNA_pow_button = tk.Button(root, text="Set VNA Power", command=VNA_set_power)
VNA_pow_button.grid(row=3, column=0, padx=5, pady=5, sticky=tk.W)
# Create an entry for the VNA power
VNA_pow_entry = tk.Entry(root)
VNA_pow_entry.insert(0, "0")  # Set the default value
VNA_pow_entry.grid(row=4, column=0, padx=3, pady=5, sticky=tk.W)  # Add
    padding and align to the right
tk.Label(root, text="dBm").grid(row=5, column=0, padx=5, pady=5, sticky=tk.W)

# Create a button to turn on the VNA power
# Create a BooleanVar to keep track of the power status
VNA_power_status1 = tk.BooleanVar()
VNA_power_status1.set(False)  # Initially, the power is off
VNA_power_on_button1 = tk.Button(root, text="Toggle VNA Power 1", command=
    toggle_VNA_power1)
VNA_power_on_button1.grid(row=7, column=0, padx=5, pady=5, sticky=tk.W)
VNA_power_status2 = tk.BooleanVar()
VNA_power_status2.set(False)  # Initially, the power is off
VNA_power_on_button2 = tk.Button(root, text="Toggle VNA Power 2", command=
    toggle_VNA_power2)
VNA_power_on_button2.grid(row=7, column=0, padx=5, pady=5, sticky=tk.N)

# Create a button to set the VNA to CW mode
VNA_mode_status = tk.BooleanVar()
VNA_mode_status.set(False)  # False is LIN mode
VNA_CW_mode_button = tk.Button(root, text="Toggle VNA Mode", command=
    toggle_VNA_mode)
VNA_CW_mode_button.grid(row=6, column=0, padx=5, pady=5, sticky=tk.W)

# Create a buttom to clear the averaging of the acquired data
VNA_clear_button = tk.Button(root, text="Restart VNA Averaging", command=
    lambda: VNA.write('SENS:AVER:CLE'))
VNA_clear_button.grid(row=6, column=0, padx=5, pady=5, sticky=tk.N)

root.mainloop()
```

Appendix VII: Fabrication recipes

Optomechanical Rings Resonator on Silicon-on-Sapphire (SOS) Fabrication Recipe

EBL process for optical layers (wg, gc, rings)

- ZEP Z0
    - 2000rpm, 120°C for 5 minutes
    - Discharger at same spin speed
- Write with 1nA, 5th lens (M6)
    - Dose: 360
    - Pitch: 22
- Develop
    - Amylacetate 60 seconds
    - IPA flush 60 seconds (with stirring)
- Yes-asher 3 seconds

ICP-C Etching

- Preconditioning before etching

ICP-C Recipes:

1. QTSYS - Ar/H_2 10 minutes
2. ML- CL clean 35 minutes
3. ML- Si etch Dec

Strip ZEP0

- NMP

ZnO Pads

- Haidelburg (Or can use 8nA EBL metal finger recipe to write ZnO Pad)
  - AZ1512 3000rpm, 110°C 1 minute
  - 4mm alignment head (Align in Micro mode)
  - Length, height = 7500, 6000 µm
  - Offset = -3.75, -3.00 mm
  - Recipe: use manual job
  - Develop: AZ340:H_2O bath 20 seconds
  - Yes asher: 15 seconds
- SPUT3 Lesker
  - Gun4 RF ZnO
  - Recipe: 2 hours 20 minutes
  - Lift-off (Small sonicator):
    - Frequency: 80
    - Power: 50
    - Time: 1 minute 30 seconds

Metal Fingers and Pads

- EBL
  - ZEP0, 2000RPM, 120c 5min
  - Cool 5 min
  - Discharger 2000RPM
  - 8nA M3, dose: 425 c/cm2, shot pitch 12
  - EBL write, around 40 min (SOS1)
  - Pitch: 18
  - develop: Amyl Acetate (1 min) → IPA (1 min) → DI water (30s)
  - YES ASHER 3sec
- EVAP1
  - 220 nm Aluminum
  - Acetone heat to 70°C lift-off
  - Lift-off (Small sonicator):
    - Frequency: 80
    - Power: 50
    - Time: 1 minute 30 seconds

BGaP continuous film transfer to sapphire substrate

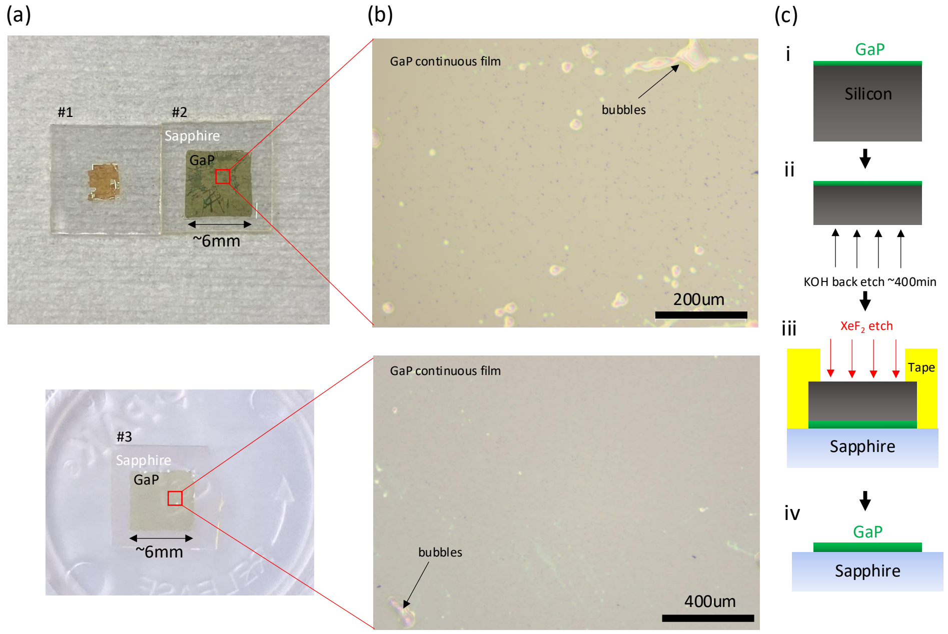

Figure A.6: BGaP-on-silicon transfer process a. Pictures of continuous BGaP film transfer on to sapphire substrate. **b.** Microscope image of the transferred BGaP film. **c.** Process flow for the transfer procedure. i. The BGaP (266 nm)-on-silicon (740 µm) is loaded to a KOH wet etch holder with silicon side exposed. The holder is from AMMT. ii. The silicon side exposed with the holder is soaked into a 70 degree C warm KOH bath in the wet etch bay and etch for $\sim$ 400 minutes to remove bulk of the silicon. iii. Roughly 70 µm of the remaining silicon is then taped to a sapphire substrate with kapton thermal tape with BGaP side facing down. Finally, the remaining silicon is removed via XeF$_2$ dry etch.

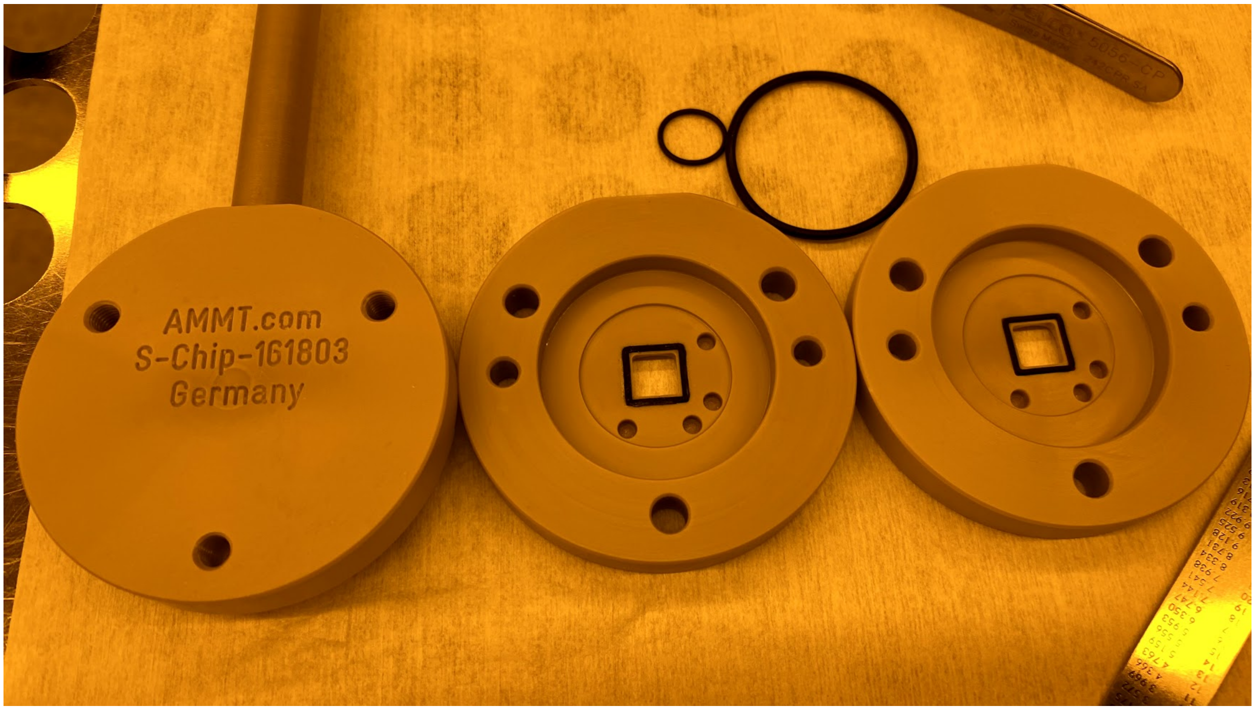

Figure A.7: A picture of the AMMT KOH chip holder

Bibliography

[1] N. S. Yama, I.-T. Chen, S. Chakravarthi, B. Li, C. Pederson, B. E. Matthews, S. R. Spurgeon, D. E. Perea, M. G. Wirth, P. V. Sushko, M. Li, and K.-M. C. Fu, "Silicon-lattice-matched boron-doped gallium phosphide: A scalable acousto-optic platform," *Advanced Materials*, p. 2305434, 2023.

[2] I.-T. Chen, B. Li, S. Lee, S. Chakravarthi, K.-M. Fu, and M. Li, "Optomechanical ring resonator for efficient microwave-optical frequency conversion," 2023.

[3] J. Komma, C. Schwarz, G. Hofmann, D. Heinert, and R. Nawrodt, "Thermo-optic coefficient of silicon at 1550 nm and cryogenic temperatures," *Applied Physics Letters*, vol. 101, p. 041905, 07 2012.

[4] U. Adya, R. Chen, I.-T. Chen, S. Joshi, A. Majumdar, M. Li, and S. Moazeni, "Non-volatile tuning of cryogenic optical resonators," 2024.

[5] H. H. Li, "Refractive index of silicon and germanium and its wavelength and temperature derivatives," *Journal of Physical and Chemical Reference Data*, vol. 9, pp. 561–658, 07 1980.

[6] D. K. Biegelsen, "Photoelastic tensor of silicon and the volume dependence of the average gap," *Phys. Rev. Lett.*, vol. 32, pp. 1196–1199, May 1974.

[7] J. Dickmann, J. Meyer, M. Gaedtke, and S. Kroker, "Temperature-dependent photo-elastic coefficient of silicon at 1550 nm," *Scientific Reports*, vol. 13, no. 1, p. 19455, 2023.

[8] M. E. Beverland, P. Murali, M. Troyer, K. M. Svore, T. Hoefler, V. Kliuchnikov, G. H. Low, M. Soeken, A. Sundaram, and A. Vaschillo, "Assessing requirements to scale to practical quantum advantage," *arXiv:*, 2022.

[9] Krinner, S., Storz, S., Kurpiers, P., Magnard, P., Heinsoo, J., Keller, R., Lütolf, J., Eichler, C., and Wallraff, A., "Engineering cryogenic setups for 100-qubit scale superconducting circuit systems," *EPJ Quantum Technol.*, vol. 6, no. 1, p. 2, 2019.

[10] A. Youssefi, I. Shomroni, Y. J. Joshi, N. R. Bernier, A. Lukashchuk, P. Uhrich, L. Qiu, and T. J. Kippenberg, "A cryogenic electro-optic interconnect for superconducting devices," *Nature Electronics*, vol. 4, no. 5, pp. 326–332, 2021.

[11] Y. Kim, A. Eddins, S. Anand, K. X. Wei, E. van den Berg, S. Rosenblatt, H. Nayfeh, Y. Wu, M. Zaletel, K. Temme, and A. Kandala, "Evidence for the utility of quantum computing before fault tolerance," *Nature*, vol. 618, 500–505, 2023.

[12] R. D. Delaney, M. D. Urmey, S. Mittal, B. M. Brubaker, J. M. Kindem, P. S. Burns, C. A. Regal, and K. W. Lehnert, "Superconducting-qubit readout via low-backaction electro-optic transduction," *Nature*, vol. 606, no. 7914, pp. 489–493, 2022.

[13] W. Jiang, C. J. Sarabalis, Y. D. Dahmani, R. N. Patel, F. M. Mayor, T. P. McKenna, R. Van Laer, and A. H. Safavi-Naeini, "Efficient bidirectional piezo-optomechanical transduction between microwave and optical frequency," *Nature Communications*, vol. 11, no. 1, p. 1166, 2020.

[14] C. O'Brien, N. Lauk, S. Blum, G. Morigi, and M. Fleischhauer, "Interfacing superconducting qubits and telecom photons via a rare-earth-doped crystal," *Phys. Rev. Lett.*, vol. 113, p. 063603, Aug 2014.

[15] N. Zhu, X. Zhang, X. Han, C.-L. Zou, C. Zhong, C.-H. Wang, L. Jiang, and H. X. Tang, "Waveguide cavity optomagnonics for microwave-to-optics conversion," *Optica*, vol. 7, pp. 1291–1297, Oct 2020.

[16] Brillouin, Léon, "Diffusion de la lumière et des rayons x par un corps transparent homogène - influence de l'agitation thermique," *Ann. Phys.*, vol. 9, no. 17, pp. 88–122, 1922.

[17] C. Wolff, M. J. A. Smith, B. Stiller, and C. G. Poulton, "Brillouin scattering—theory and experiment: tutorial," *J. Opt. Soc. Am. B*, vol. 38, pp. 1243–1269, Apr 2021.

[18] C. C. Rodrigues, N. J. Schilder, R. O. Zurita, L. S. Magalhães, A. Shams-Ansari, F. J. L. dos Santos, O. M. Paiano, T. P. M. Alegre, M. Lončar, and G. S. Wiederhecker, "Cross-polarized stimulated brillouin scattering in lithium niobate waveguides," *Phys. Rev. Lett.*, vol. 134, p. 113601, Mar 2025.

[19] A. Kobyakov, M. Sauer, and D. Chowdhury, "Stimulated brillouin scattering in optical fibers," *Adv. Opt. Photon.*, vol. 2, pp. 1–59, Mar 2010.

[20] S. B. K. Hönl, T. Kippenberg, and P. F. Seidler, "Microwave-to-optical transduction with gallium phosphide electro-optomechanical devices," 2021.

[21] C. S. Tsai, *Guided-Wave Acousto-Optics Interactions, Devices, and Applications.* Berlin Heidelberg: Springer-Verlag, 1990.

[22] A. Korpel, "Acousto-optics—a review of fundamentals," *Proceedings of the IEEE*, vol. 69, no. 1, pp. 48–53, 1981.

[23] D. B. Sohn, S. Kim, and G. Bahl, "Time-reversal symmetry breaking with acoustic pumping of nanophotonic circuits," *Nature Photonic*, vol. 12, 91–97, 2018.

[24] Q. Liu, H. Li, and M. Li, "Electromechanical brillouin scattering in integrated optomechanical waveguides," *Optica*, vol. 6, pp. 778–785, Jun 2019.

[25] S. A. Tadesse and M. Li, "Sub-optical wavelength acoustic wave modulation of integrated photonic resonators at microwave frequencies," *Nature Communications*, vol. 5, no. 1, p. 5402, 2014.

[26] L. Shao, M. Yu, S. Maity, N. Sinclair, L. Zheng, C. Chia, A. Shams-Ansari, C. Wang, M. Zhang, K. Lai, and M. Lončar, "Microwave-to-optical conversion using lithium niobate thin-film acoustic resonators," *Optica*, vol. 6, pp. 1498–1505, Dec 2019.

[27] E. A. Kittlaus, W. M. Jones, P. T. Rakich, N. T. Otterstrom, R. E. Muller, and M. Rais-Zadeh, "Electrically driven acousto-optics and broadband non-reciprocity in silicon photonics," *Nature Photonics*, vol. 15, no. 1, pp. 43–52, 2021.

[28] Y. Zhou, F. Ruesink, S. Gertler, H. Cheng, M. Pavlovich, E. Kittlaus, A. L. Starbuck, A. J. Leenheer, A. T. Pomerene, D. C. Trotter, C. Dallo, K. M. Musick, E. Garcia, R. Reyna, A. L. Holterhoff, M. Gehl, A. Kodigala, J. Bowers, M. Eichenfield, N. T. Otterstrom, A. L. Lentine, and P. Rakich, "Nonreciprocal dissipation engineering via strong coupling with a continuum of modes," *Phys. Rev. X*, vol. 14, p. 021002, Apr 2024.

[29] L. Zhang, C. Cui, P.-K. Chen, and L. Fan, "Integrated-waveguide-based acousto-optic modulation with complete optical conversion," *Optica*, vol. 11, pp. 184–189, Feb 2024.

[30] M. Aspelmeyer, T. J. Kippenberg, and F. Marquardt, "Cavity optomechanics," *Reviews of Modern Physics*, vol. 86, pp. 1391–1452, dec 2014.

[31] S. G. Johnson, M. Ibanescu, M. A. Skorobogatiy, O. Weisberg, J. D. Joannopoulos, and Y. Fink, "Perturbation theory for maxwell's equations with shifting material boundaries," *Phys. Rev. E*, vol. 65, p. 066611, Jun 2002.

[32] B. G. Mytsyk, N. M. Demyanyshyn, and O. M. Sakharuk, "Elasto-optic effect anisotropy in gallium phosphide crystals," *Applied Optics*, vol. 54, no. 8546-8553, 2015.

[33] R. W. Dixon, "Photoelastic Properties of Selected Materials and Their Relevance for Applications to Acoustic Light Modulators and Scanners," *Journal of Applied Physics*, vol. 38, pp. 5149–5153, 06 2004.

[34] X. Han, W. Fu, C.-L. Zou, L. Jiang, and H. X. Tang, "Microwave-optical quantum frequency conversion," *Optica*, vol. 8, pp. 1050–1064, Aug 2021.

[35] A. D. O'Connell, M. Hofheinz, M. Ansmann, R. C. Bialczak, M. Lenander, E. Lucero, M. Neeley, D. Sank, H. Wang, M. Weides, J. Wenner, J. M. Martinis, and A. N. Cleland, "Quantum ground state and single-phonon control of a mechanical resonator," *Nature*, vol. 464, no. 7289, pp. 697–703, 2010.

[36] Y. Chu, P. Kharel, W. H. Renninger, L. D. Burkhart, L. Frunzio, P. T. Rakich, and R. J. Schoelkopf, "Quantum acoustics with superconducting qubits," *Science*, vol. 358, no. 6360, pp. 199–202, 2017.

[37] K. J. Satzinger, Y. P. Zhong, H. S. Chang, G. A. Peairs, A. Bienfait, M.-H. Chou, A. Y. Cleland, C. R. Conner, É. Dumur, J. Grebel, I. Gutierrez, B. H. November, R. G. Povey, S. J. Whiteley, D. D. Awschalom, D. I. Schuster, and A. N. Cleland, "Quantum control of surface acoustic-wave phonons," *Nature*, vol. 563, no. 7733, pp. 661–665, 2018.

[38] M. Mirhosseini, A. Sipahigil, M. Kalaee, and O. Painter, "Superconducting qubit to optical photon transduction," *Nature*, vol. 588, no. 7839, pp. 599–603, 2020.

[39] A. Vainsencher, K. J. Satzinger, G. A. Peairs, and A. N. Cleland, "Bi-directional conversion between microwave and optical frequencies in a piezoelectric optomechanical device," *Applied Physics Letters*, vol. 109, p. 033107, 07 2016.

[40] M. Forsch, R. Stockill, A. Wallucks, I. Marinković, C. Gärtner, R. A. Norte, F. van Otten, A. Fiore, K. Srinivasan, and S. Gröblacher, "Microwave-to-optics conversion using a mechanical oscillator in its quantum ground state," *Nature Physics*, vol. 16, no. 1, pp. 69–74, 2020.

[41] M. J. Weaver, P. Duivestein, A. C. Bernasconi, S. Scharmer, M. Lemang, T. C. v. Thiel, F. Hijazi, B. Hensen, S. Gröblacher, and R. Stockill, "An integrated microwave-to-optics interface for scalable quantum computing," *Nature Nanotechnology*, 2023.

[42] A. Rueda, F. Sedlmeir, M. C. Collodo, U. Vogl, B. Stiller, G. Schunk, D. V. Strekalov, C. Marquardt, J. M. Fink, O. Painter, G. Leuchs, and H. G. L. Schwefel, "Efficient microwave to optical photon conversion: an electro-optical realization," *Optica*, vol. 3, pp. 597–604, Jun 2016.

[43] W. Hease, A. Rueda, R. Sahu, M. Wulf, G. Arnold, H. G. Schwefel, and J. M. Fink, "Bidirectional electro-optic wavelength conversion in the quantum ground state," *PRX Quantum*, vol. 1, p. 020315, Nov 2020.

[44] J. Orcutt, H. Paik, L. Bishop, C. Xiong, R. Schilling, and A. Falk, "Engineering electro-optics in sige/si waveguides for quantum transduction," *Quantum Sci. Technol.*, vol. 5, 034006, 2020.

[45] R. Sahu, L. Qiu, W. Hease, G. Arnold, Y. Minoguchi, P. Rabl, and J. M. Fink, "Entangling microwaves with light," *Science*, vol. 380, no. 6646, pp. 718–721, 2023.

[46] F. Mondain, F. Brunel, X. Hua, E. Gouzien, A. Zavatta, T. Lunghi, F. Doutre, M. P. D. Micheli, S. Tanzilli, and V. D'Auria, "Photorefractive effect in linbo3-based integrated-optical circuits for continuous variable experiments," *Opt. Express*, vol. 28, pp. 23176–23188, Aug 2020.

[47] T. Volk, N. Rubinina, and M. Wöhlecke, "Optical-damage-resistant impurities in lithium niobate," *J. Opt. Soc. Am. B*, vol. 11, pp. 1681–1687, Sep 1994.

[48] A. Rueda, W. Hease, S. Barzanjeh, and J. M. Fink, "Electro-optic entanglement source for microwave to telecom quantum state transfer," *npj Quantum Information*, vol. 5, no. 1, p. 108, 2019.

[49] W. L. Bond, "Measurement of the Refractive Indices of Several Crystals," *Journal of Applied Physics*, vol. 36, pp. 1674–1677, 07 2004.

[50] A. D. Corso, F. Mauri, and A. Rubio, "Density-functional theory of the nonlinear optical susceptibility: Application to cubic semiconductors," *Phys. Rev. B*, vol. 53, pp. 15638–15642, Jun 1996.

[51] J. Slobodnik, A. J., P. H. Carr, and A. J. Budreau, "Microwave Frequency Acoustic Surface-Wave Loss Mechanisms on LiNbO3," *Journal of Applied Physics*, vol. 41, pp. 4380–4387, 12 2003.

[52] F. M. Mayor, W. Jiang, C. J. Sarabalis, T. P. McKenna, J. D. Witmer, and A. H. Safavi-Naeini, "Gigahertz phononic integrated circuits on thin-film lithium niobate on sapphire," *Phys. Rev. Appl.*, vol. 15, p. 014039, Jan 2021.

[53] Y. Vlasov, W. M. J. Green, and F. Xia, "High-throughput silicon nanophotonic wavelength-insensitive switch for on-chip optical networks," *Nature Photonics*, vol. 2, no. 4, pp. 242–246, 2008.

[54] Q. Xu, B. Schmidt, S. Pradhan, and M. Lipson, "Micrometre-scale silicon electro-optic modulator," *Nature*, vol. 435, no. 7040, pp. 325–327, 2005.

[55] D. J. Wilson, K. Schneider, S. Hönl, M. Anderson, Y. Baumgartner, L. Czornomaz, T. J. Kippenberg, and P. Seidler, "Integrated gallium phosphide nonlinear photonics," *Nature Photonics*, vol. 14, no. 1, pp. 57–62, 2020.

[56] Y. D. Dahmani, C. J. Sarabalis, W. Jiang, F. M. Mayor, and A. H. Safavi-Naeini, "Piezoelectric transduction of a wavelength-scale mechanical waveguide," *Phys. Rev. Appl.*, vol. 13, p. 024069, Feb 2020.

[57] C. J. Sarabalis, R. V. Laer, R. N. Patel, Y. D. Dahmani, W. Jiang, F. M. Mayor, and A. H. Safavi-Naeini, "Acousto-optic modulation of a wavelength-scale waveguide," *Optica*, vol. 8, pp. 477–483, Apr 2021.

[58] F. M. Mayor, W. Jiang, C. J. Sarabalis, T. P. McKenna, J. D. Witmer, and A. H. Safavi-Naeini, "Gigahertz phononic integrated circuits on thin-film lithium niobate on sapphire," *Phys. Rev. Appl.*, vol. 15, p. 014039, Jan 2021.

[59] W. Fu, Z. Shen, Y. Xu, C.-L. Zou, R. Cheng, X. Han, and H. X. Tang, "Phononic integrated circuitry and spin–orbit interaction of phonons," *Nature Communications*, vol. 10, no. 1, p. 2743, 2019.

[60] L. Shao, D. Zhu, M. Colangelo, D. Lee, N. Sinclair, Y. Hu, P. T. Rakich, K. Lai, K. K. Berggren, and M. Lončar, "Electrical control of surface acoustic waves," *Nature Electronics*, vol. 5, no. 6, pp. 348–355, 2022.

[61] A. D. Logan, S. Shree, S. Chakravarthi, N. Yama, C. Pederson, K. Hestroffer, F. Hatami, and K.-M. C. Fu, "Triply-resonant sum frequency conversion with gallium phosphide ring resonators," *Opt. Express*, vol. 31, pp. 1516–1531, Jan 2023.

[62] M. Mitchell, A. C. Hryciw, and P. E. Barclay, "Cavity optomechanics in gallium phosphide microdisks," *Applied Physics Letters*, vol. 104, no. 14, p. 141104, 2014.

[63] K. Schneider, Y. Baumgartner, S. Hönl, P. Welter, H. Hahn, D. J. Wilson, L. Czornomaz, and P. Seidler, "Optomechanics with one-dimensional gallium phosphide photonic crystal cavities," *Optica*, vol. 6, pp. 577–584, May 2019.

[64] S. Hönl, Y. Popoff, D. Caimi, A. Beccari, T. J. Kippenberg, and P. Seidler, "Microwave-to-optical conversion with a gallium phosphide photonic crystal cavity," *Nature Communications*, vol. 13, no. 1, p. 2065, 2022.

[65] S. Chakravarthi, N. S. Yama, A. Abulnaga, D. Huang, C. Pederson, K. Hestroffer, F. Hatami, N. P. de Leon, and K.-M. C. Fu, "Hybrid integration of gap photonic crystal cavities with silicon-vacancy centers in diamond by stamp-transfer," *Nano Letters*, vol. 23, pp. 3708–3715, 5 2023. doi: 10.1021/acs.nanolett.2c04890.

[66] B. Kunert, S. Zinnkann, K. Volz, and W. Stolz, "Monolithic integration of ga(nasp)/(bga)p multi-quantum well structures on (001) silicon substrate by movpe," *Journal of Crystal Growth*, vol. 310, no. 23, pp. 4776–4779, 2008. The Fourteenth International conference on Metalorganic Vapor Phase Epitax.

[67] "The 2019 surface acoustic waves roadmap," *Journal of Physics D: Applied Physics*, vol. 52, p. 353001, 2019.

[68] W. Fu, Z. Shen, Y. Xu, C.-L. Zou, R. Cheng, X. Han, and H. X. Tang, "Phononic integrated circuitry and spin–orbit interaction of phonons," *Nature Communications*, vol. 10, 2743, 2019.

[69] Y. D. Dahmani, C. J. Sarabalis, W. Jiang, F. M. Mayor, and A. H. Safavi-Naeini, "Piezoelectric transduction of a wavelength-scale mechanical waveguide," *Phys. Rev. Applied*, vol. 13, 024069, p. 24069, 2 2020.

[70] F. M. Mayor, W. Jiang, C. J. Sarabalis, T. P. McKenna, J. D. Witmer, and A. H. Safavi-Naeini, "Gigahertz phononic integrated circuits on thin-film lithium niobate on sapphire," *Phys. Rev. Applied*, vol. 15, 014039, 1 2021.

[71] X.-B. Xu, J.-Q. Wang, Y.-H. Yang, W. Wang, Y.-L. Zhang, B.-Z. Wang, C.-H. Dong, L. Sun, G.-C. Guo, and C.-L. Zou, "High-frequency traveling-wave phononic cavity with sub-micron wavelength," *Appl. Phys. Lett*, vol. 120, 163503, 2022.

[72] X. Han, W. Fu, C. Zhong, C.-L. Zou, Y. Xu, A. A. Sayem, M. Xu, S. Wang, R. Cheng, L. Jiang, and H. X. Tang, "Cavity piezo-mechanics for superconducting-nanophotonic quantum interface," *Nature Communications*, vol. 11, no. 1, p. 3237, 2020.

[73] X.-Q. He, P. Gómez García, and J.-P. Fernández-Álvarez, "Floquet-bloch theory and its application to the dispersion curves of nonperiodic layered systems," *Mathematical Problems in Engineering*, vol. 2015, p. 475364, 2015.

[74] G. Calajó, M. J. A. Schuetz, H. Pichler, M. D. Lukin, P. Schneeweiss, J. Volz, and P. Rabl, "Quantum acousto-optic control of light-matter interactions in nanophotonic networks," *Phys. Rev. A*, vol. 99, p. 053852, May 2019.

[75] I. H. Malitson, "Refraction and dispersion of synthetic sapphire," *J. Opt. Soc. Am.*, vol. 52, pp. 1377–1379, Dec 1962.

[76] A. Neubrand and P. Hess, "Laser generation and detection of surface acoustic waves: Elastic properties of surface layers," *Journal of Applied Physics*, vol. 71, pp. 227–238, 01 1992.

[77] B. A. Auld, *Acoustic fields and waves in solids.* Wiely, 1973.

[78] J. M. Winey, Y. M. Gupta, and D. E. Hare, "r-axis sound speed and elastic properties of sapphire single crystals," *Journal of Applied Physics*, vol. 90, pp. 3109–3111, 09 2001.

[79] F. Hassani, M. Peruzzo, L. N. Kapoor, A. Trioni, M. Zemlicka, and J. M. Fink, “Inductively shunted transmons exhibit noise insensitive plasmon states and a fluxon decay exceeding 3 hours,” *Nature Communications*, vol. 14, no. 1, p. 3968, 2023.

[80] I. Siddiqi, “Engineering high-coherence superconducting qubits,” *Nature Reviews Materials*, vol. 6, no. 10, pp. 875–891, 2021.

[81] A. P. M. Place, L. V. H. Rodgers, P. Mundada, B. M. Smitham, M. Fitzpatrick, Z. Leng, A. Premkumar, J. Bryon, A. Vrajitoarea, S. Sussman, G. Cheng, T. Madhavan, H. K. Babla, X. H. Le, Y. Gang, B. Jäck, A. Gyenis, N. Yao, R. J. Cava, N. P. de Leon, and A. A. Houck, “New material platform for superconducting transmon qubits with coherence times exceeding 0.3 milliseconds,” *Nature Communications*, vol. 12, no. 1, p. 1779, 2021.

[82] A. J. Keller, P. B. Dieterle, M. Fang, B. Berger, J. M. Fink, and O. Painter, “Al transmon qubits on silicon-on-insulator for quantum device integration,” *Applied Physics Letters*, vol. 111, p. 042603, 07 2017.

[83] M. Chen, J. C. Owens, H. Putterman, M. Schäfer, and O. Painter, “Phonon engineering of atomic-scale defects in superconducting quantum circuits,” *Science Advances*, vol. 10, no. 37, p. eado6240, 2024.

[84] C. Wang, X. Li, H. Xu, Z. Li, J. Wang, Z. Yang, Z. Mi, X. Liang, T. Su, C. Yang, G. Wang, W. Wang, Y. Li, M. Chen, C. Li, K. Linghu, J. Han, Y. Zhang, Y. Feng, Y. Song, T. Ma, J. Zhang, R. Wang, P. Zhao, W. Liu, G. Xue, Y. Jin, and H. Yu, “Towards practical quantum computers: transmon qubit with a lifetime approaching 0.5 milliseconds,” *npj Quantum Information*, vol. 8, no. 1, p. 3, 2022.

[85] M. Tsang, “Cavity quantum electro-optics,” *Phys. Rev. A*, vol. 81, p. 063837, Jun 2010.

[86] M. Wolfmeyer and J. Dillinger, “The thermal conductivity of sapphire between 0.4 and 4 °k,” *Physics Letters A*, vol. 34, no. 4, pp. 247–248, 1971.

[87] M. J. Weaver, P. Duivestein, A. C. Bernasconi, S. Scharmer, M. Lemang, T. C. v. Thiel, F. Hijazi, B. Hensen, S. Gröblacher, and R. Stockill, “An integrated microwave-to-optics interface for scalable quantum computing,” *Nature Nanotechnology*, vol. 19, no. 2, pp. 166–172, 2024.

[88] F. M. Mayor, S. Malik, A. G. Primo, S. Gyger, O. A. Hitchcock, K. K. S. Multani, W. Jiang, T. P. M. Alegre, and A. H. Safavi-Naeini, “A microwave-to-optical transducer based on a two-dimensional optomechanical crystal,” in *Quantum 2.0 Conference and Exhibition*, p. QTu4A.4, Optica Publishing Group, 2024.

[89] S. Sonar, U. Hatipoglu, S. Meesala, D. P. Lake, H. Ren, and O. Painter, “High-efficiency low-noise optomechanical crystal photon-phonon transducers,” *Optica*, vol. 12, pp. 99–104, Jan 2025.

[90] S. Mahashabde, E. Otto, D. Montemurro, S. de Graaf, S. Kubatkin, and A. Danilov, “Fast tunable high-q-factor superconducting microwave resonators,” *Phys. Rev. Appl.*, vol. 14, p. 044040, Oct 2020.

[91] G. Arnold, T. Werner, R. Sahu, L. N. Kapoor, L. Qiu, and J. M. Fink, "All-optical superconducting qubit readout," *Nature Physics*, https://doi.org/10.1038/s41567-024-02741-4, 2025.

[92] L. Shao, N. Sinclair, J. Leatham, Y. Hu, M. Yu, T. Turpin, D. Crowe, and M. Lončar, "Integrated microwave acousto-optic frequency shifter on thin-film lithium niobate," *Opt. Express*, vol. 28, pp. 23728–23738, Aug 2020.

[93] H. Tian, J. Liu, A. Siddharth, R. N. Wang, T. Blésin, J. He, T. J. Kippenberg, and S. A. Bhave, "Magnetic-free silicon nitride integrated optical isolator," *Nature Photonics*, vol. 15, no. 11, pp. 828–836, 2021.

[94] F. Lecocq, F. Quinlan, K. Cicak, J. Aumentado, S. A. Diddams, and J. D. Teufel, "Control and readout of a superconducting qubit using a photonic link," *Nature*, vol. 591, no. 7851, pp. 575–579, 2021.

[95] G. Arnold, T. Werner, R. Sahu, L. N. Kapoor, L. Qiu, and J. M. Fink, "All-optical superconducting qubit readout," *Nature Physics*, 2025.

[96] T. C. van Thiel, M. J. Weaver, F. Berto, P. Duivestein, M. Lemang, K. L. Schuurman, M. Žemlička, F. Hijazi, A. C. Bernasconi, C. Ferrer, E. Cataldo, E. Lachman, M. Field, Y. Mohan, F. K. de Vries, C. C. Bultink, J. C. van Oven, J. Y. Mutus, R. Stockill, and S. Gröblacher, "Optical readout of a superconducting qubit using a piezo-optomechanical transducer," *Nature Physics*, 2025.

[97] X. Han, W. Fu, C. Zhong, C.-L. Zou, Y. Xu, A. A. Sayem, M. Xu, S. Wang, R. Cheng, L. Jiang, and H. X. Tang, "Cavity piezo-mechanics for superconducting-nanophotonic quantum interface," *Nature Communications*, vol. 11, no. 1, p. 3237, 2020.

[98] M. Gehl, C. Long, D. Trotter, A. Starbuck, A. Pomerene, J. B. Wright, S. Melgaard, J. Sirola, A. L. Lentine, and C. DeRose, "Operation of high-speed silicon photonic micro-disk modulators at cryogenic temperatures," *Optica*, vol. 4, pp. 374–382, Mar 2017.

[99] H. Gevorgyan, A. Khilo, D. V. Orden, D. Onural, B. Yin, M. T. Wade, V. M. Stojanović, and M. A. Popović, "Cryo-compatible, silicon spoked-ring modulator in a 45nm cmos platform for 4k-to-room-temperature optical links," in *2021 Optical Fiber Communications Conference and Exhibition (OFC)*, pp. 1–3, 2021.

[100] M. Dong, G. Clark, A. J. Leenheer, M. Zimmermann, D. Dominguez, A. J. Menssen, D. Heim, G. Gilbert, D. Englund, and M. Eichenfield, "High-speed programmable photonic circuits in a cryogenically compatible, visible–near-infrared 200 mm cmos architecture," *Nature Photonics*, vol. 16, no. 1, pp. 59–65, 2022.

[101] S. Joshi and S. Moazeni, "Scaling up superconducting quantum computers with cryogenic rf-photonics," *Journal of Lightwave Technology*, vol. 42, no. 1, pp. 166–175, 2024.

[102] J. M. Hornibrook, J. I. Colless, I. D. Conway Lamb, S. J. Pauka, H. Lu, A. C. Gossard, J. D. Watson, G. C. Gardner, S. Fallahi, M. J. Manfra, and D. J. Reilly, "Cryogenic control architecture for large-scale quantum computing," *Phys. Rev. Appl.*, vol. 3, p. 024010, Feb 2015.

[103] H. Li, Q. Liu, and M. Li, "Electromechanical Brillouin scattering in integrated planar photonics," *APL Photonics 4, 080802*, 2019.